Fabrication and Characterization of Micro-patterned Porous Membranes Using Hydrogel Facilitated Phase Separation Method

by

Asad Asad

A thesis submitted in partial fulfilment of the requirements of the degree of

Doctor of Philosophy

Department of Mechanical Engineering
University of Alberta

Abstract

Membrane separation processes are now well-established technologies in a wide range of applications, including biotechnology, pulp and paper, pharmaceutical, food processing, petroleum, wastewater treatment, and seawater desalination. The main challenges in membrane separation processes are (i) flux decline due to membrane fouling and (ii) the trade-off relationship between permeability and selectivity of a membrane. Membrane fouling is defined as the attachment of fouling materials (water contaminants) on the membrane surface and inside its pores, resulting in an overall reduction of the membrane performance with time and reducing its life span. Furthermore, membranes with high permeability (how fast the desired molecule to pass through a membrane) typically show a low rejection (how selective a membrane is to a desired molecule compared with the rest). The current methods to increase the membrane performance rely on chemical and physical approaches such as coating the membrane with hydrophilic/hydrophobic layers or modifying the membrane matrix through blending with additives (nanofillers, surfactants, and polymeric additives). However, these approaches have some severe disadvantages and limitations, such as the leaching of additives and coated materials during filtration, which affect the membrane performance, as well as the environmentally unfriendliness of utilized chemicals. Surface patterning has been proven to be an effective method to enhance membrane performance by increasing the effective surface area, which is directly proportional to the permeate flux.

In this work, I presented a novel method to directly apply micro-scale patterns on the membrane surface using hydrogel facilitated phase separation (HFPS). A Hydrogel mold initiates the phase separation spontaneously when it contacts the polymer solution and this ensures that the location of the dense skin layer is on the patterned side. With this method, the active surface area of a membrane is larger than the equivalent flat surface that subsequently enhances water flux without a need to change the membrane surface chemistry. Fouling experiments with Bovine Serum Albumin (BSA) solution showed an increase in the flux for the patterned membrane after 100 min operation, demonstrating the advantage of using microstructure membrane for filtration applications.

In the second phase of this research, I demonstrated, for the first time, a simple treatment process that allows repeated usage of the same hydrogel mold in micropatterned phase separation membrane castings. The method consists of warm and cold treatment steps to provide organic solvent extraction from hydrogel without changing the mold integrity. The best recovery result was 96%, which was obtained by placing the hydrogel in a warm water bath (50 ºC) for 10 minutes followed by immersing in a cold bath (23 ºC) for 4 minutes and finally 4 minutes drying in air.

In the third phase, I prepared novel polyamide-imide (PAI) microfiltration membranes using our recently developed HFPS and Non-solvent induced phase separation (NIPS) techniques. The prepared membranes, including HFPS-patterned, HFPS-unpatterned, and NIPS, showed high porosity, superhydrophilicity, and underwater superoleophobicity. The underwater oil contact angles of n-hexadecane and mineral oils were higher than 150°, while a complete repellency for diesel oil was observed for all membranes. The ultra-high-water flux of patterned HFPS membranes, 440 Liter meter^{-2} hour^{-1} (LMH), made them outstanding candidates for separating oil/water emulsions. For all fabricated membranes, gravity-driven filtration experiments of 9 consecutive oil cyclic filtration tests yielded > 99.9% oil removal efficiency. Moreover, after 18 filtration experiments, the flux recovery ratio and flux decline were in the range of 90-100 % and 3-20 %, respectively.

In the fourth phase, I fabricated novel micropatterned thin-film composite (TFC) NF membranes using a two-step process. First, Hydrogel facilitated phase separation (HFPS) method was used to prepare micropatterned polyethersulfone (PES) substrate. Second, a thin dense polyamide (PA) film was formed on top of the PES substrate using interfacial polymerization reaction between piperazine (PIP) and trimesoyl chloride (TMC) monomers. TFC patterned membrane with 0.25 wt.% PIP showed ~96% increase in the water flux compared with an unpatterned one with only less than 10% reduction in the separation performance for different salts (e.g., $MgSO_4$, Na_2SO_4, and NaCl), reactive black 5 dye, methyl orange dye and the treatment of real oil sands produced water due to the increase in the surface area.

Keywords: Membrane technology, transport through membranes, thin-film composite membranes, nanocomposite membranes, phase separation, phase inversion, nonsolvent induced phase separation, patterned membranes, hydrogel, soft lithography, bioinspired, membrane fabrication, soft lithographically, hydrogel-facilitated phase separation, hydrogel mold, oil/water separation, antifouling property, super-wetting property, micropatterned membranes, microfiltration, ultrafiltration, nanofiltration, reverse osmosis. SAGD produced water, wastewater treatment, dye rejection, salts rejection.

Preface

This doctoral dissertation is an original work by Asad Asad. Chapters 1, 2, 3 4 are published. Chapter 5 has been submitted recently and the current status is under review. The following publication is the result of this research work:

1- Asad, Asad, et al. "Gravity assisted super high flux microfiltration polyamide-imide membranes for oil/water emulsion separation." *Journal of Membrane Science* 621 (2021): 119019.

2- Asad, Asad, et al. "Durability and recoverability of soft lithographically patterned hydrogel molds for the formation of phase separation membranes." *Micromachines* 11.1 (2020): 108.

3- Asad, Asad, Mohtada Sadrzadeh, and Dan Sameoto. "Direct micropatterning of phase separation membranes using hydrogel soft lithography." *Advanced Materials Technologies* 4.7 (2019): 1800384.

4- Asad, Asad, Dan Sameoto, and Mohtada Sadrzadeh. "Overview of membrane technology." *Nanocomposite Membranes for Water and Gas Separation*. Elsevier, 2020. 1-28.

5- Asad Asad, Dan Sameoto, Mohtada Sadrzadeh, Patterned Microfilter Membrane and Method of Preparing the Same, US Patent Application Serial No. 62/530,445, Date of Filing: July 10, 2017.

6- Micro-patterned Thin Film Composite Poly(piperazine-amide) Nanofiltration membranes for Wastewater Treatment. Status under review.

Dedicated to my lovely parents,

Ahmad & Shukrieh

And the love of my life, my wife,
Rawan Jaradat

For their endless love and support through all times.

I will always love you

Acknowledgement

I would like to express my deepest respect to my supervisors Mohtada Sadrzadeh and Dan Sameoto, for their continuous support and help through this journey. I cannot express my gratitude to both of you. You trusted me to join your groups and have always been there for me through tough times. From the deepest spot in my heart, thank you for everything!

I would like to thank my supervisor committee member Dr. Ayranci for being supportive through this journey as well.

Special thanks to my best friend Waleed Al-Mahshi for his endless support and help. You were always there for me, and I will always be there for you!

Special thanks to my colleagues: Hadi Nazaripoor, Mohammad Abu Hassan Khondoker, Samuel Lehman, Debanik Bhattacharjee, Behnam Khorshidi, Aida Razi, Amin Karkooti, Mohammad Abu Hassan Khondoker, Nadia Baheri, Adam Ostashek, Tianshuo Liang, Teng Zhang, Luka Morita, Laleh Shamaei, Masoud Rastgar, Pooria Karami, Farhad Ismail, Ali Mohammadtabar, Simin Shabani, Ishita Biswas, Hassan Hosseini, Nusrat Hellali, Sadegh Aghapour, Zayed Mansouri, Adham Riad, Amirriza and Parmiss Mojir Shaibani for all the nice memories we have had together.

Table of contents

List of Tables

List of Figures

Chapter 1

Introduction

1.1 Water demand

Water and energy shortages are two of the greatest challenges humanity will face for the foreseeable future [1]. Worldwide, more than 1.2 billion people lack access to the fundamental human need for clean drinking water, leaving them susceptible to waterborne diseases transmitted through wastewater sources or sewage, causing the deaths of millions each year [2,3]. The increased demand for water resources is due to several reasons such as climate change, population growth, industrial activities, and agriculture purposes; this increases the need for water resources to meet the higher demand [4]. Although seawater desalination has been a popular method for increasing the availability of water resources, the high costs of desalination limit its use in many countries [5]. Moreover, studies have proven that municipal wastewater treatment is more environmentally sustainable and more economical than desalination of seawater. In fact, municipal wastewater can be treated and converted into a higher standard of quality than the current drinking water regulation with a cost reduction of 40% compared to seawater desalination [6].

1.2 Membrane separation processes

Membrane separation processes are now well-established technologies in a wide range of applications, including biotechnology [7], pulp and paper [8], pharmaceutical [9], food processing [10,11], petroleum [12,13], and seawater desalination [14]. A membrane is a selective thin layer of a semi-permeable material. By applying a potential gradient, such as pressure, temperature, electrical, or concentration difference, as a driving force, the membrane separates undesired materials from a feed solution based on their sizes or affinity. In general, membranes are classified based on their material, their morphology, and their average pore size. Membrane materials can be organic and inorganic. Organic membranes, such as polysulfone (PSf), polyethersulfone (PES), polyvinylidene fluoride (PVDF), polyacrylonitrile (PAN), polytetrafluoroethylene (PTFE), polyamide-imide (PAI) are the most common polymeric membranes for lab and industrial applications. On the other hand, the most common inorganic membranes are metallic, ceramic, and zeolite membranes. Although inorganic membranes, such as metals or ceramics, exhibit superior mechanical, chemical, and thermal properties compared to the polymeric ones, they are more expensive to fabricate and so not preferred [15]. In terms of cross-section morphology, membranes are divided into anisotropic (asymmetric) and isotropic (symmetric) membranes, as shown in Figure 1.1. Anisotropic membranes include composite membranes, integrated asymmetric membranes and supported liquid membranes, while isotropic membranes consist of microporous membranes, nonporous dense membranes, and electrically-charged membranes [16]. Regarding pore size, membranes can be categorized into dense and porous membranes. As can be observed in Table 1.1, porous membranes are used in microfiltration (MF), ultrafiltration (UF), and membrane distillation (MD) processes. In all other types of membrane processes, dense membranes are utilized.

Table 1.1 shows the most common types of membrane separation processes. Among these processes, MF, UF, Nanofiltration (NF), and Reverse osmosis (RO) are the most widely used membranes for water treatment and are the focus of this study. MF is employed to separate solutes with a diameter higher than 100 nm [17]. The MF membranes can separate sand, clays, algae, and some bacteria. UF membranes are denser than MF membranes and can remove solutes with a diameter in the range of 10 nm to 100 nm. UF membranes can separate all species removed by MF and some viruses and humic organic materials. NF membranes are denser than UF membranes and have a higher hydrodynamic resistance, which requires a stronger driving force (pressure) for filtration. NF membranes can separate solutes in the range of 1 nm to 10 nm. RO membranes are considered nonporous membranes, separating even very small, monovalent ions, such as Na^+.

Membrane performance is generally measured by two parameters: flux and selectivity. The flux of a membrane can be expressed as the volume of a substance that permeates through a membrane per unit area over a period of time. The most common units used in the literature to describe the flux for water treatment applications is L m^{-2} hr^{-1} (LMH) and gal ft^{-2} day^{-1} (GFD). The selectivity of a membrane can be expressed by the retention or rejection (R) of solutes when treating aqueous mixtures consisting of solvent (mostly water) and solutes. There are two types of filtration modes: the cross-flow and the dead-end filtration systems (Figure 1.2). These types mainly depend on the direction of the feed streams with respect to the membrane surface and the permeate direction. In the cross-flow filtration, the direction of the feed stream is tangential to the membrane surface and perpendicular to the permeate. The shear forces resulting from the interaction between the feed stream and the membrane surface helps to remove some of the materials deposited on the membrane surface [18]. The dead-end mode is more prone to fouling as the feed stream and the permeate are both perpendicular to the membrane surface and the accumulation of the rejected particles increases on the membrane surface with time [19].

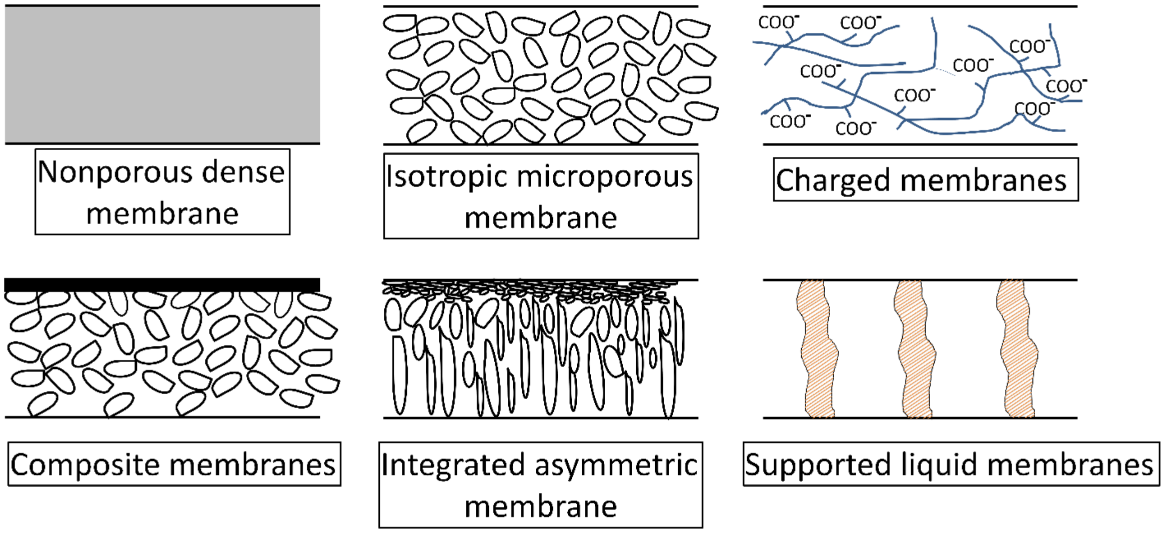

Figure 1.1. Schematic diagram of membranes with different morphologies.

Table 1.1. Characteristics of various membrane processes

Membrane Process	**F/P phase**	**Driving force**	**Membrane morphology**	**Separation principle**	**Application**
Microfiltration (MF)	L/L	ΔP	Porous 10^{-1}–10 μm	Sieving mechanism	Separation of macromolecular to cellular size particles (Bacteria/fat and some proteins)
Ultrafiltration (UF)	L/L	ΔP	Porous 10^{-2}–10^{-1} μm	Sieving mechanism	Separation of molecular to macromolecular size particles (All proteins)
Nanofiltration (NF)	L/L	ΔP	Dense/Porous 10^{-3}–10^{-2} μm	Solution-diffusion	Separation of Ionic to molecular size particles (Lactose)
Reverse Osmosis (RO)	L/L	ΔP	Dense 10^{-4}–10^{-3} μm	Solution-diffusion	Separation of ions (all minerals)
Gas Separation (GS)	G/G	ΔP	Dense & porous	Solution-diffusion & sieving mechanism	Separation of gases
Pervaporation (PV)	L/G	ΔP	Dense	Solution-diffusion	Separation of liquid mixtures
Electrodialysis (ED)	L/L	ΔE	Dense ion-exchange membranes	Donnan exclusion	Separation of ions mostly in desalination of water
Forward Osmosis (FO) & Dialysis	L/L	ΔC	Dense	Solution-diffusion	Separation of neutral, low molecular weight particles based on diffusion
Membrane Distillation (MD)	L/L	ΔT, ΔP	Porous 0.2-1.0 μm	Vapor-liquid equilibrium	Removal of volatile components, the concentration of solutions

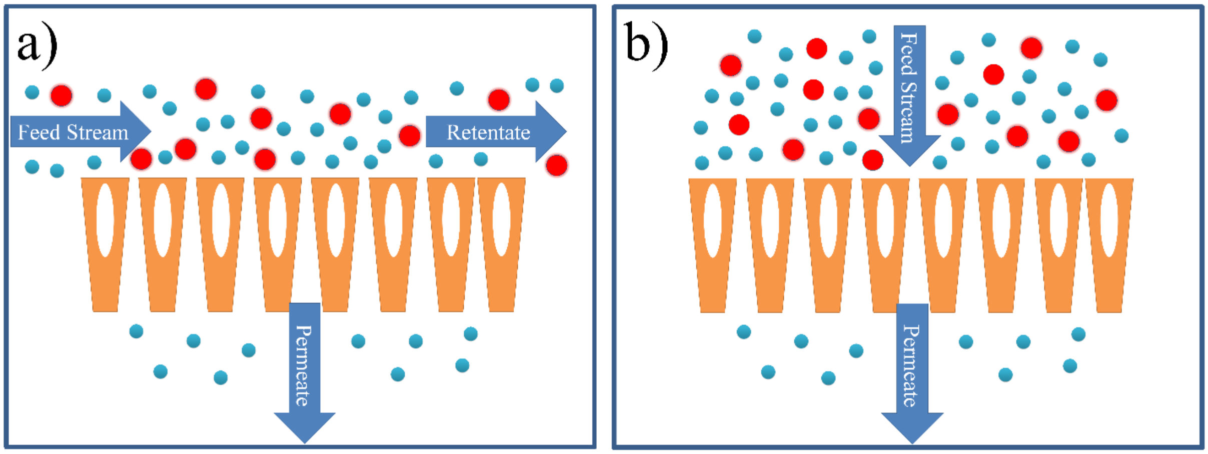

Figure 1.2 Schematic diagram of types of filtration modes

1.3 Water transport through polymeric membranes

Based on their morphology, membranes for water separation can be categorized into porous and dense. In the following sections, more details about the models related to water transport through porous and dense membranes are presented.

1.3.1 Porous membranes

The separation of porous membranes is based on the sieving mechanism in which molecules larger than the membrane pores are rejected while smaller ones pass through. The pure water flux through a porous membrane can be described using Darcy's law:

$$J = A\left(p_f - p_p\right) = A\Delta p, \qquad (1.1)$$

where J is the volumetric flux, A is the hydraulic permeability constant, p_f is the pressure at the feed side, p_p is the pressure at the permeate side and Δp is the transmembrane pressure across the membrane. The hydraulic permeability constant, A, depends mainly on membrane morphology, including porosity, tortuosity, average pore size distribution and feed characteristics, such as viscosity. Two approaches are commonly used to determine this constant, depending on the membrane's internal structure. The Hagen-Poiseuille approach [19] assumes that the internal structures are a set of parallel cylindrical pores across the membrane with a length equal to the membrane thickness. Flux is then written as follows:

$$J = \frac{\varepsilon\, r^2}{8\varphi\tau}\,\frac{\Delta P}{\delta}, \tag{1.2}$$

where ε is the membrane porosity, r is the average pore size, φ is the feed viscosity, τ is the tortuosity and δ is the membrane thickness. The second approach, Kozeny-Carman[19], assumes the membrane structure as closed packed spheres:

$$J = \frac{\varepsilon^3}{K\varphi\, S^2(1-\varepsilon)^2}\,\frac{\Delta P}{\delta}, \tag{1.3}$$

where ε is the membrane porosity, K is the Kozeny-Carman constant, which is a function of the tortuosity and the shape of pores, φ is the feed viscosity and S is the internal surface area.

1.3.2 Dense membranes

Molecules with sizes in the same order of magnitude of oxygen, nitrogen and metal ions cannot be separated by porous membranes. Therefore, dense or nonporous membranes are used, such as NF and RO membranes. Although NF/RO membranes are considered nonporous, they do have pores at the molecular level, which allow transport of small molecules via diffusion. In NF/RO membranes, transport is affected by a combination of concentration polarization (CP) and fouling by organic matter, colloidal particles, and microorganisms. These parameters are interconnected and reduce the water permeate flux through membranes over time. Hoek and Elimelech were the first to propose a model to explain the effects of both colloidal fouling and concentration polarization on flux decline, which is called cake enhanced concentration polarization (CECP)[20].

Based on their model, the total membrane resistance in NF/RO membranes consists of three major components: the hydrodynamic resistance of the membrane (the resistance of the membrane itself); the resistance of the accumulated colloids fouling at the membrane surface (cake-layer fouling); and lastly the accumulation of ions on the membrane surface (concentration polarization). Equation 4 shows the water flux permeation using the cake enhance concentration polarization model:

$$J = \frac{\Delta p - \Delta\pi}{\mu(R_m + R_c)}, \tag{1.4}$$

where J is the water flux permeated through the membrane, μ is the dynamic viscosity of water, $\Delta\pi$, R_m and R_c are the cake-enhanced osmotic pressure difference, hydrodynamic membrane resistance, and the cake layer resistance, and concentration polarization resistances, respectively.

Hydrodynamic membrane resistance The hydrodynamic membrane resistance (R_m) is the resistance of the membrane in the absence of any fouling materials. For pure water filtration, both $\Delta\pi$ and R_c will be removed from Equation 4, and R_m is determined as follows:

$$R_m = \frac{\Delta p}{J\mu} \tag{1.5}$$

Cake layer resistance: The cake layer resistance ($R_c, 1/m$) can be measured by the Kuwabara cell model [21]:

$$R_c = \frac{9A_K M_c}{2a^2 g^* \rho_p A_m} = \frac{9A_K \delta_c (1 - \epsilon_c)}{2a^2 g^*}, \tag{1.6}$$

where A_K is the Kuwabara correction factor, which depends on neighbored particles in the cake layer. M_c (kg) is the mass of the deposited colloidal particles on the membrane surface measured by a simple mass balance, a is the particle diameter, g^* is the electroosmotic effect of a swarm of charged colloidal particles, ρ_p is the density of the colloidal particles, A_m is the membrane surface area, δ_c is the thickness of the cake layer and ϵ_c is the porosity of the cake layer. Another way to measure the cake layer resistance (R_c) is to determine permeate flux at a specific pressure, in the absence of ions ($\Delta\pi$=0), and substituting in the rearranged form of Equation 4 as follows:

$$R_c = \frac{\Delta p}{J\mu} - R_m \tag{1.7}$$

Concentration polarization (CP) In the absence of fouling, the accumulation of ions on the membrane surface generates a transmembrane osmotic pressure (TOMP), which reduces the effective transmembrane pressure (TMP). The effect of TOMP is represented as the concentration polarization resistance ($\Delta\pi$), which can be calculated from equation 1.8 by measuring the permeate flow rate across a membrane at a known TMP using saltwater ($R_c = 0$):

$$\Delta\pi = \Delta p - J\mu R_m \tag{1.8}$$

It must be noted that the cake layer intensifies the effect of concentration polarization and in the CECP model $\Delta\pi$ must be replaced with cake-enhanced osmotic pressure difference ($\Delta\pi^*$). The derivation is provided elsewhere [22].

1.4 Membrane fabrication methods

1.4.1 Fabrication of porous membranes

Porous membranes are fabricated by electrospinning, stretching, track-etching, and phase inversion method. Phase inversion is the most versatile method to prepare membranes in which different kinds of morphologies can be obtained for different applications[23]. All phase inversion membranes are based on the precipitation of a polymer from an originally homogenous casting solution. The precipitation occurs through a demixing process where a polymer solution (made of polymer and solvent) is transformed from a liquid into a porous solid-state due to an exchange between the solvent and a nonsolvent. The precipitation of polymer solution is governed by the thermodynamics and the kinetics of the phase inversion process, which subsequently affect the final morphology of prepared membranes. Thermodynamic and kinetic properties can be primarily controlled by changing the formulation of the casting solution, i.e., the type and concentration of polymer, solvent, and additives [24]. Most available commercial membranes are prepared using the phase inversion method by one of the following techniques: (1) lowering the temperature of the casting solution below a critical threshold (thermally-induced phase separation, TIPS), (2) evaporation of the volatile solvent from the cast polymer film (evaporation-induced phase separation, EIPS), (3) immersion of the polymer film in a non-solvent vapor phase (vapor-induced phase separation, VIPS), and (4) immersion of cast polymer film into the nonsolvent bath (nonsolvent-induced phase separation, NIPS). NIPS is the most broadly used method for fabricating porous membranes due to some advantages, such as low cost and easy implementation.

The procedure of membrane preparation by the NIPS method is shown in Figure 1.4. In this method, the precipitation of the polymer occurs due to the exchange of solvent from the polymer solution and the nonsolvent. After immersing the polymer film in the nonsolvent bath, phase separation happens initially at the film interface. First, it starts with an abrupt change in the polymer chemical potential, causing a net movement of the polymer towards the film interface. This increases the polymer concentration at the interface until it becomes rigid and forms a skin layer, which prevents further transport of the nonsolvent into the cast film. The formation of the finger-type structure occurs in two stages: the initiation and the propagation. The initiation happens at points where the skin layer ruptures as a result of shrinkage stresses and syneresis. After that, the growth of fingers happens at the ruptured points and propagates towards the bottom of the polymer cast film [25,26]. Due to the continuous demixing process, the polymer solution is separated into a polymer-rich phase that creates the membrane structure and a polymer-lean phase that forms the membrane pores. The internal structure is hierarchal, with a dense skin layer at the solvent/nonsolvent interface.

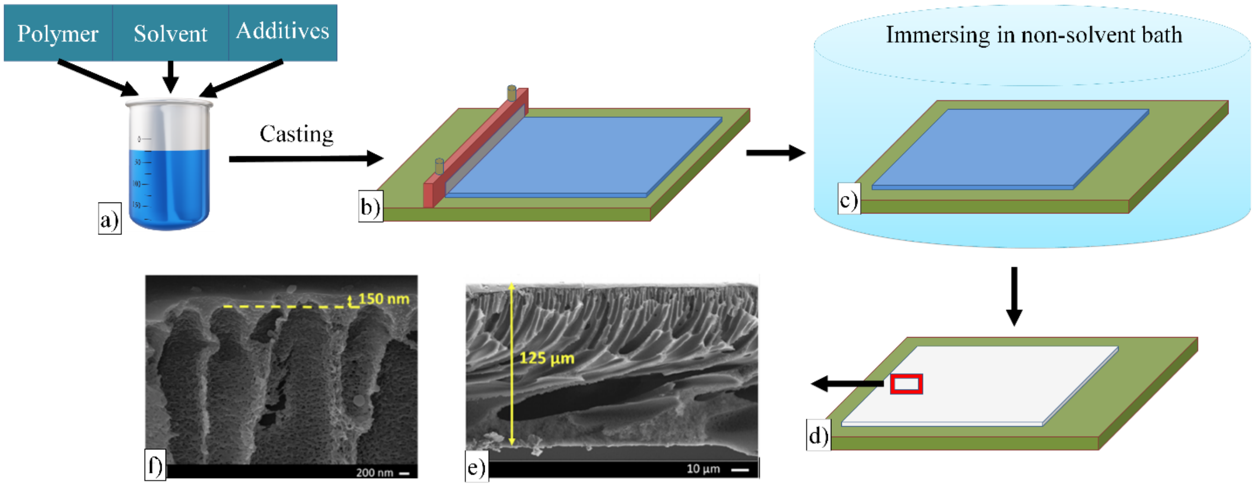

Figure 1. 3. (a-d) Schematic diagram of the preparation process for NIPS membranes and (e-f) [27] SEM images of the internal structures and the skin layer of PES membranes

1.4.2 Fabrication of dense membranes

Interfacial polymerization (IP) is one of the most popular methods to prepare dense membranes. In this method, a thin, selective layer, typically made of polyamide (PA), is formed on microporous support by in-situ polymerization reaction (Figure 1.12). Although Morgan was the first to propose the use of IP to create a very thin PA layer on a porous substrate, his approach was not successfully deployed at industrial scales. In the early 1970's Cadotte et al. successfully applied this technique to form a series of thin-film composite (TFC) membranes with high performance [28,29]. In this method, two fast-reacting monomers (diamine and acyl chloride) are dispersed in two immiscible solutions; one of them is preferably water. First, a porous membrane is impregnated with an aqueous solution (e.g., water) containing the diamine monomers. After that, the impregnated membrane is brought into contact with an organic solution containing acid chloride. Since both solutions are immiscible, the reaction takes place at the interface in sequential stages [30]. At first, a highly crosslinked layer forms at the interface, called the incipient layer, due to the extremely fast reaction between the monomers. This layer slows down the diffusion of the diamine monomers to the organic solution, shifting the IP reaction into a slow-growth mode and resulting in a loose polymerized layer in the shape of ridges-and-valleys. Finally, the reaction stops once the PA layer prevents further diffusion of the diamine monomers into the organic layer [31].

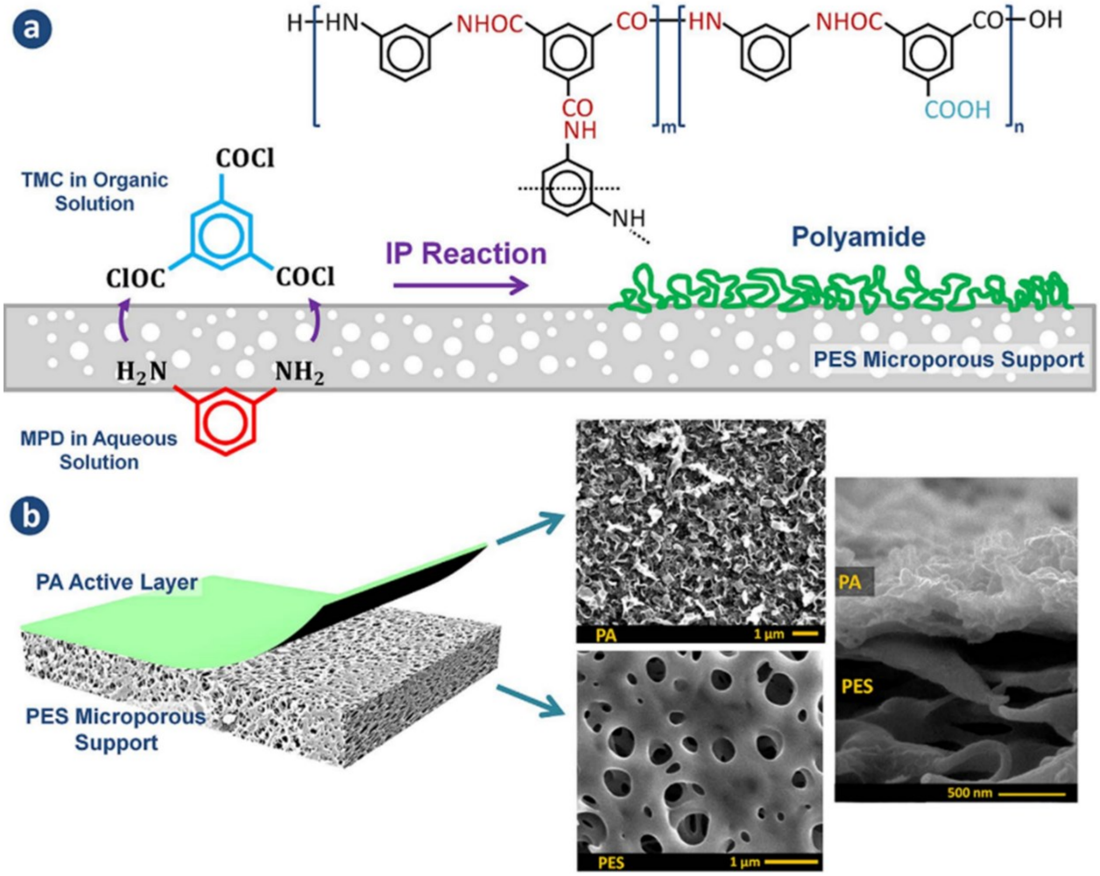

Figure 1. 4. (a) A schematic diagram shows the formation mechanism of the polyamide layer on a PES support membrane using the interfacial polymerization (IP) reaction between MPD and

TMC monomers. (b) SEM images of the top surface of the TFC membrane, the porous layer beneath it, and the cross-sectional image of the TFC membrane [32].

1.5 Membrane modification methods

1.5.1 Surface coating and chemical grafting

Several surface modification methods have been investigated to improve permeation properties and to reduce the fouling of membranes [17,33]. Most of these methods are based on physical coating or chemical grafting of multifunctional materials on the surface of membranes to change their surface properties such as hydrophilicity, surface charge, and roughness [34-36]. While versatile, inexpensive, and applicable to many substrates, the physical coating method suffers from some major drawbacks, including the weak attachment of the coating layer to the membrane surface and the leaching of materials during modification and cross-flow filtration. The need to make more stable coatings has attracted attention to chemical grafting methods. In the chemical grafting method, (super)hydrophilic macromolecules are either grafted to or grafted from the membrane surface. In the ‘graft to’ method, the hydrophilic polymer chains are tethered to the membrane surface, while in the ‘graft from’ method, the polymer chains are grown from the surface. Nevertheless, in both methods, the need for post-treatment steps, such as plasma or UV treatment, to ensure grafting, as well as the potential hazard of grafted materials leaching to the environment, raises concerns regarding the scalability, cost, and environmental impacts of these methods [17,37,38].

1.5.2 Nanocomposite membranes

Although polymeric membranes are widely used for membrane separation processes, they suffer from three main challenges: (i) the trade-off relation between permeability and selectivity; (ii) low thermal stability; and (iii) membrane fouling. All these challenges are associated with the material properties, not the method of membrane fabrication. Therefore, a new class of membranes was developed in the 1970s by combining nanomaterials within cellulose acetate (CA) membranes to improve the compaction resistance [39]. Later, this unique combination garnered significant attention as an alternative method to tune and enhance membrane performance [40]. For example, the most common polymers used in membrane applications, such as polyethersulfone (PES), polyvinylidene fluoride (PVDF), polypropylene (PP), polytetrafluoroethylene (PTFE), are hydrophobic. Therefore, incorporating hydrophilic nanomaterials into these membranes changes their property from hydrophobic to hydrophilic [41,42]. Nanocomposite membranes are classified into four categories based on the location of the nanomaterials and the type of membrane: (1) conventional nanocomposite; (2) surface located nanocomposite; (3) thin-film nanocomposite (TFN); and (4) thin-film composite (TFC) with nanocomposite substrate. A schematic diagram of the four types of nanocomposite membranes is shown in Figure 1.14. Each one of these membranes has unique advantages over the others. Despite the significant improvements enabled by nanomaterials, there are still some major challenges in synthesizing nanocomposite membranes. These challenges are (i) poor dispersion of nanomaterials in the polymer solution (polymer and solvent), (ii) aggregation of nanomaterials within the membrane matrix which results in defects, (iii) low compatibility between nanomaterials and the membrane, and (iv) weak chemical interaction between nanomaterials and the membrane material, which may result in leakage of nanomaterials [43,44].

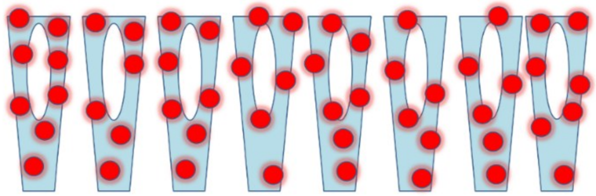

Conventional Nanocomposite

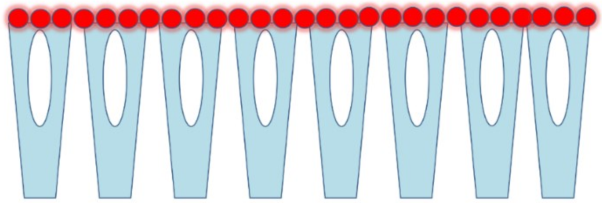

Surface Located Nanocomposite

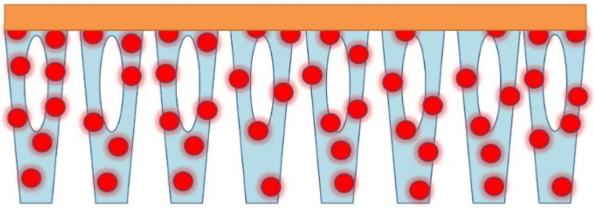

TFC with Nanocomposite Substrate

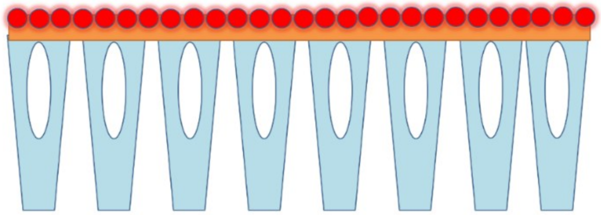

Thin-film Nanocomposite

Figure 1. 5. Schematic of typical types of nanocomposite membranes

1.5.3 surface patterning

Recently, increased attention has been directed towards surface topography as a promising approach to increase membrane performance. The idea involves applying patterns on the membrane surface that increase its surface area, increasing the water permeation and introducing secondary flow in the water, which reduces the deposition of unwanted materials on the membrane surface.[45] There are currently two methods to prepare patterned membranes: *phase separation micromolding (PSμM)* and nanoimprint lithography (NIL); however, these methods have some serious challenges.

1.5.3.1 Phase inversion micro-molding

In 2003, Vogelaar *et al.* presented *PSμM* for the first time to make patterned porous membranes [46]. In the phase inversion technique, a homogeneous polymer solution is cast as a thin film on a flat substrate and then immersed in a coagulation bath containing a non-solvent (e.g., water). The solvent exchange with the non-solvent results in a porous membrane with a dense skin layer at the polymer film/non-solvent interface[25,47]. Vogelaar *et al.* used the same principle; however, instead of casting the polymer solution on a flat surface, it was cast on a patterned impermeable substrate and then immersed in a water bath (see Figure 1.6). Although this method succeeded in preparing patterned membranes, the location of the dense layer was at the unpatterned side, making the addition of patterns useless. Therefore, no water filtration using these membranes was performed at that time. In 2012, Won *et al.* proposed a modified immersion precipitation method to relieve the formation of the dense layer on the unpatterned side of the membrane. After casting the polymer solution on a PDMS patterned mold, a polyester fabric support was placed on the unpatterned side and then placed in a coagulation bath. The role of the fabric support in this process was to reduce the sudden exchange between the solvent and non-solvent, which directly impacted the formation of the skin layer. Patterns such as pyramid and prism were formed on the surface of polyvinylidene fluoride (PVDF) membranes and tested using a cross-flow filtration system. Their results showed 20% increase in the water flux for patterned membranes compared with the unpatterned ones due to the addition of surface area. Fouling test were also performed using a wastewater taken from a membrane bioreactor process. Confocal laser microscopy (CLSM) showed complete coverage of the unpatterned membranes by microbial cells while patterned membranes showed less deposition on their surfaces indicating that patterned membranes mitigated fouling. It is worth mentioning that no separation results were presented. The main drawback of this process was the average pore size, ~0.89-0.91, which is considered a loose MF membrane that can fail to separate most contaminants. Moreover, controlling the average pore size of these membranes is a big challenge [48,49].

In another study, *PSμM* was used to prepare symmetric porous patterned membranes but instead of using water as the coagulation bath, water vapor was chosen. The precipitation of the polymer occurs due to the penetration of the vapor into the film which eventually forms a symmetric porous membrane without a dense skin layer [50,51]. The pores of these membranes ranged from 0.2 – 1 μm which made them less efficient for separation of particulates [52].

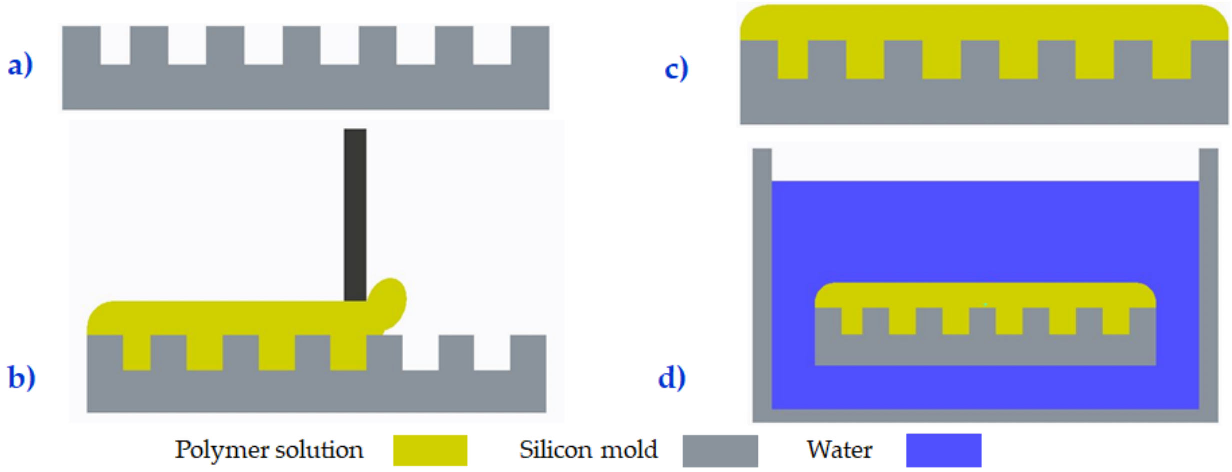

Figure 1. 6. Schematic illustration of preparing patterned membranes using phase separation micromolding technique.

1.5.3.2 Nano-imprint lithography

In 2013, Marouf *et al.* used nanoimprint lithography (NIL) to surface pattern commercial UF membranes (Figure 1.20). In this process, a patterned silicon mold with 200 nm depth of parallel ridges was heated up to 120 °C and imposed on the top of a commercial UF membrane. The applied pressure to form the patterns was 40 bar which is more than 10 times higher than the operating pressure; therefore, the internal structures of these membranes were damaged. As a result, when the prepared membranes were tested in a cross-flow system, the flat membranes showed higher pure water permeance compared with the patterned one [53]. Therefore, the molecular weight cut-off of the patterned membranes dropped by 40% compared with the unpatterned ones. This indicates that the excessive applied pressure to induce the patterns not only damaged the internal structures but also damaged the surface pores.[54] However, during fouling tests with colloidal silica particles flux results increased by 19-45% for patterned membranes due to the anti-fouling property induced by the patterns.[53] In addition, the direction of the feed flow/pattern orientation was very critical to mitigate the deposition of silica particles. Results showed lower silica particles deposition were achieved when the orientation of the flow was perpendicular to the orientation of the ridge and valley patterns compared with other orientations. Since the NIL method were applied on pre-existing PSf commercial membranes, applying this method on other types of polymeric membranes and lab produced membranes requires adjusting the pressure and temperature with every single new recipe. This increases the variation in the produced porous substrate and may completely damage some membranes due to the excessive applied pressure.

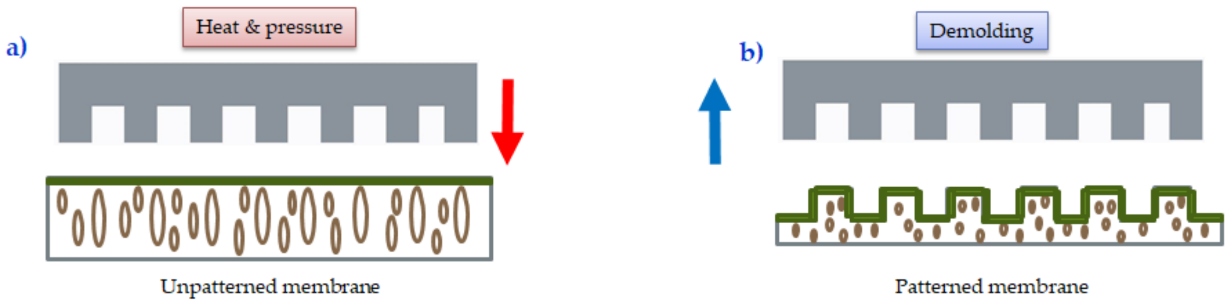

Figure 1. 7. Schematic illustration for preparing patterned membranes using nanoimprint lithography (NIL) technique.

1.6 Research objectives

This work aims to develop a new method to fabricate energy-efficient patterned membranes with an improved filtration performance that can overcome the limitations of *PSμM* and NIL methods. To achieve this objective, the current work is conducted through the following themes:

I. *Developing a new sustainable method to make phase separation patterned membranes with a skin dense layer at the patterned side using hydrogel.* Hydrogel acts as a water reservoir that can be feasibly patterned with different shapes and geometries while conserving its shape for months. With these advantages, if hydrogel is used to make membranes, the formation of the membranes starts from the mold, ensuring the existence of the selective skin layer on the patterned side. The sustainability of our method was examined through the reusability of the hydrogel in making phase separation membranes. The reusability of hydrogel molds relies on maintaining the same initial water content after each membrane formation. The main challenge in this phase is extracting the organic solvent from the hydrogel mold without damaging its internal structure. The importance of this step is for future implementation of hydrogel into a continuous scale producing through a roll-to-roll manufacturing system.

II. *The Application of Patterned Membranes for Wastewater Treatment*: The prepared membranes will be evaluated to treat different industrial wastewater, including oil sand, textile, and oily wastewater. Different types of patterned membranes should be fabricated for various wastewater streams. Oily wastewater can be treated with MF and UF membranes which can be prepared directly using the HFPS method. Concerning textile wastewater and oil sands produced water, they need NF membranes to remove dissolved organic matter. NF membranes are usually prepared by coating patterned membranes with an ultrathin polyamide layer using IP reaction. The primary challenge is to ensure good adhesion between the polyamide layer and the patterned substrate.

1.7 Thesis structure

This is a paper-based doctoral dissertation that contains six chapters. Chapters 1, 2, 3, and 4 are published, while chapter 5 has been submitted for publication.

Chapter 1 presents a brief overview of polymeric membranes and their classifications, as well as the most common types of membrane separation processes. It also includes the common methods to fabricate porous and dense membranes. In addition, it provides a brief summary of the current methods to fabricate patterned membranes and their limitations.

Chapter 2 presents detailed steps of the fabrication process of patterned membranes using the hydrogel facilitated phase separation (HFPS) method. In this phase, the HFPS method was developed, and patterned membranes were characterized using scanning electron microscopy (SEM), water contact angle anaylyzer, attenuated total reflectance-Fourier transform infrared (ATR_FTIR), and filtration performance.

Chapter 3 presents a recoverability method of the hydrogel mold after preparing membranes. In this phase, two types of hydrogel treatment were proposed to extract the diffused organic solvent from the hydrogel mold without sacrificing the hydrogel integrity.

Chapter 4 presents super high flux gravity-assisted MF membranes for oily wastewater treatment. In this phase, the HFPS method is used to prepare MF membranes with high porosity, superhydrophilicity, and underwater superoleophobicity, making them outstanding candidates for separating oil/water emulsions under gravity. The morphological properties, hydrophilicity and surface chemistry of the prepared membranes were examined in detail. Moreover, filtration performance of the prepared membranes was performed for the separation of n-hexadecane, diesel, and mineral oil in water emulsions.

Chapter 5 presents novel micropatterned thin-film composite (TFC) NF membranes using a two-step process. First, Hydrogel facilitated phase separation (HFPS) method was used to prepare micropatterned polyethersulfone (PES) substrate. Second, a thin dense polyamide (PA) film was formed on top of the PES substrate using interfacial polymerization reaction between piperazine (PIP) and trimesoyl chloride (TMC) monomers. The prepared TFC membranes were analyzed by their surface roughness, wettability, and surface chemistry. In addition, the filtration performance of these membranes was evaluated through the separation of different salts (e.g., $MgSO_4$, Na_2SO_4, and NaCl), Reactive Black 5 dye, Methyl Orange dye and the treatment of real oil sands produced water.

Chapter 6 summarizes the major findings of all chapters of this thesis and suggests future directions for this research work.

Chapter 2

Direct Micropatterned of Phase Separation Membranes using Hydrogel Soft Lithography method

2.1 Introduction

Membrane separation processes offer a sustainable and reliable method for water and wastewater treatment due to their distinct advantages such as low energy consumption, ease of preparation, upscaling process, and the wide variety of polymers that can be used to manufacture membranes at a relatively low cost [17,55]. A considerable amount of literature has been conducted to improve membranes by physical and chemical methods such as modifying the membrane matrix through blending surfactant and nanofillers within the membrane [13,56,57], or modifying the membrane surface via chemical grafting of polar functional group to the membrane surface [58-61]. Despite the importance of surface modification in improving the membrane performance, there are some serious disadvantages as the grafted/coated functional group deteriorates with time and the chemicals used in the grafting process can be environmentally unfriendly [33]. Recently, increased attention has been directed towards surface topography as a promising approach to increase membrane performance. The idea involves applying patterns on the membrane surface that increase its surface area, which increases the water permeate and also introduces secondary flow in the water, which reduces the deposition of unwanted materials on the membrane surface [45]. Vogelaar *et al.* reported for the first time the use of a micromolding process to prepare patterned polymeric membranes, so-called "*phase separation micromolding (PSμM)*" [46]. In the conventional phase inversion technique, a homogeneous polymer solution is cast as a thin film on a flat substrate and then immersed in a coagulation bath containing a non-solvent (e.g., water). The solvent exchange with the non-solvent results in a porous membrane [25,47]. PSμM can prepare membranes by using either vapor-induced [62-64], or liquid-induced phase separation [65-67] which result in a symmetric and asymmetric structure with a skin layer at the solvent/non-solvent interface, respectively. The main disadvantage of PSμM is that the location of the dense skin layer, in liquid-induced phase separation, is on the unpatterned side of the membrane since the patterned side is always in contact with the mold itself. However, Won *et al.* proposed a modified immersion precipitation method to relieve the formation of the dense layer on the unpatterned side of the membrane, but the mean pore size of the prepared membranes was ~0.89-0.91µm which is not useful to produce ultrafiltration (UF) or nanofiltration (NF) membranes [48]. Marouf *et al.* used nanoimprint lithography (NIL) to surface pattern commercial UF membranes, but results showed that this method affected the pore size and number of pores. Therefore, when the prepared membranes were tested in a cross-flow system, the flat membranes showed higher pure water permeance compared with the patterned ones [53].

We have developed a new method to produce patterned membranes with a thin dense layer on the patterned side by making the structured mold itself out of the non-solvent. Hydrogel is a water-swollen polymeric material that is capable of holding and retaining large amounts of water molecules between its polymer chains [68]. The hydrogel acts as a reservoir of water which can be structured in an inexpensive way, allowing for water-based molds that can be produced in different geometries. Hydrogels have attracted substantial attention in the research community in different fields such as tissue engineering [69], cell culture [70], pharmaceutical [71], and biomedical applications [72]. However, the hydrogel has never been applied to the area of phase separation manufacturing of membranes before this work. Our technique is different from phase separation micromolding – where the mold is impermeable [46], our method has a permeable mold which allows solvent/non-solvent demixing to happen between the polymer solution and the mold itself. The water in the hydrogel acts as the non-solvent, and since the place of the solution/non-solvent interface defines the location of the dense layer; this method is able to produce a thin dense layer on the patterned side of the membrane. This work shows the first proof-of-principal designs of phase inversion membranes produced in conventional non-solvent induced phase separation (NIPS) and hydrogel-facilitated phase separation (HFPS).

2.2 Experimental Section:

2.2.1 Materials

Polyethersulfone (PES, BASF Ultrason E6020p, M_w=58 kDa), N, N-Dimethylacetamide (DMAc, Sigma-Aldrich), and polyvinylpyrrolidone (PVP, Sigma-Aldrich, M_w = 35 kDa) were used to prepare polymer casting solution. Agarose (Sigma-Aldrich, CAS number: 9012-36-6) and PVP were utilized to make hydrogel solution. Polymethylmethacrylate (PMMA, McMaster-Carr) was utilized to develop master molds. BSA (ChemCruz, Product code: SC-2323) was used to prepare the fouling solution.

2.2.2 Preparation of solutions

The membrane polymer solution was prepared by dissolving 15wt% PES and 2wt% PVP in 83wt% DMAc. The solution was placed on a magnetic stirrer overnight to produce a homogeneous polymer solution. The hydrogel solution was prepared with 5wt% agarose and 1wt% PVP mixed with 94 wt% distilled water. The mixture was then placed in a microwave and heated up until boiling. Finally, the mixture was gently degassed to remove air bubbles. The PEG solution was prepared by dissolving 0.25 g of PEG powder in 1 L of distilled water and then stirred for 10 minutes. In each experiment, a fresh PEG solution was used. The BSA solution was prepared by dissolving 0.05 g of BSA powder in 1 L of distilled water and then stirred until it is completely dissolved. In each experiment, a fresh BSA solution was used.

2.2.3 Preparation of the master molds:

The PMMA trenches molds were manufactured using a CO_2 laser cutter (VLS 3.5 Versa Laser). The posts and the crosses master mold were prepared using lithography techniques.

2.2.4 Preparation of the HFPS membranes

Figure 2.1. illustrates the preparation steps for patterned membranes using hydrogel molds. First, polymethylmethacrylate (PMMA) substrate was used to prepare ridge-pattern master mold using CO_2 laser cutter (Figure 2.1a and 2.1b). The master mold can also be prepared using lithography techniques or 3D printing technology depending on the desired features and dimensions. Next, a hydrogel solution is prepared and cast with a thickness of 1.6 mm on top of the patterned mold that comprises the desired structures and left to gel at room temperature (Figure 2.1c) before demolding. The hydrogel mold is then placed on a smooth substrate, and pressurized air is used to remove standing water from the patterned side (Figure 2.1d). Without this step, some water drops will remain between the patterns, which will affect the quality of the replicated structures, resulting in a non-uniform membrane. The polymer solution is cast on the patterned side of the hydrogel mold using a film applicator (Figure 2.1e). After that, the solvent exchanges with the non-solvent at the film surface, and due to the huge sudden gradient of the polymer chemical potential, this causes a net movement of the polymer towards the solvent/non-solvent interface. After the polymer concentration in the top layer of the cast film reaches a specific point, a skin layer forms on the surface and acts as a barrier for further non-solvent transport into the sub-layer of the polymer solution. The polymer solution beneath the skin layer has a lower polymer concentration, forming the finger-type structures in a two-step process; the initiation and the propagation of fingers. The initiation of fingers forms at points where the skin layer fractures as a result of shrinkage stress and syneresis. Subsequently, the growth of the fingers occurs and

propagates towards the bottom side of the membrane [25]. The entire assembly is kept in air for one minute, which is enough to form the membrane. Finally, the membrane is demolded from the hydrogel and is stored in distilled water for later use (Figure 2.1f). Figure 1g shows a schematic image of the internal structures with a dense skin layer on the patterned side and a finger-like structure in the sublayer.

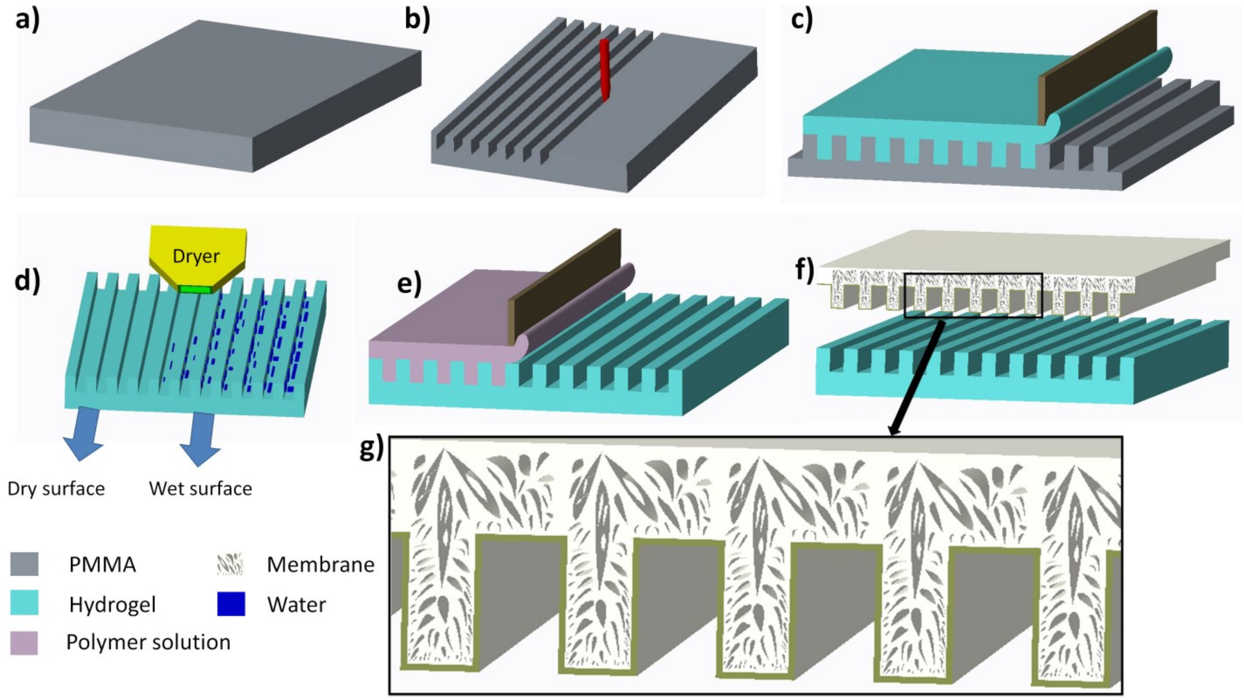

Figure 2. 1. Schematic illustration of the preparation steps of the patterned membranes. (a) Fabrication of the master mold. (b) & (c) Casting the hydrogel solution on the master mold and drying the hydrogel surface. (e) & (f) Casting the polymer solution on the hydrogel mold and wait until phase inversion to be completed. (g) Schematic image of the internal structures prepared by this method.

2.2.5 Preparation of the NIPS membranes

Information about the procedure of preparing the NIPS membranes can be found in [73]

2.2.6 Characterization

For each membrane, a consistent filtration protocol was followed. All filtration experiments started by compacting the membrane with distilled water at 3 bar for 30 minutes (this time was enough to get flux change less than 2%). Then, the TMP was lowered to 2 bar, and PEG solution was used as a feed to the cross-flow system. After collecting 70 grams, a sample from the permeate was collected to measure the rejection. Data were recorded every 30 seconds using a balance and converted into LMH (L m^{-2} h^{-1}) using Equation (1):

$$\mathbf{J_w = \frac{Q}{A \times \Delta t}} \tag{2.1}$$

where J_w, Q, A, and Δt are the water permeate flux (L m^{-2} h^{-1}), the measured amount of permeate (L), the surface area (m^2), and the sampling time (h). For evaluating the rejection, samples from the feed and the permeate solutions were collected after one hour and analyzed using total organic carbon (TOC) analyzer (Shimadzu, model TOC-V; detection range 3–25,000 mg/L, Kyoto, Japan) to measure the concentration of PEG. The following equation was used to measure the PEG rejection:

$$\mathbf{R = \left(1 - \frac{C_p}{C_f}\right) \times 100} \tag{2.2}$$

where C_p and C_f are the concentrations of the PEG in the permeate and the feed, respectively. The original area of the HFPS membranes is 100 cm^2 and the area of the tested pieces is 20.6 cm^2. The same procedure was applied for when using the BSA feed solution; however, the filtration time was 100 minutes.

A schematic diagram is shown in **Figure 2.2** of the cross-flow filtration system; the feed water passes tangentially along the membrane surface and the pressure difference across the membrane channel drives the water through the membrane. The solution that passes over the membrane surface and returns to the feed tank is known as retentate, while the one that passes through the membrane is known as permeate. The parameters used for the filtration tests are: The flow rate: 150 g/hr and the actual area of the testing cell is 0.00206 m^2. The cell type is Sterlitech CF016A with a slot depth and width of 2.3 mm and 40 mm, respectively.

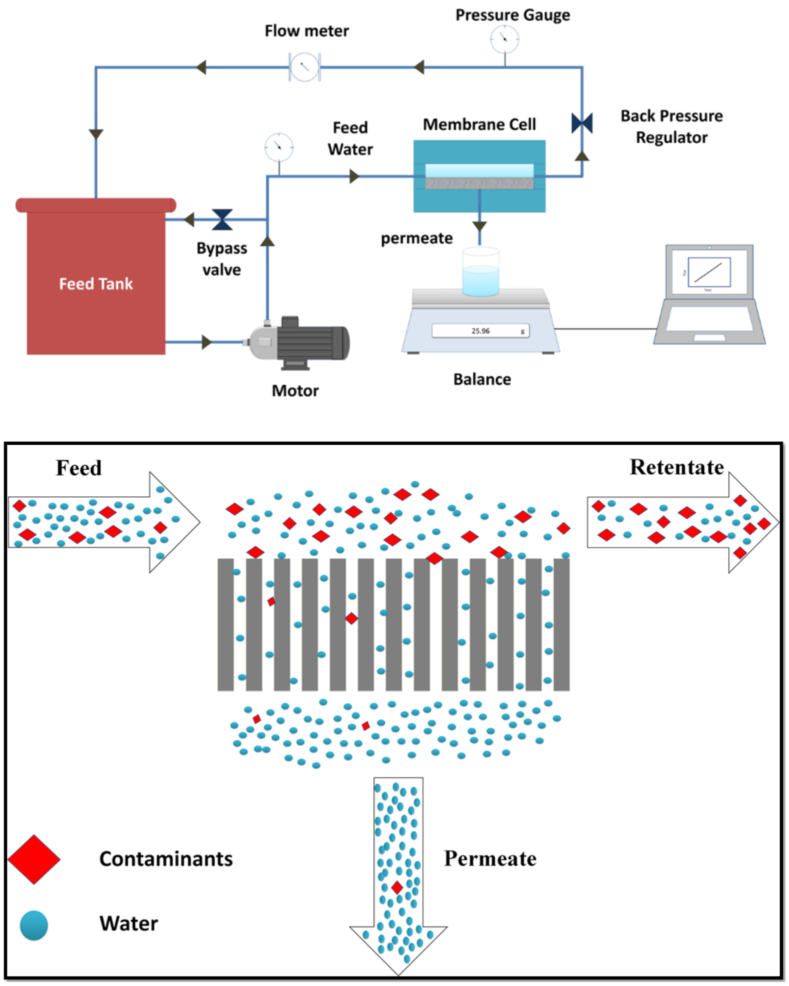

Figure 2. 2 (a) Schematic diagram of the cross-flow filtration system used in this paper. (b) A schematic diagram of the filtration mechanism inside those membranes.

Field-emission scanning electron microscopy (FESEM) was used to examine the surface and the cross-section of the membrane samples. Membrane samples were dried overnight and frozen in liquid nitrogen before fracturing. Prior to imaging, the samples were coated with a 2 nm gold layer using a Denton gold sputter unit. Image J software was used to measure the increase in the surface area from the cross-sectional images obtained by SEM. Surface wettability was measured using a contact angle measurement device (KRUSS - DSA100), where 1 µL of water was deposited on a dry membrane surface and the angle was recorded directly. The pre-wetting procedure was performed by applying a drop on the membrane surface and waiting for 5 minutes until the drop was completely absorbed, followed by depositing another water drop on the same spot and recording the contact angle.

The porosity of each membrane was calculated gravimetrically using Equation (2.3) [74]. From each membrane, samples were cut and soaked in water overnight until it's fully saturated, then weights of the wet samples were measured using a balance with ensuring no water excess on the sample surfaces. Then the samples were dried overnight at 60 ºC in an oven.

$$\boldsymbol{\varepsilon} = \left(\frac{(\mathbf{m_{wet}} - \mathbf{m_{dry}})/\boldsymbol{\rho}_\mathbf{w}}{(\mathbf{m_{wet}} - \mathbf{m_{dry}})/\boldsymbol{\rho}_\mathbf{w} + \frac{\mathbf{m_2}}{\boldsymbol{\rho}_\mathbf{p}}} \right) \times \mathbf{100} \tag{2.3}$$

Where, $\boldsymbol{\varepsilon}$ is the % porosity of a membrane, $\mathbf{m_{wet}}$ is the weight of the wet membrane sample (g), $\mathbf{m_{dry}}$ the weight of the dry membrane sample (g), $\boldsymbol{\rho}_\mathbf{w}$ the density of water ($\mathbf{g/cm^3}$) and $\boldsymbol{\rho}_\mathbf{p}$ is the density of the polymer ($\mathbf{g/cm^3}$). Four samples from different membranes were used to measure the porosity. The porosity of the HFPS patterned, unpatterned and the NIPS membranes are 0.83, 0.83 and 0.84, respectively.

The average pore size was calculated using the water filtration velocity method, using the following equation [74]:

$$\mathbf{r_m} = \sqrt{\frac{(\mathbf{2.9} - \mathbf{1.75\varepsilon}) \times \mathbf{8\gamma\delta Q}}{\boldsymbol{\varepsilon} \times \mathbf{A} \times \Delta\mathbf{P}}} \tag{2.4}$$

Where, $\mathbf{r_m}$, is the average pore radius, $\boldsymbol{\varepsilon}$ is the porosity of the membrane sample, $\boldsymbol{\gamma}$ is the water viscosity (8.9×10^{-4} Pa.s), $\boldsymbol{\delta}$ is the thickness of the membrane sample, $\mathbf{Q}$ the water flow rate ($m^3.s^{-1}$) and $\Delta\mathbf{P}$ is the transmembrane pressure (0.3 MPa).

2.3 Results and discussion

2.3.1 SEM images

Figure 2.2. shows surface and cross-sectional SEM images of different membranes prepared using hydrogel molds. The internal structure is hierarchical finger-like which is typical for the immersion precipitation phase separation membranes. The simplicity of this method expands its capability in producing big features, as shown in Figures 2a and 2b where the height of the ridge is ~530 µm. Moreover, it can produce uniform patterns which are suitable for filtration purposes, as shown in Figure 2c, where the height and the width of the features are 100 µm and 270 µm, respectively. A particular advantage of this method is the wide range of the available features that can be produced, where any replicated feature by hydrogel can be applied on the membrane surface (Figure 2.2e and 2.2f).

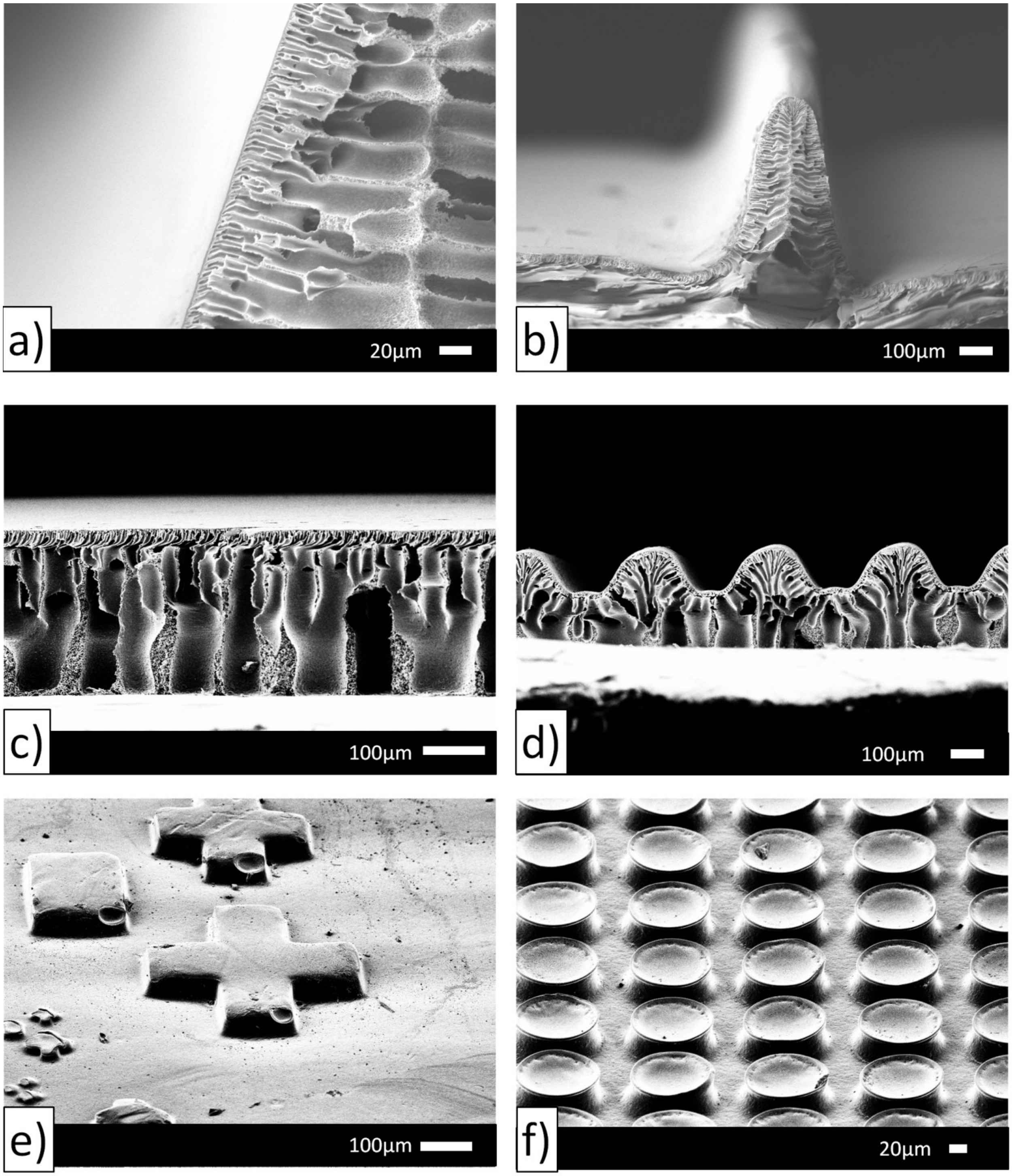

Figure 2. 3. Scanning electron microscope images of the prepared membranes. (a) a cross-section of a ridge membrane and the (b) the full cross-section of the ridge to show the total height which is around 530 µm. (c) and (d) show an un-patterned membrane prepared using hydrogel and a

uniformly patterned membrane, which were used later for filtration experiments. (e) and (f) show the morphologies of other patterned membranes.

Nature provides us with a variety of naturally occurring micro/nano features that exhibit many inspiring phenomena, such as the self-cleaning effect of the lotus leaf, [75] the superhydrophilic surfaces of pitcher plants,[76] the ability of water striders to walk on water [77] and the antifouling properties of shark skin [78]. With our soft lithography molding via hydrogels of phase inversion membranes, many of these types of structures can now be easily integrated with water filtration technologies. For example, white bass fish (Figure 2.3a) scales were obtained from a supermarket and used to study its topography. SEM images show that the surface topography of this type of scale consists of grooves in a radial direction (radii), ridges distributed in the form of circular rings (Figure 2.3b) and lateral circular ridges (Figure 2.3c). Figures 2.3d and 2.3e show a micro-structured membrane surface replicated from a fish scale master as a demonstration of this method to reproduce different bioinspired structures on the membrane surface.

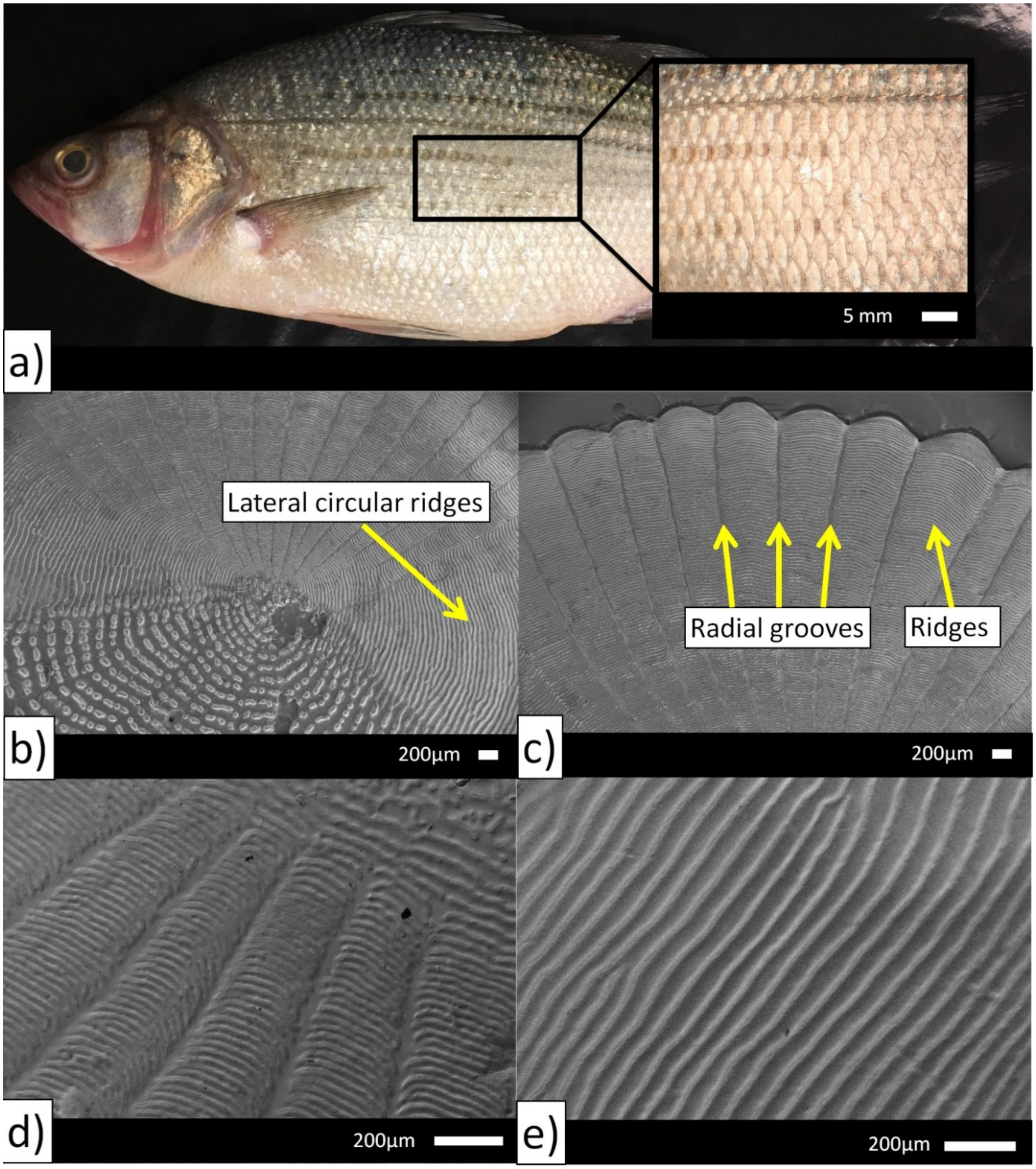

Figure 2. 4. The replication of fish scale topography on a membrane surface. (a) a whole white bass fish, (b) and (c) SEM images of a fish scale removed from the fish, (d) and (e) SEM images of patterned membranes replicated from a fish scale.

2.3.2FTIR

The surface chemistry of the hydrogel and conventionally produced membranes was examined using FTIR, as shown in Figure 2.4a. Both types of membranes showed the same trend indicating that the hydrogel molding technique does not affect the chemical property of membranes. The contact angle measurements for the patterned-hydrogel, the unpatterned hydrogel and the conventional membranes are shown in Figure 2.4b. Generally, the contact angle measurements are used to evaluate the wettability of the membrane surface, with the lower contact angles indicating higher wettability which can enhance the water permeation through the membrane [32].

2.3.3 Contact angle (CA)

The contact angle measurements for the dry samples of patterned-hydrogel, unpatterned-hydrogel and the conventional membranes were 43°, 58°, and 56°, respectively. In the case of pre-wetted samples, again, the contact angle decreased to 52° for both the unpatterned-hydrogel and the conventional membranes and 32° for the patterned one. However, since hydrogel is not changing the chemical properties of the membrane surface, the reduction in the contact angle for the patterned membrane is due to the existence of the patterns, which changes the physical property of the surface for Wenzel wetting [79].

2.3.4 Filtration experiments

Figure 2.4c shows the pure water flux results and PEG rejection for the three types of membranes. All filtration experiments were conducted using a cross-flow filtration system. The filtration experiment was conducted for each membrane in two stages; filtration with distilled water (pure water flux tests) and filtration with PEG solution. A consistent filtration protocol was applied for each filtration test (see the experimental section). The pure water flux results for the patterned-hydrogel and the unpatterned-hydrogel membranes increased significantly by 8 and 4 times as compared to the conventional membrane, respectively. Moreover, the patterned-hydrogel membrane has doubled the water flux compared to the unpatterned-hydrogel membrane. It can be observed from Figure 2.4c that the rejection results of the HFPS membranes for PEG ($M_w = 35$ kDa) were almost similar. However, the HFPS membranes showed lower rejection by almost 50% compared with the NIPS membrane. There are several possible explanations for those results. First, the skin layer of a membrane prepared by the NIPS method is denser than that of HFPS method. In both methods, the skin layer is formed by gelation and the porous sublayer is the result of liquid-liquid phase separation through nucleation and growth [80,81]. In the NIPS method, immediately after immersion of casting solution, there is a rapid depletion of solvent and a relatively small penetration of non-solvent. This results in high polymer concentration at the polymer film/non-solvent bath interface and thus the formation of a dense and thin gel layer. This so-called skin layer restricts the solvent out-diffusion, and the demixing at the sublayer occurs at lower polymer and higher non-solvent concentrations, mainly governed by liquid-liquid phase separation [81]. In the HFPS method, however, the hydrogel material itself acts as a resistance for the rapid transport of solvent toward the non-solvent at the interface. Hence, the mechanism of formation of the skin layer is governed by both gelation and liquid-liquid phase separation. The second reason for the significant improvement of HFPS membranes can be attributed to the addition of patterns that increases the surface area, which should be directly proportional to the water flux; in this case, the increase in the surface area was 23%. Finally, the absence of the secondary skin layer in the HFPS membranes, which typically results from the adhesion of the polymer to the glass plate in NIPS membranes, reduces another resistance against water transport [82]. In the HFPS membranes, the other side of the cast solution, which is not in contact with hydrogel, is exposed to air; therefore, the polymer on the top surface is not attached to any solid surface. The average pore size for the prepared membranes was calculated using Guerout-Elford-Ferry equation (Equation 4) [74]. The pore sizes of patterned-hydrogel, unpatterned hydrogel and conventional membranes were 57±3, 41±3, and 16±1 nm, respectively, which is in the range of UF membranes [17]. The variations in the pore sizes of the two methods can be attributed to the slow demixing rate between the solvent and the nonsolvent. In fact, the morphology of membranes produced by HFPS method lies between two extremes: NIPS and vapor-induced phase separation (VIPS). In the VIPS method, casting solution is in contact with a vapor as a non-solvent and the membrane formation would be merely based on non-solvent inflow, which generates microporous membranes without a skin. In the second stage, we tested the fouling propensity of the prepared membranes via filtration experiments using a model protein solution. Figure 2.4.d shows the flux decline over time for the HFPS patterned and unpatterned membranes using BSA solution at fixed transmembrane pressure (TMP). As can be observed, the patterned membrane could maintain the higher initial water flux and even showed 78% increase compared to the unpatterned membrane after 100 min filtration. It is worth noting that the flux enhancement was obtained with a minor sacrifice in rejection (66% for the patterned and 68% for the unpatterned) of BSA. Since the patterned membrane starts at a higher initial flux, an increase in the transport resistance due to the accumulation of foulants on and/or in the membrane surface is expected to be higher than the unpatterned one [83]. This may result in a severe flux decline, especially at the start of the filtration experiment causing pore narrowing. Although the deposition of foulant materials on the patterned membranes might be more severe, particularly in the dead zones of valleys, the less fouled upper areas of the ridges maintain higher flux as compared with the unpatterned ones. The latter is attributed to higher local shear stresses at the top of the ridges reported to be higher than the unpatterned membrane, resulting in less fouled areas [49].

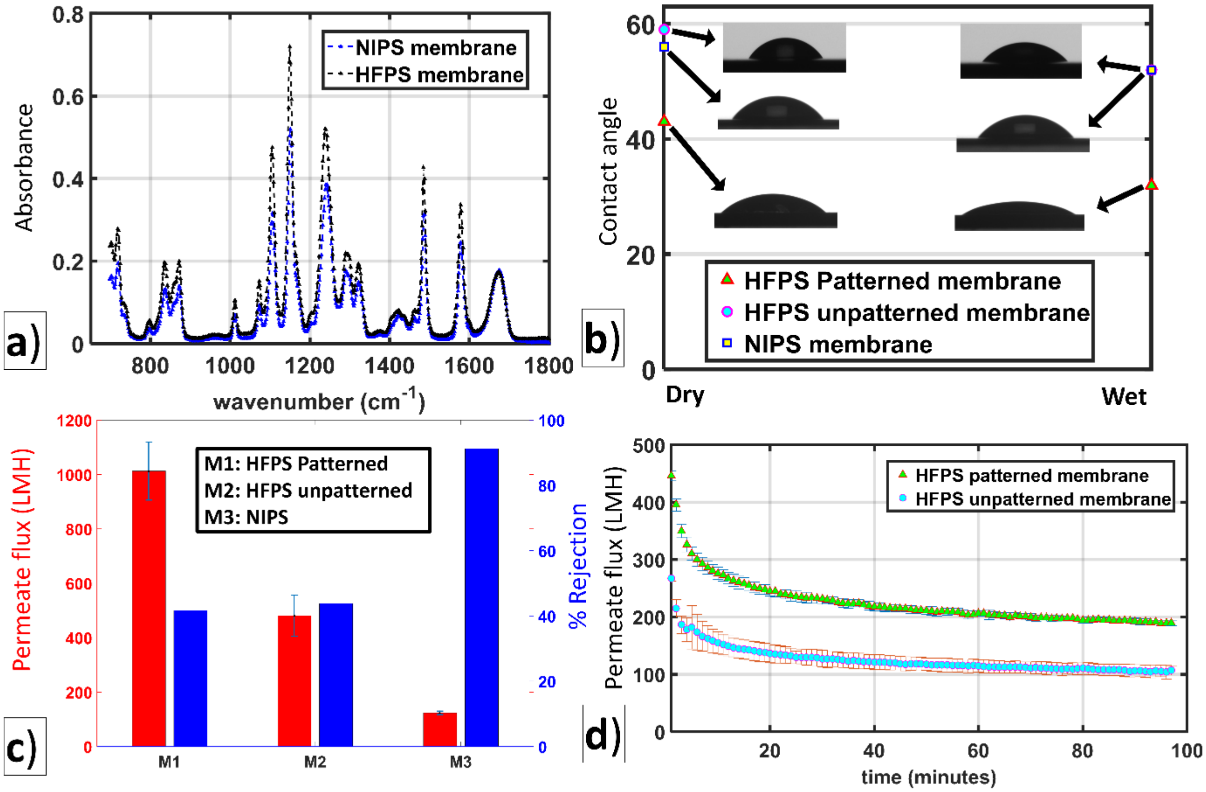

Figure 2. 5. Characterization results of the prepared membranes. (a) FTIR spectra of NIPS and HFPS membranes. (b) Contact angle measurements of three samples for both NIPS and HFPS membranes using dry and wet samples, where the direction of the images was taken perpendicular to the ridges. (c) Pure water flux and PEG rejection results of three membrane samples (HFPS and NIPS) and the statistical average is provided herein. (d) Flux decline vs. time of the HFPS membranes by BSA as a feed solution (Number of replicates is 3).

2.4.5 the cross-sectional analysis of the prepared membranes

The internal structure of the conventional NIPS and the HFPS membranes is presented in **Figure 2.5**. All membranes have asymmetric finger-like structures with a thin dense layer supported by a porous sublayer. HFPS method has resulted in twice thicker skin layer but with higher average pore size compared with NIPS. The thicker skin layer of HFPS membranes can be explained by looking at the effect of interfacial polymer concentration at the onset of phase inversion. Generally, a higher interfacial concentration of polymer, which can be a result of slower nonsolvent inflow relative to solvent outflow, leads to the formation of a thicker skin layer [80]. In contrast to the conventional NIPS, in the HFPS method, the solvent is located on the top and the nonsolvent at the bottom in the hydrogel solution. This upside-down configuration, along with the hydrogel material resistance against materials transport, significantly hinders the diffusion of nonsolvent in the cast film. The existence of PVP in the hydrogel molds can potentially intensify this effect due to the higher affinity of PVP molecules to water, as well as their large size to pass through the hydrogel barrier. Moreover, the slow rate of non-solvent and solvent demixing also results in a thicker membrane [84-86].

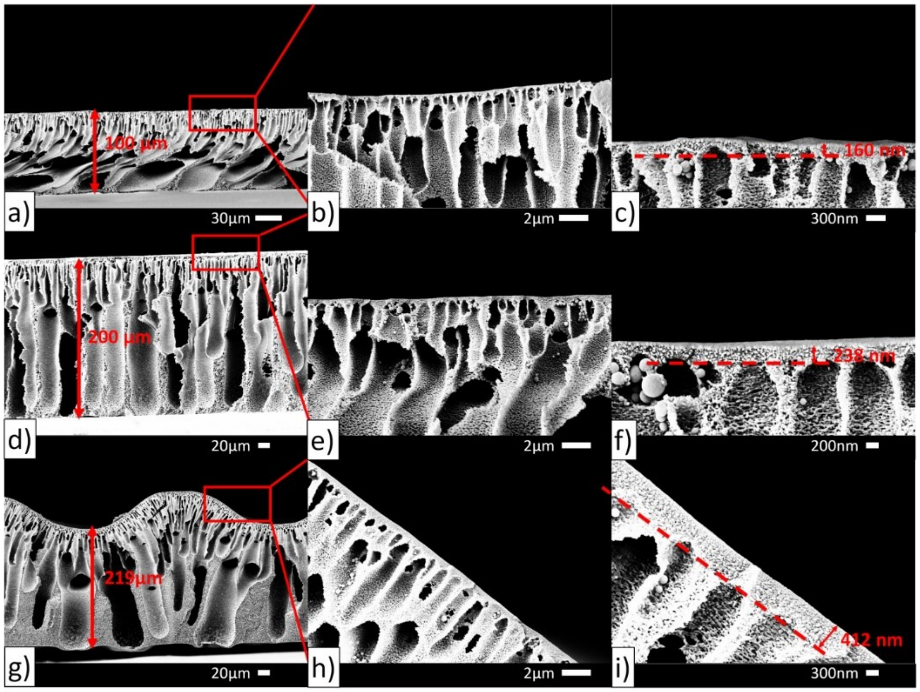

Figure 2. 6. Cross-sectional FESEM images of the conventional membrane (a-c), the hydrogel unpatterned (d-f), and the hydrogel patterned membranes (g-i) with different magnifications.

The transport phenomena in hydrogels happen inside the water-filled areas; therefore, any factor affecting those areas will impact the rate of materials transport (here solvent, water, and additive) inside the hydrogel [87]. Many factors can affect this diffusion rate, such as the hydrogel thickness, the polymer concentration in the hydrogel, the polymer chain radius, and the solute hydrodynamic radius. This means that hydrogel offers a new way to control the type of membranes to either have symmetric or asymmetric internal structures by simply controlling the demixing rate of solvent/non-solvent [73,88]. Another potential advantage for the hydrogel molding technique is the ability to investigate different surfactants in the non-solvent, which was not feasible to study with the conventional method due to the huge amount of waste material that has to be used every time. These results do not show the full capabilities of our method, and many future improvements may be achieved with the introduction of a reliable micropatterning method for phase inversion formed membranes. Based on the literature, specific features may form re-circulation zones and eddies on the membrane surface, resulting in the mitigation of the fouling phenomenon [89-91].

2.4 Conclusion

In summary, we have demonstrated a novel method to produce patterned membranes through a structured mold with high non-solvent content that can initiate the phase separation molding by creating a dense surface on the structured side of the membrane. Hydrogel molding can produce many different patterns and geometries on the membrane surface, allowing for a much-expanded design space when developing high-flux and antifouling membranes. Initial results showed that the HFPS membranes significantly increased the water flux compared with the conventional membrane due to an overall increase in the porosity of their skin layer. Moreover, the hydrogel-based membranes showed that the patterned membrane doubled the water flux compared with the unpatterned one and can likely be increased to higher values by optimizing the patterns' dimensions.

Chapter 3

Durability and Recoverability of Soft Lithographically Patterned Hydrogel Molds for the Formation of Phase Separation Membranes

3.1 Introduction

Membrane technology is a well-established method for the highly selective separation of a wide variety of contaminants from water [19,59,92,93]. Despite many advantages, membrane separation processes are faced with two critical challenges [94]. The first problem is fouling of the membranes with contaminants, which reduces water flux over time. Membrane fouling is defined as the attachment and accumulation of dissolved materials (water contaminants) or suspended particles on the membrane surface and internal pores. The fouling results in a dramatic reduction of the membrane performance with time and reduces its life span [95-97]. The second major challenge is the trade-off relationship between permeability and selectivity of membranes [98]. As permeation characteristics of membranes improved, the rejection capability is reduced [99]. To improve membrane performance and lower the membrane fouling, chemical treatments [100,101] or physical modifications [27,102] have commonly been attempted by either coating the membrane surface with hydrophilic/hydrophobic layers or modifying the membrane matrix by blending with additives (such as nanofillers, surfactants, and polymeric additives). However, these approaches suffer from many disadvantages which restrict their extended applications in practice. Leaching of additives out of the polymer matrix and detachment of surface-coated materials even in mild filtration conditions have been widely reported in the literature [33,103,104].

As an alternative to coatings and surface treatments, membrane surface patterning has recently attracted attention [105,106]. Tailoring the topographical surface of a polymer membrane can theoretically increase the effective surface area, which is directly proportional to the permeate flux. Therefore, the trade-off between permeability and selectivity is partially avoided because a higher effective area is fit into a smaller system, and permeation is significantly increased without sacrificing the selectivity [107]. Furthermore, patterns on the membrane surface can create secondary flows that boost the fluid shear at the vicinity of the membrane surface for certain designs leading to a higher antifouling property for some applications [89,108].

Over the last decade, there have been many efforts to develop new techniques to fabricate membranes with micro and nano-sized features [26,109-114]. The current methods to fabricate patterned membranes can be classified as either mold-based patterning or direct printing approaches [109-112]. In the mold-based patterning, phase inversion micromolding (PSμM) [46] and thermal embossing micromolding [115], a solid mold is used to produce the features on the membrane surface. More recently, micropatterned anion exchange membranes have been fabricated using 3D printing techniques [116]. Although these methods have succeeded in producing patterned membranes, some drawbacks are encountered. In the PSμM, the polymer solution is cast on the mold and dipped in the coagulation bath to start the phase separation process. However, this method results in a pattern replication on the backside of the membrane. The active surface - the face which contacts the non-solvent first - is still unstructured [48]. Despite the progress in using different phase separation methods to modify the PSμM, this method is limited in the membrane types that are compatible with the technology [62]. Thermal embossing compresses the surface of previously manufactured membranes to form surface features but damages the internal structures of the membrane due to the application of high pressure (around 15 bar) and temperatures in the fabrication procedure. There is also an inverse relationship between the height of the features and the membrane permeation response such that an increase in the height of patterns results in a lower flux [117]. In contrast to the PSμM and thermal embossing approaches, direct 3D printing of membranes is in its initial stages of development and currently suffers from limited pattern resolution, materials choice, and poor scalability [105].

Hydrogels are water-swollen cross-linked polymers that hold and retain high contents of water owing to their 3D network structure [68]. The existence of water in hydrogel plays a crucial role in the overall diffusion of solutes within the gel matrix [118]. The unique properties of hydrogels in terms of solute uptake and release expand their applications in many fields such as drug delivery [119], tissue engineering [69], cell culturing [70], and biomedical applications [72]. Recently, we reported a novel fabrication method for porous patterned membranes relying on the high water content of micropatterned hydrogel molds named “hydrogel facilitated phase separation (HFPS)” [26]. It was shown that different patterns and shapes successfully replicated on the membrane surface without affecting the membrane’s surface chemistry. The fabricated HFPS membranes have an asymmetric structure containing finger-like pores on the bottom and a dense skin layer on top similar to the conventional non-solvent induced phase separation[104,120]. Reusability of the hydrogel mold is of interest to lower the cost and time required for large-scale membrane fabrication. In the HFPS process, a thin layer of polymer solution (consisting of polymer and solvent) is cast on a hydrogel mold, and due to the high content of water in the hydrogel phase, separation starts at the interface. The solvent from the polymer solution exchanges with the nonsolvent from the hydrogel mold, forming a porous membrane structure. The gradual buildup of the solvent within the hydrogel mold during consecutive membrane fabrication lowers the performance of the mold from the ideal initial condition. Thus, the phase separation process is slower since the concentration gradient between the nonsolvent-filled mold and solvent/polymer mixture is less, resulting in different membranes from each casting. In this study, we investigated the effect of continuous usage of hydrogel mold on membrane performance over time. No available studies, to our best knowledge, investigated the reusability of hydrogel molds for membrane applications. Herein, we developed a procedure to extract the diffused solvent inside hydrogel during the HFPS method to recover the performance of the fabricated membrane into its initial state. This study provides an insight into the continuous fabrication of HFPS membranes using hydrogel molds.

3.2 Materials and methods

3.2.1 Chemicals

Polyethersulfone (PES, Baden Aniline and Soda Factory (BASF) Ultrason E6020p, Mw = 58 kDa), PVP (Sigma-Aldrich, Mw = 350 kDa), and N, N-dimethylacetamide (DMAc, Sigma-Aldrich), were used to prepare polymer casting solutions. Agarose (Sigma-Aldrich, chemical abstracts service (CAS) number: 9012-36-6) was used to make hydrogel solutions. PMMA (McMaster-Carr) was used to develop master molds. Membrane rejection performance was evaluated through filtering of Dextran (Mw = 500 kDa). All materials were used without any modifications.

3.2.2 Preparation of polymer solution

PES polymer solution was prepared by mixing 15 wt% PES, 2 wt% PVP and 83 wt% DMAc and then stirred in a beaker overnight at room temperature until the solution reached a homogeneous state. Thereafter, the beaker containing the polymer solution was placed to rest at room temperature for one day and then used for membrane fabrication.

3.2.3 Preparation of HFPS membranes

Hydrogel solution was prepared using the microwave method in which 5 wt% Agarose was mixed with distilled water then heated using a microwave until boiling. The solution was cast on a patterned acrylic master mold, with a thickness of 1.6 mm and left for gelation (2-3 minutes). The hydrogel mold was gently removed from the master mold and placed on a glass plate with the patterns face up. The polymer solution was subsequently hand cast using a Gardco film applicator on top of the hydrogel mold with a gap thickness of 200 µm. The assembly was kept under a fume hood until the membrane was fully formed (approximately 1 minute). Then the membrane was gently peeled off the hydrogel mold and placed in a distilled water bath for later use.

3.2.4 Characterization

3.2.4.1 Membrane morphology

The cross-sectional images of the membranes were examined using field emission scanning electron microscopy (Zeiss Sigma FESEM). Membrane samples were dried overnight at room temperature and broken in liquid nitrogen and then coated with a gold layer (~2nm thickness) using Denton gold sputter to aid in SEM imaging.

3.2.4.2 Water content and average pore size

The average pore size of each membrane was calculated based on water filtration velocity method [102]:

$$r_m = \sqrt{\frac{(2.9 - 1.75\varepsilon) \times 8\gamma\delta Q}{\varepsilon 2.9A \times \Delta P}} \tag{3.1}$$

where r_m is the membrane average pore size, ε is the membrane porosity, δ is the thickness of the membrane, γ is the viscosity of water (8.9×10^(-4) Pa s), Q is the flow rate of water passing across the membrane (m^3/s), A is the membrane surface area (m^2), and ΔP is the transmembrane pressure being applied (0.28 MPa). The porosity of each membrane was calculated by a gravimetric method following a standard procedure from the literature [26,73]. From each membrane, samples were cut and immersed in distilled water overnight. The wet membrane samples (m_{wet}) were weighed using a digital balance after ensuring there is no excess water on the membrane surface. After that, the membrane samples were dried overnight at 60 ºC and weighed in dry conditions (m_{dry}). The porosity of the membrane ε, is found using:

$$\varepsilon = \left(\frac{(m_{wet} - m_{dry})/\rho_w}{\frac{m_{wet} - m_{dry}}{\rho_w} + \frac{m_{dry}}{\rho_p}} \right) \times 100 \tag{3.2}$$

where m_{dry} is the weight of a dry membrane (g), m_{wet} is the weight of a dry membrane sample (g), ρ_w and ρ_p are the densities (g/cm^3) of the water and polymer, respectively.

3.2.4.3 Filtration tests

The water filtration experiments of HFPS membranes were conducted using a dead-end filtration system shown in Figure 3.1. The surface area of a Millipore cell (Amicon® Stirred Cell 400mL) was 41.8 cm2 and the applied transmembrane pressure was 40 psi. The flux results were calculated using

$$J_w = \frac{Q}{A\Delta t} \tag{3.3}$$

where J_w is the permeated water flux through the membrane (L/(m^2 h)), A is the membrane surface area (m^2), Q is the amount of permeate (L), and Δt is the sampling time intervals.

3.2.4.4 Solute rejection

In order to measure the dextran rejection, samples from the permeate and the feed solutions were collected and analyzed using total organic carbon (TOC) instrument (Shimadzu, model TOC-V; detection range 3–25 000 mg L−1, Kyoto, Japan). The rejection and the measured concentrations are related as follows,

$$R = \left(1 - \frac{C_p}{C_f}\right) \times 100 \tag{3.4}$$

where the C_p and C_f is the solute concentration in the permeate and feed samples, respectively.

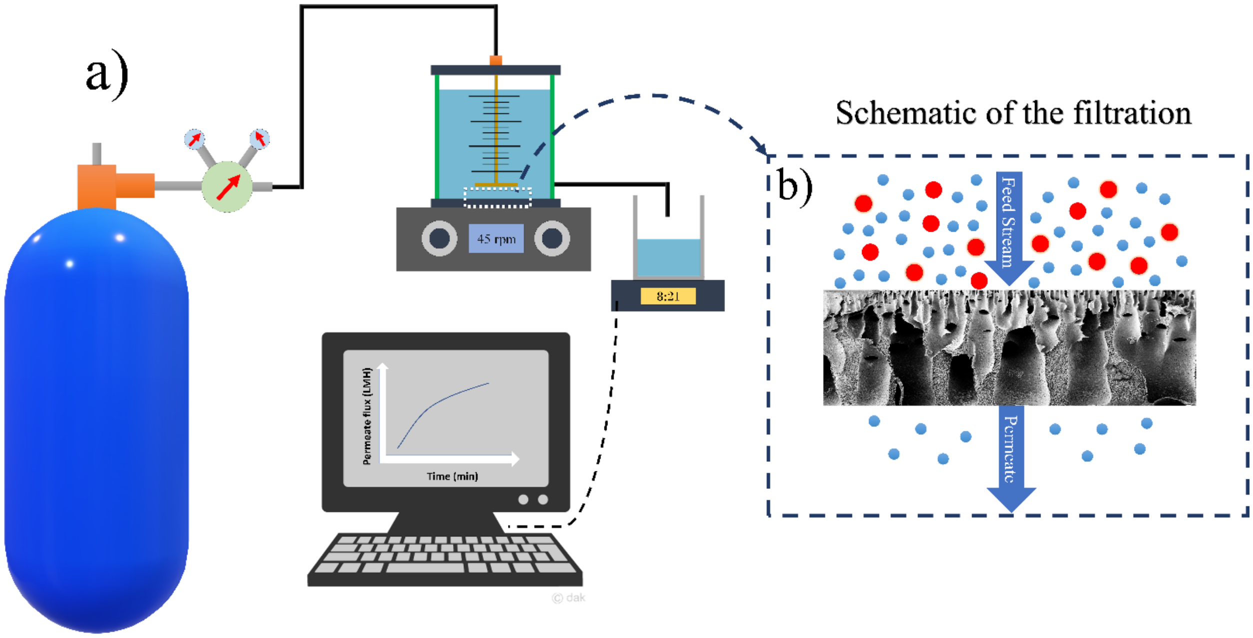

Figure 3. 1. Schematic diagram of (a) the dead-end filtration system and (b) the filtration mechanism in the membranes.

3.2.5 Treatment methodologies

The time of treatment required to recover a hydrogel mold is crucial for continuous and large-scale productions. An ideal treatment plan would fully extract the solvent from hydrogel molds without damaging its structure in a short time with minimum energy and material requirements. When a hydrogel mold is used in phase separation, the de-mixing process between membrane polymer solvent (DMAc) and nonsolvent (water) changes the hydrogel liquid content. Thus, using the same hydrogel mold for another casting leads to a membrane with different characteristics compared to the initial trials due to the presence of solvent within the mold. The membranes replicated from an untreated hydrogel mold were denoted as M1_pristine, M2_untreated, and M3_untreated, in which the numbers (1, 2 and 3) represent the order of castings. For the case of untreated hydrogel, the mold was placed in a water bath for 10 minutes at room temperature and then air-dried for four minutes and used again. To ensure consistency in the characteristics of the fabricated membranes, the initial state of the mold should be recovered after any castings. Here, two methods are proposed for hydrogel treatment, the first one is based on cold treatment (long-term), and the second one involves heat treatment (short-term).

3.2.5.1 Cold treatment (Long-term)

For long-term treatment, after each membrane casting, the hydrogel mold was flushed with water, and it was placed in a distilled water bath (0.5 L) at room temperature for three days, which allows for natural diffusion of residual DMAc. Before membrane casting, the mold was again flushed with water then gently forced air applied to the hydrogel surface to remove excess water for four minutes. The membranes produced from a cold treated hydrogel were denoted as M2_cold, M3_cold, M4_cold and M5_cold.

3.2.5.2 Heat treatment (short-term)

After each membrane casting, the hydrogel mold was placed in a warm distilled water bath (50 ºC) for a time between 5-10 minutes and then placed in a room temperature distilled water bath (23 ºC) for 4 minutes. After that, the surface of the mold was air-dried using pressurized air for 4 min. The membranes produced from a heat-treated hydrogel were denoted as M2_hot, M3_hot, and M4_hot. The drying process was included in both treatments to remove the residual water at the surface of the hydrogel mold as it affects the phase separation process. The temperature of the warm water bath was chosen to be 50 ºC as its high enough to increase the diffusivity within hydrogel diffusivity while remaining well below the melting point temperature (80 ºC) of the agarose to avoid damaging the hydrogel structure.

3.3 Results and discussion

The effect of the continuous usage of a hydrogel mold without any treatment on the performance of the fabricated membrane was first characterized by field emission scanning electron microscopy

(SEM). SEM images of M1_pristine, M2_untreated and M3_untreated membranes replicated from the same hydrogel mold are shown in figure 3.2. All membranes showed a similar asymmetrical finger-like structure which is typical in HFPS fabricated membranes [26]. The thickness of the top skin layer of the membranes increased from 786 nm in the M1_pristine membrane to 1670 nm in the M2_untreated membrane and 1812 nm in the M3_untreated. This increase in the thickness is attributed to the existence of solvent inside the hydrogel mold which remained from the previous casting.

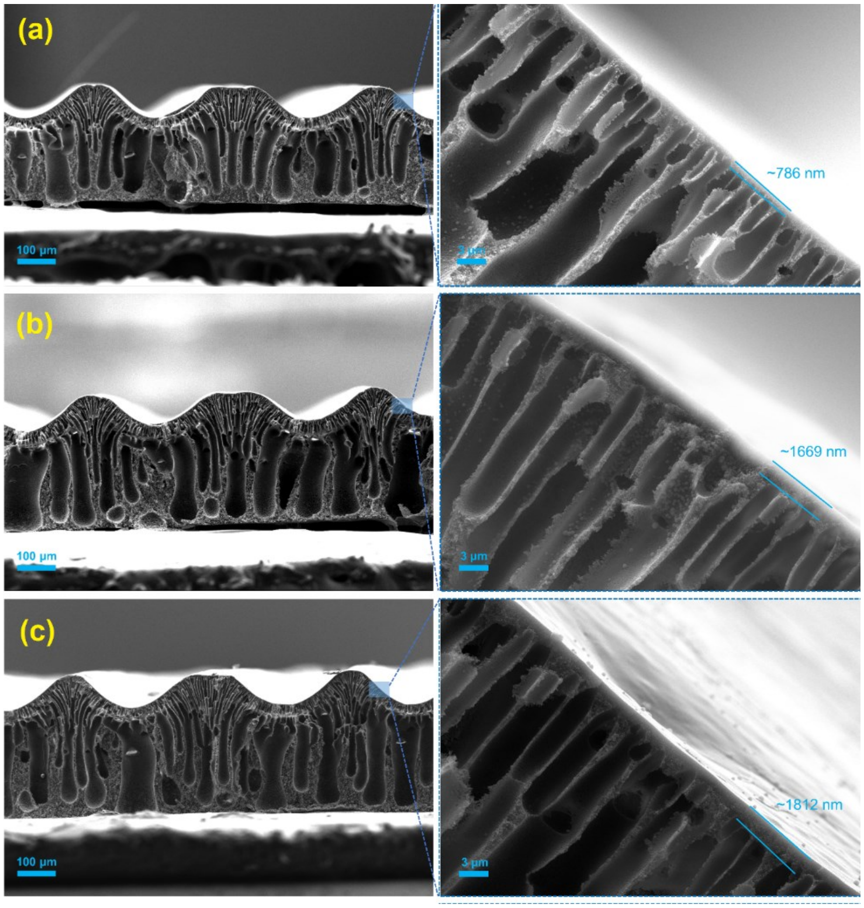

Figure 3. 2. FESEM cross-sectional images of (a) M1_pristine, (b) M2_untreated and (c) M3_untreated membranes being fabricated using the same mold without pre-treatment.

In membrane formation using a nonsolvent induced phase separation (NIPS), a three-component ternary diagram of polymer-solvent-nonsolvent describes the thermodynamics of the membrane precipitation, which is shown in figure 3.3 [121]. Each corner of the triangle represents one component, such as polymer, solvent, and non-solvent, while any point inside the triangle represents a mixture of these components. The system consists of two distinct regions, separated by a binodal curve: (i) one-phase region where all components are miscible and (ii) two phase-region where the polymer solution separates into polymer-rich that forms the solid part of the membrane, and polymer-lean that forms the pores of the membrane [122]. The entire membrane precipitation process is tracked by the path AD, where point A represents the initial polymer composition and point D represents the final membrane. Point B, on this path, represents the first precipitation of the polymer due to the demixing process between solvent and nonsolvent. As the precipitation continues, the concentration of the polymer becomes high enough to be considered a solid material (point C). The last point, D on the nonsolvent-polymer axis, indicates the porosity of the membrane [25]. The existence of solvent in the hydrogel mold increases the precipitation time, as more non-solvent solution (mixture of solvent and non-solvent) is needed to make the polymer solution thermodynamically unstable. Hence, the time required for the system to reach the first precipitation point B (being referred to as path A-B*) increases. With further increase of the solvent content inside the hydrogel, this time increases, and subsequently, the path A-B** becomes longer [123]. The precipitation time affects the morphological structure of phase separation membranes represented by skin layer thickness and average pore size.

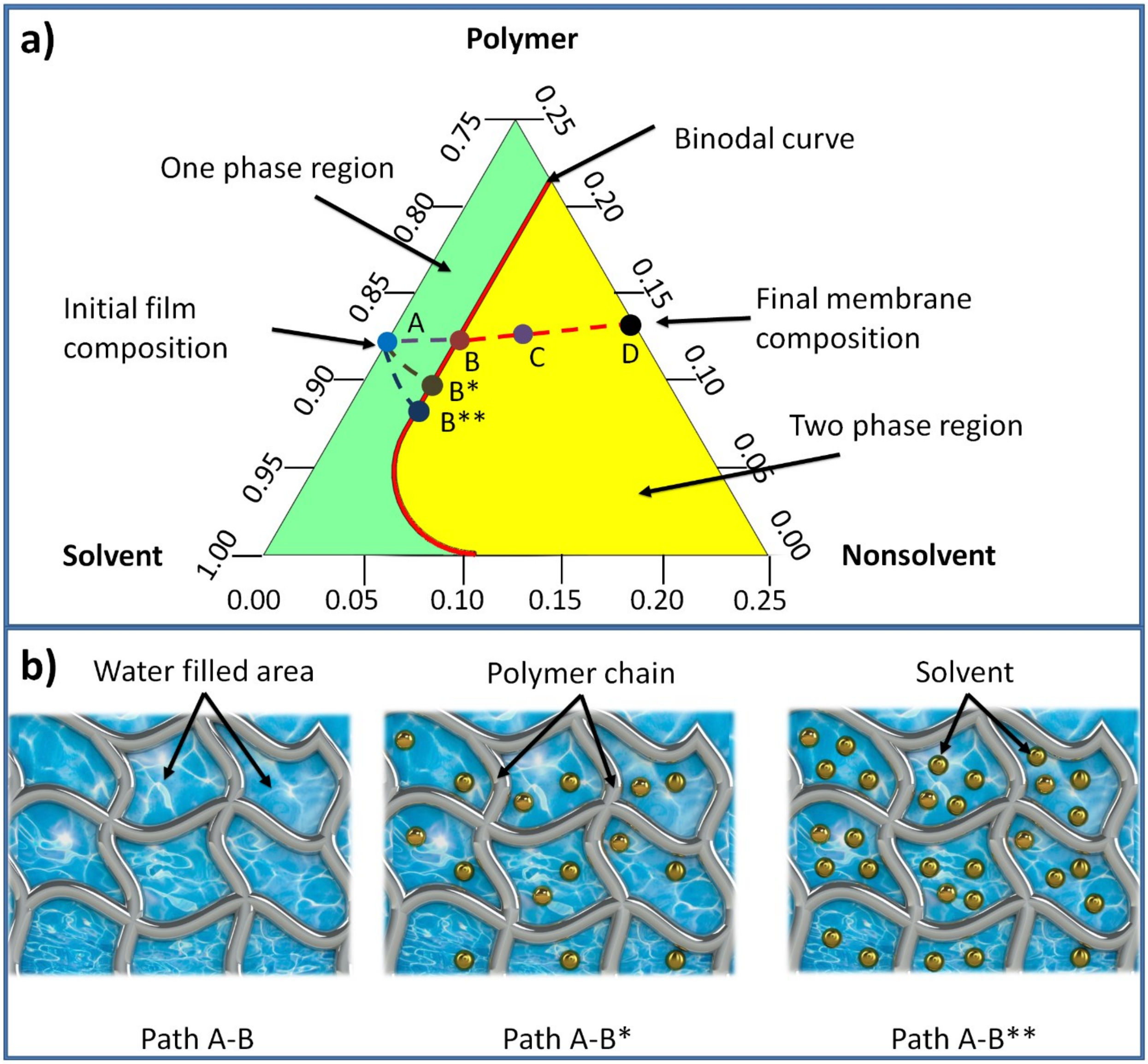

Figure 3. 3. (a) Ternary phase diagram of a polymer/solvent/nonsolvent system. (b) Schematic view of the hydrogel structure with consecutive castings without any treatment. Path A-B shows the time needed for a polymer solution to start precipitation. As the amount of solvent increases in the hydrogel due to the consecutive castings without treatment, the precipitation time becomes longer (Path A-B* and A-B**).

The pore size, pure water flux, and rejection results for the M1_pristine, M2_untreated and M3_ untreated membranes were compared and presented in figure 3.4. The average pore size calculations showed a sharp decline from 89 nm (M1_pristine) to 54 nm (M2_ untreated) and a gradual decline from 54 nm (M2_ untreated) to 51 nm (M3_ untreated). This decrease in the average pore size is due to the increase in the amount of solvent in the hydrogel mold after the first and the second castings. The combined effect of solvent in the hydrogel mold decreases the average pore size and increases the thickness of the skin layer significantly and dropped the pure water flux of M2_ untreated and M3_ untreated by 63 % and 68%, respectively. Moreover, it increased the dextran rejection of M2_ untreated and M3_ untreated by 1.7 and 2.4 times as compared with the pristine membrane (M1_pristine). These results suggest that if the hydrogel mold is not treated after each membrane casting, different membrane performance will be achieved each time.

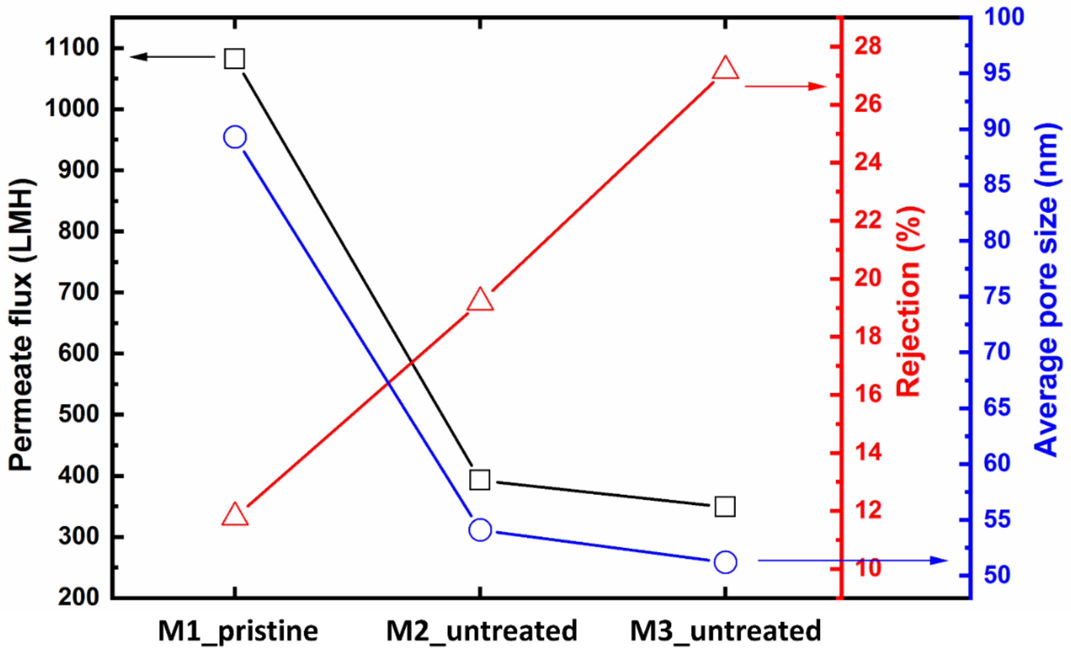

Figure 3. 4. Pure water flux of patterned membranes replicated from the same hydrogel mold. In the first three castings, the mold was just washed with pure water and then reused.

3.3.1 Cold treatment

To evaluate the cold treatment protocol, the filtration performance of patterned and unpatterned HFPS membranes was investigated for up to five castings from the same mold (Figure 3.5). The pure water flux results showed a gradual decline for both patterned and unpatterned membranes over the period of treatments. Although the cold treatment process was used on the hydrogel mold before each membrane casting, the full recovery of the pure water flux wasn't successful. This decline is attributed to (i) the existence of solvent inside the hydrogel after each casting, and (ii) the permanent deformation of the hydrogel structure. Previous studies on conventional phase separation membranes have shown that the existence of solvent in the coagulation bath decreases the effectiveness of the nonsolvent (water) and thus slows down the precipitation rate. The slower solvent/nonsolvent exchange rate was found to result in denser structures [82,123]. The permanent deformation of the hydrogel structure also reduces the water-filled areas, thus lowering the demixing rate between the solvent and the nonsolvent.

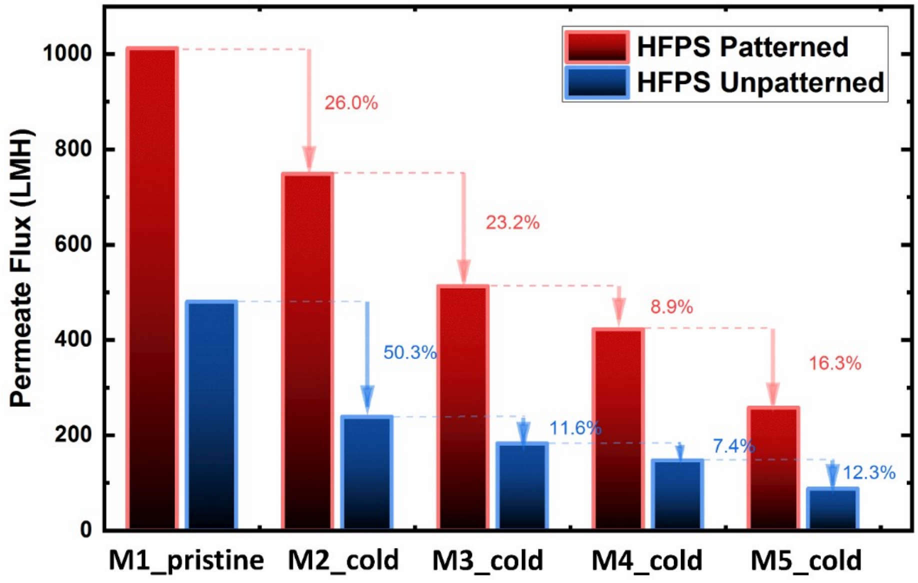

Figure 3. 5. The effect of the cold treatment process on the filtration performance of HFPS patterned and unpatterned membranes prepared from the same hydrogel molds for five castings.

3.3.2 Heat treatment

Based on the literature, factors that affect the diffusion of solute within hydrogel are the hydrogel structure (gel pore size), properties of solutes (concentration and size), diffusion time and temperature of solutes [49,50]. In most cases, the temperature of solute is increased to a mild temperature, usually between 30-50, which has proven to be an effective range for increasing the diffusion coefficient and, therefore, a better solutes extraction. Since, in our case, the hydrogel recipe and the type of solvent are fixed, the other two parameters were considered in the heat treatment process. However, increasing the temperature closer to the melting point of the agarose may damage the hydrogel structure. Therefore, as shown in Table 3.1, the temperature of the warm water bath was set at 50 ºC and the treatment time was varied to evaluate the water flux recovery. Moreover, a cold-water bath stage was added to lower the temperature and prevent the hydrogel deformation before the drying stage.

Table 3. 1. Details of heat treatments for recovery of the hydrogel mold in the patterned membrane.

Membrane Casting	**Warm water bath at 50 °C (min)**	**Cold water bath at 23 °C (min)**	**Drying time (min)**	**Average pore size (nm)**	**Dextran rejection (%)**	**Water flux recovery (%)**
M2_hot	5	5	4	72.9	19	64.2
M3_hot	7.5	5	4	82.9	18	84.4
M4_hot	10	5	4	88.1	14	96.2

Figure 3.6. shows the filtration performance, average pore size, and dextran rejection of M1_pristine, M2_hot, M3_hot, and M4_hot membranes replicated from the same hydrogel. After

the first membrane casting, the hydrogel mold went through three heat treatment process, as shown in Table 3.1. The filtration performance for the M2_hot membrane showed 64.2% water flux recovery as compared to the pristine membrane. This decline in the water flux indicates that the warm water bath time for M2_hot was not enough to extract all DMAc solvent from the hydrogel mold. The existence of solvent in the hydrogel, even if it's a small amount, has a significant effect on the morphological properties of the prepared membranes. The average pore size and dextran rejection of M2 were 72.9 nm and 19%, respectively. These results show a similar trend compared with M2_untreated in which no treatment was applied; however, M2_hot is still closer to the M_pristine due to the partial solvent extraction. In the case of M3_hot, the warm water bath time was increased, which resulted in higher water flux recovery ~84.4, from one side, and closer average pore size and dextran rejection to the original membrane (M1_pristine). As the warm water bath time increases, the flux recovery percentage increases too, confirming the importance of both time and temperature in solvent extraction. In the fourth membrane (M4_hot), the warm treatment time was 10 minutes, which resulted in a ~ 96% flux recovery. This can be attributed to a nearly full solvent extraction without damaging the hydrogel structure. Moreover, the average pore size and dextran rejection were close to those of the M1_pristine. We believe for the M4_hot case, the hydrogel mold state was similar to that of a pristine mold which then results in similarities in water flux, average pore size, and dextran rejection.

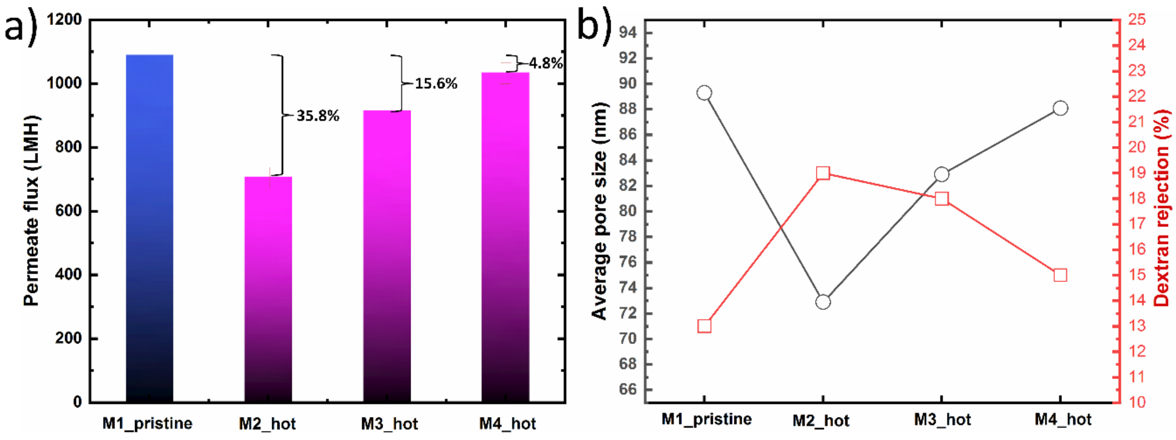

Figure 3. 6. (a) Pure water flux of patterned HFPS membranes fabricated using heat-treated hydrogel mold with an overall filtration time of 400 seconds for each membrane. (b) Average pore size and dextran rejection for the heat-treated membranes.

3.4 Conclusion

We have demonstrated, for the first time, a simple treatment process that allows repeated usage of the same hydrogel mold in micropatterned phase separation membrane castings. The formation of HFPS membranes relies on the demixing process between solvent from the polymer solution and water contained within the hydrogel mold. The change in the hydrogel mold initial state, significantly affected the membrane formation process and subsequent flux and rejection performance. Our experiments showed that the repeated use of the same hydrogel mold without any treatments resulted in a tighter membrane having a smaller average pore size and lower permeated water. Two types of hydrogel mold treatments, cold and heat, proposed in order to extract the diffused solvent from the hydrogel without sacrificing the hydrogel integrity. The proposed plans for improving mold recovery relies on enhancing the diffusion rate of solvent (DMAc) within the hydrogel to increase the degree of solvent extraction from the mold before repeated castings. In the case of the hydrogel cold treatment process, results showed that this method was lengthy and not effective in terms of water flux recovery. Alternatives, the heat treatment process showed a significant improvement in the hydrogel mold recovery represented by water flux recovery in cast membranes. The best heat treatment parameters of those that were tested were found to be 10 minutes in a warm-water bath, followed by 5 minutes in a cold-water bath and 4 minutes drying time, which resulted in 96% flux performance recovery. It is believed that this combination provided enough time for solvent extraction and relaxation of the hydrogel mold to create a similar structure and content to the pristine state. This study provides insight into the advantages and disadvantages of treatment methods that can be used for hydrogel mold recovery in the HFPS method for membrane applications and is the first step in future work to develop optimized recovery protocols for hydrogel molds intended for large scale production of patterned membrane surfaces.

Chapter 4

Gravity Assisted Super High Flux Microfiltration Polyamide-imide Membranes for Oil/Water Emulsion Separation

4.1 Introduction

The growing impact of water pollution resulting from the untreated discharge of industrial oily wastewater has severely endangered the environment and public health [124-129]. Although conventional methods of oily wastewater treatment, such as centrifugation [130], air flotation [131], and electrical/chemical coalescence [132], can effectively separate oil and water mixtures, they still suffer from the disadvantages of high operating costs, complex operational processes, large environmental footprint, and inability to remove emulsified oil (especially with droplet diameter less than 20 μm) [133-135].

Recently, membrane separation processes have become an emerging technology for effective oil separation from water owing to their high removal efficiency and small footprint [136-140]. The current trend in the membrane research area is the use of super-wetting and highly porous materials for the sustainable treatment of oil in water emulsions driven only by gravity [124,141-143]. The super-wetting property is also essential for the mitigation of membrane fouling during the separation of oil. Membrane fouling is a devastating problem caused by adsorption of oil on the membrane surface or internal pores that restricts the successful deployment of energy-efficient membrane filtration systems [12,26,127,144]. It is a widely held view that membranes with higher hydrophilicity demonstrate less tendency toward hydrophobic oil compounds [33]. So far, extensive research has been carried out to improve the membrane hydrophilicity either by bulk [145] or surface modifications [146]. Membrane bulk modifications are usually performed through the incorporation of different additives, e.g., nanomaterials, into the polymeric casting solution before the membrane preparation. Despite being straightforward, this method suffers from the leaching of the blended additives from the membrane structure during filtration [104]. As a result, the effectiveness of the prepared membrane might be reduced due to the creation of structural defects. Surface modification [147-149] is another popular method to improve membrane hydrophilicity, which can be done through chemical grafting of hydrophilic polymers, layer-by-layer (LBL) assembly of polyelectrolytes, plasma treatments, and coating of hydrophilic polymers and nanoparticles. Although the mentioned approaches could minimize membrane fouling to some extent, they have a number of limitations such as long modification steps, concerns related to scalability and robustness of the modified membranes owing to the detachment of surface coatings, and low environmental friendliness due to the use of toxic chemicals [150]. Moreover, most of these modification methods increase the membrane hydrodynamic resistance, and thus higher transmembrane pressure (TMP), or more energy, is required to achieve a specific permeation flux.

Over the past decade, surface patterning has emerged as a promising method for improving the water permeation rate due to the increase in the surface area and antifouling property of the membrane [48,112]. Recently, we have developed a new method for surface patterning, called the hydrogel facilitated phase separation (HFPS) method, where highly water-saturated hydrogel acts as a nonsolvent bath [26]. By casting a polymeric solution on top of a hydrogel mold, phase separation starts immediately, mimicking the NIPS method in principle. Also, the hydrogel, as a water-based mold, can be easily structured with different geometries. Using the HFPS method, we resolved the limitations encountered by phase inversion micro-molding (PSμM) [46,151] and nanoimprint lithography (NIL) [53,117] techniques that suffered from patterning the non-active side of the membrane and damaging the membrane internal structure, respectively.

In this study, we used the HFPS method to prepare gravity-driven super-high flux polyamide-imide (PAI) microfiltration (MF) membranes. It is well-known that most of the polymers commonly used to synthesize MF and UF membranes (e.g., polyethersulfone and polysulfone) are inherently hydrophobic [152]. Hence, bulk and surface modifications are necessary to enhance their performance. In contrast, PAI is a hydrophilic and underwater superoleophobic polymer that provides high water permeability and antifouling properties [134]. Herein, we utilized the hydrophilic PAI with the advantages of HFPS to produce antifouling and high flux MF membranes. This unique combination can potentially eliminate the need for a series of hydrophilization methods, which may not be feasible for large scale production of membranes. PAI membranes with different porosities were prepared using HFPS and NIPS methods and evaluated in terms of morphological properties, wettability, and pure water permeability. Furthermore, the membranes were applied for the separation of n-hexadecane, diesel, and mineral oil in water emulsions under gravity.

4.2 Materials and Methods

4.2.1 Chemicals

Polyamide-imide (PAI, Torlon® 4000T-HV, Solvay, USA), polyvinylpyrrolidone (PVP, Sigma - Aldrich, average M_w = 10k), and N, N-dimethylacetamide (DMAc, Sigma-Aldrich) were all used to make polymer casting solutions. Agarose (Sigma-Aldrich) was used to prepare hydrogel solutions. N-hexadecane, mineral oil, diesel oil, and Tween 80 were purchased from Sigma Aldrich to prepare oil/water emulsions. Polymethylmethacrylate (PMMA, McMaster-Carr, USA) was employed to prepare master molds.

4.2.2 Preparation of solutions

PAI polymer solutions were prepared by mixing PAI, PVP, and DMAc with compositions shown in Table 4.1. The mixture was then stirred in a beaker at 50 $^{\circ}$C overnight until a homogenous solution was obtained. After that, the solution was placed to rest at room temperature overnight and then used to prepare HFPS patterned and unpatterned membranes (PM4, PM6, PM8, UPM4, UPM6, and UPM8) and NIPS conventional membranes (CM6 and CM8). It is worth mentioning that CM4 could not form on the polyester fabric support due to the low viscosity of 4 wt.% PAI solutions. Hydrogel solutions (50 g) were prepared by mixing agarose (5 wt.%) with distilled water (95 wt.%) and subsequent heating in a microwave up to the boiling point of water for 120 s. 500 mg/L oil in water emulsions were prepared by mixing 0.5 g of oil, 0.75 mg of Tween 80, as a surfactant, and 1000 mL of distilled water. To stabilize oil in water, the mixture was blended with a homogenizer (Homogenizer 150, Fisherbrand, Canada) for 4 min. Dynamic light scattering (DLS, ALV/CGS-3 Goniometer) technique was used to determine the size distribution of three different oils in water.

Table 4. 1. The polymer concentrations used to prepare HFPS and NIPS membranes

Membrane	PAI Conc. (wt.%)	PVP Conc. (wt.%)	DMAc Conc. (wt.%)
PM8	8	2	90
UPM8	8	2	90
CM8	8	2	90
PM6	6	2	92
UPM6	6	2	92
CM6	6	2	92
PM4	4	2	94
UPM4	4	2	94

4.2.3 Preparation of HFPS membranes

The hydrogel solution, while in the liquid state, was placed on a patterned acrylic mold with a controlled thickness of 1.6 mm and then left for solidifications (2-3 min), as shown in Figure 4.1a.

Then, the hydrogel mold was gently demolded from the acrylic mold and placed on a glass plate where its pattern side was faced up. Subsequently, the membrane polymer solution was cast using Gardco film applicator (Paul N. Gardner Company, Pompano Beach, FL) on top of the hydrogel mold with a thickness of 200 µm. After that, the cast film was left under the fume hood until the membrane is fully formed in 1-2 min (Figure 4.1. b –d). Finally, the assembly (the hydrogel mold and the membrane) was placed in a water bath, and the membrane was gently removed from the hydrogel mold and kept for later use.

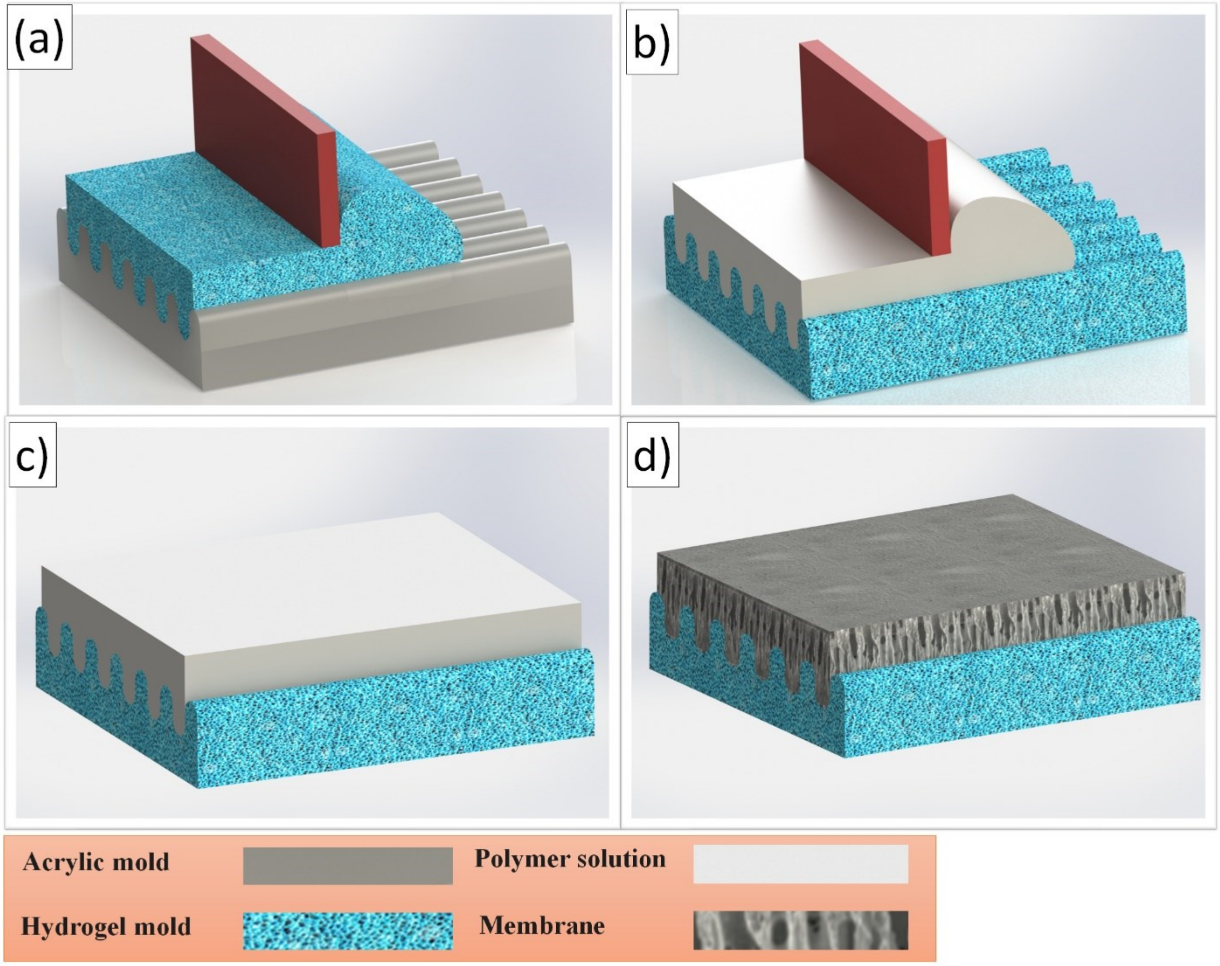

Figure 4. 1. A 3D schematic diagram of the preparation steps of HFPS membranes. (a) The hydrogel solution was cast on top of the patterned acrylic mold to form the hydrogel patterned

mold. (b) The hydrogel mold was placed on a glass plate, and a PAI polymer solution was cast on top with a controlled thickness of 200 µm. (c) The PAI polymer solution was left for 1-2 min under the fume hood until full formation. (d) The membrane was formed and ready to be peeled off the hydrogel mold.

4.2.4 Characterization

4.2.4.1 Membrane Morphology

The top surface cross-sectional structures of the obtained membranes were observed using field emission scanning electron microscopy (FEESEM, Zeiss Sigma). Membrane samples were first soaked in 3 wt.% glycerol/water solution and then dried at room temperature. This step was performed to prevent collapsing of the PAI pores during the drying step. After that, the membrane samples were broken in liquid nitrogen and mounted on an SEM stub. Prior to SEM imaging, the samples were coated with a gold layer (~2nm).

4.2.4.2 Mechanical Properties

The mechanical properties of PAI membranes were characterized using a tensile measurement device following a standard procedure from the literature [153]. Membrane samples with dimensions of 8 mm X 40 mm (thicknesses were taken from the SEM images of PM8, PM6, and PM4) were carefully cut and clamped between two 3D printed holders (see Figure 4.S1). The applied displacement and the corresponding forces were detected using a National Instrument motion controller (Model No. ESP301), data acquisition (DAQ) hub (NI USB-6289), and a load cell (Transducer Techniques, GSO-25) [154]. CM8 and CM6 were not tested because they have polyester fabric support, and thus the tensile strength of these membranes would be dominated by the fabric support.

4.2.4.3 Chemical Composition

Attenuated total reflectance-Fourier transform infrared (ATR-FTIR) was utilized to evaluate the chemical composition of the prepared membranes. The transmittance spectrums were recorded over the scanning range of 1000-4500 cm^{-1} with a resolution of 4 cm^{-1} at room temperature.

4.2.4.4 Porosity measurement

The porosity of the prepared membranes was determined by the gravimetric method [26,73]. First, 3 pieces from each membrane were randomly cut and immersed in water. Then, the external sides of the membrane pieces were dried using a tissue (Kimwipes) to make sure that no excess water exists on the surface, and the dried samples were weighed using a digital balance (Mettler Toledo). The membrane pieces were then placed in a digital oven and dried overnight at 60 ºC. The completely dried membrane samples were again weighed, and the porosity (ε) value for each membrane was calculated as follows:

$$\varepsilon = \left(\frac{(m_{wet} - m_{dry})/\rho_w}{\frac{m_{wet} - m_{dry}}{\rho_w} + \frac{m_{dry}}{\rho_p}} \right) \times 100 \tag{4.1}$$

where ρ_w is the density of water (g cm^{-3}), ρ_p are the density of PAI (g cm^{-3}), m_{dry} is the weight of dry membrane samples (g), and m_{wet} is the weight of wet membrane samples.

4.2.4.5 SEM image processing

The SEM images of the top surface of membranes (Figure 4.S2 – 4.S4 in the Supplementary Material) were utilized to extract the pore size distribution of the membrane surface through the following standard steps [155]:

(i) The darkest places in each image are considered opening longitudinal pores.

(ii) The multi-Otsu threshold algorithm was used to separate the pixels of each gray-scale image into different segments depending on the intensity of the gray levels within the image [156]. In this step, the pores are distinguished from the surrounding solid polymer by converting them into black and white colors, respectively.

(iii) The longitudinal pores are divided into colored segments using the watershed algorithm, which is a common method to separate overlapped porous geometries [157].

(iv) To find the pore size distribution, the area of each detected segment (pore) is measured and used to calculate the radius of an equivalent circle with the same area.

4.2.4.6 Wettability measurement

The apparent water contact angle of each membrane was measured using a contact angle analyzer instrument (Kruss GmbH, Hamburg, Germany). A small piece of each membrane was attached on a glass slide in which a 2 μL water droplet was gently placed on the active side of the membrane. The contact angle was then measured after the droplet reached an equilibrium stage. Five measurements were taken for each sample.

4.2.4.7 Underwater oil wettability

The underwater oil contact angle was measured using the same device using the captive bubble technique. Small pieces of membranes were attached to a plastic holder with active surface facing the downside and placed in an optically sensitive quartz cuvette filled with DI water. A J-shaped needle was lowered into the cuvette and fixed to place 6 μL oil droplet on the membrane surface. For each oil drop, a nascent membrane piece was used, and 5 measurements were taken for each sample.

4.2.5 Filtration tests

4.2.5.1 Pure water tests

Filtration experiments were conducted using a dead-end filtration cell (Millipore cell, Amicon® Stirred Cell 400mL) with an effective surface area of 41.8 cm^2 under no transmembrane pressure. Permeate was weighed using a digital balance (ME4002, Mettler Toledo, USA), where data was automatically recorded using a laptop with a time interval of 15 s. The pure water flux was calculated using:

$$J_w = \frac{Q}{A\Delta t} \tag{4.2}$$

where, J_w is the permeated water flux (L m^{-2} h^{-1}), Q is the amount of permeated water (L), Δt is the sampling time (h), and A is the surface area of the membrane (m^2). In this work, pure water refers to distilled water.

4.2.5.2 Oil/water emulsion tests

The filtration performance of the membranes was assessed using three types of oil/water emulsions based on the following protocol: (1) pure water filtration test (J_{w1}) was initially performed for 10 minutes, (2) oil/water emulsion filtration test (J_{wf}) was conducted for 10 minutes, (3) the membrane was washed with pure water for 2 minutes, (4) pure water filtration test (J_{w2}) was performed again for 10 minutes. This protocol was considered as one cycle, and the filtration of each oil/water emulsion was repeated for three consecutive cycles. The over all filtration experiments were repeated three times using a new synthesized membrane each time.

The percentage of flux decline (FD) and recovery ratio (FRR) for each cycle was calculated using Eqs. 3 and 4, respectively

$$FD = \left(1 - \frac{J_{wf}}{J_{w1}}\right) \times 100 \tag{4.3}$$

$$FRR = \left(\frac{J_{w2}}{J_{w1}}\right) \times 100 \tag{4.4}$$

In order to measure the oil/water emulsion rejection, the permeate and feed samples were tested using a UV-Vis spectrophotometer (Thermo Fisher Scientific GENESYS™ 10). The oil rejection was calculated as follows:

$$R = \left(1 - \frac{C_p}{C_f}\right) \times 100 \tag{4.5}$$

where the C_p and C_f are the oil concentrations in the permeate and the feed solutions, respectively.

4.3 Results and discussion

4.3.1 ATR-FTIR results

ATR-FTIR results of the fabricated membranes are shown in Figure 4.2. All membranes demonstrated a characteristic imide bond, including asymmetric C═O stretching at 1778 cm^{-1}, symmetric C═O stretching at 1720 cm^{-1}, and C—N stretching at 1378 cm^{-1} [158]. The PAI is also bearing amide functionals which its corresponding peaks appeared at 1670 cm^{-1} (C═O stretching) and 1500 cm^{-1} (C—N stretching) [134]. Two different ranges from the ATR-FTIR spectrum were highly focused on comparing the PVP content of the membranes. The prominent peak centering at 1661 cm^{-1} corresponds to C═O stretching vibration existing in the PVP structure. As can be seen, the un-patterned HFPS membranes exhibited the highest PVP content remaining within the PAI bulk after phase inversion. In contrast, most of the blended PVP polymers were obviously leached out from the outer layers of patterned HFPS membranes due to the higher surface area of the hydrogel mold which enhanced the diffusion rate of PVP macromolecules during the membrane formation. The similar intensity trends obtained from O—H stretching (wide peaks at 3280 cm^{-1}) can further confirm such observation.

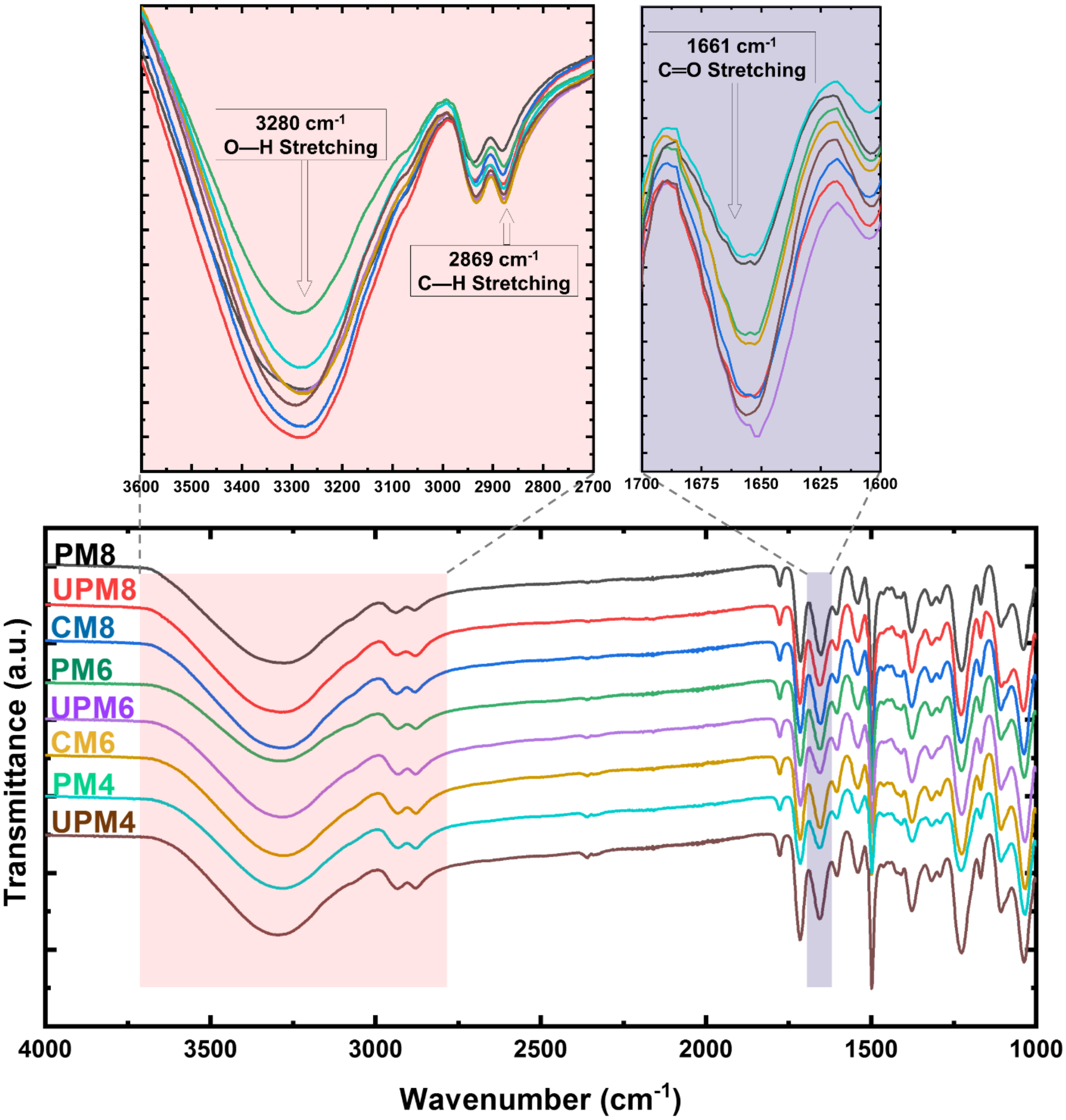

Figure 4. 2 ATR-FTIR spectra of 8 different fabricated membranes. As represented, all membranes possessed some identical characteristic peaks. The enlarged wavenumber ranges on top are representing the PVP content of each membrane.

4.3.2 SEM analysis

The cross-sectional FESEM images of patterned and un-patterned membranes prepared by the HFPS method with different polymer concentrations are shown in Figure 4.3. The cross-sectional FESEM images of NIPS membranes are also represented in Figure 4.S5. All membranes showed finger-like asymmetric structures with a dense skin layer at the top, which is a typical feature of HFPS and NIPS membranes [26]. Although the thickness of the PAI polymer cast solution was the same for all membranes, the overall thickness of HFPS membranes was higher than the NIPS one. The thicknesses of HFPS membranes with 8, 6, and 4 wt.% PAI concentrations were 200 µm, 190 µm, and 180 µm, respectively, while it was 60 µm in the case of NIPS membranes. In the NIPS method, a PAI polymer solution was cast on a polyester fabric support, then immersed in a distilled water bath to complete the membrane solidification. However, due to the low viscosity of the polymer solution (≤ 8 wt.%), a significant portion of it has likely penetrated within the fabric support, resulting in a formation of thinner membranes. Unlike the NIPS method, the polymer solution in HFPS is cast on top of the hydrogel mold and stayed there until the formation of the membrane is completed to form a single-layer porous membrane. The reason behind casting the PAI solution on fabric support, in the case of the NIPS method, was difficulty in detachment of solidified PAI film from the underlying glass surface.

The morphological properties of membranes, such as the overall thickness, the thickness of the skin layer, and the porosity, were highly dependent on the PAI concentration. The change in these properties can be explained by the effect of the thermodynamic enhancement and the kinetic hindrance on the phase separation process. The thermodynamics aspect describes the stability of the polymer solution starting from one stable phase (homogenous state of polymer and solvent) that becomes unstable with two phases, namely, polymer-rich (forms the membrane matrix) and polymer lean (nonsolvent rich that forms the membrane pores) in the presence of nonsolvent. The kinetic aspect describes the solvent and nonsolvent demixing rate [159]. The formation of HFPS and NIPS membranes occurs in two stages [25,82]: (1) Rapid exchange between the solvent and nonsolvent at the film surface to the point that polymer concentration is high enough to form a dense skin layer, which acts as a barrier against further penetration of nonsolvent into and solvent out of the polymer film; (2) formation of the fingers/microvoids happening at the points where the skin layer ruptures due to the syneresis and shrinkage stresses. By decreasing the PAI concentration in the polymer solution, the in-diffusion of the nonsolvent and out-diffusion of solvent are accelerated due to the decreased viscosity of the casting solution. This instantaneous demixing, along with the quick rupture of the skin layer, led to the formation of membranes with lower overall thickness and skin layer thickness [25]. The skin layer thicknesses of 8 wt.% PAI membrane were reduced by 34% and 65% for 6 wt.% and 4 wt.% PAI membranes, respectively. The overall thickness of 8 wt.% membranes was also reduced by 5% and 15% for 6 wt.% and 4 wt.% membranes, respectively. At lower polymer concentrations (<8 wt.%), the skin layer thickness of both HFPS and NIPS membranes were almost similar. However, at higher polymer concentrations, the skin layer thickness was observed to be higher for HFPS membranes due to the limited amount of nonsolvent available for the phase separation that slowed down the demixing rate [26].

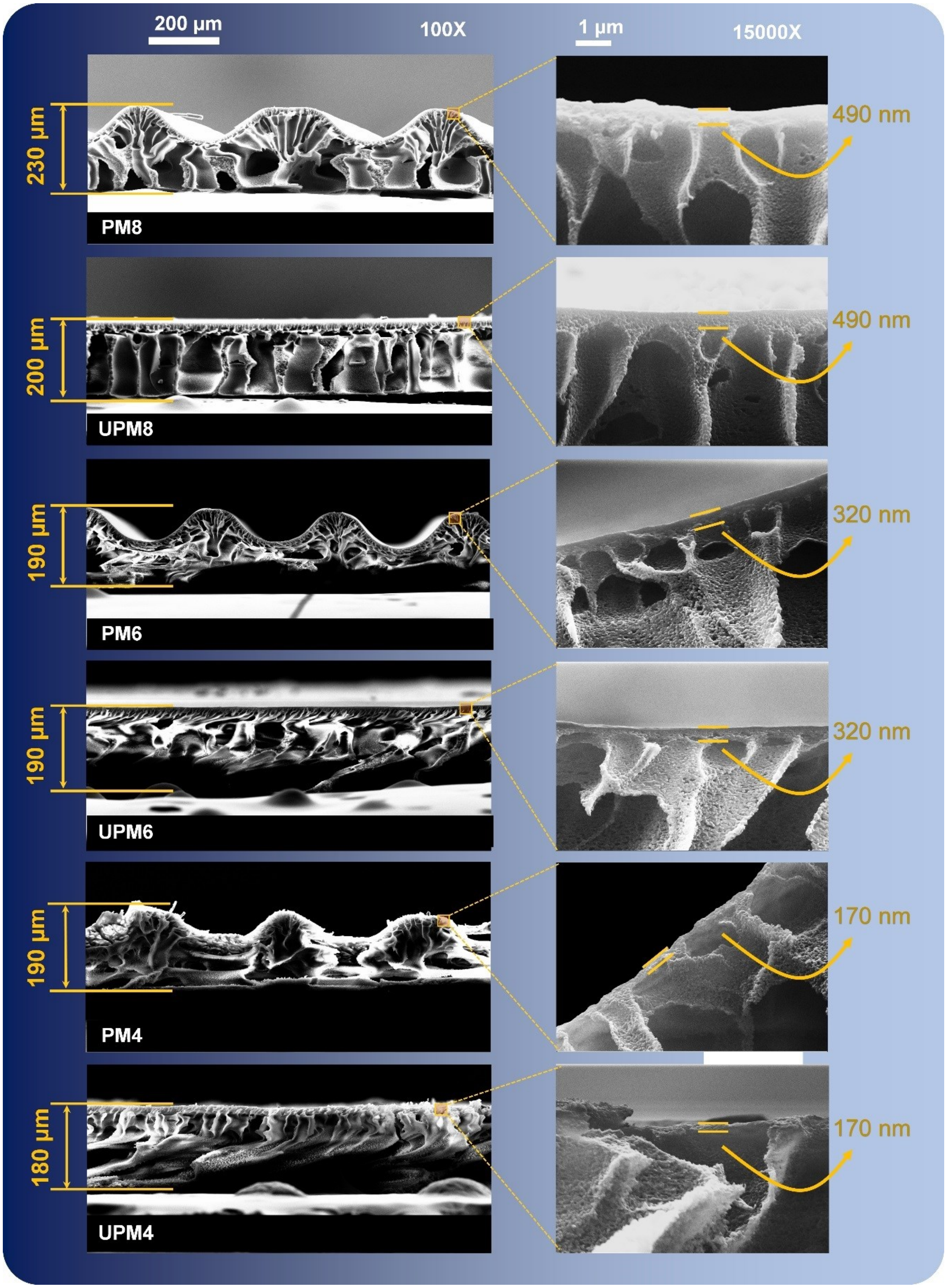

Figure 4. 3. Cross-sectional SEM images of HFPS membranes with two different magnifications.

The overall porosity values of the HFPS and NIPS were also increased as the PAI concentration decreased. In the case of HFPS membranes, the overall porosities of 8 wt.%, 6 wt.%, and 4 wt.% membranes were 80%, 87%, and 90%, respectively. The increase in the overall porosity can be attributed to the increase in the PVP/PAI ratio of the polymer solution. Since low molecular weight PVP (10 kDa) was used in the present work, the accelerated leaching of this additive into the nonsolvent, particularly for less viscous casting solutions, has led to a higher porosity [160]. The porosity values of 8 wt.% and 6 wt.% NIPS membranes were 60% and 63%, respectively. A possible explanation is the entrapment of PAI and PVP polymers within the fabric support, which might have reduced the solvent-nonsolvent demixing rate and release of PVP macromolecules.

Figure 4.4 shows the surface FESEM images of HFPS membranes at different magnifications. Top surface FESEM images of NIPS membranes are also presented in Figure 4.S6. The top surfaces of these membranes possess many longitudinal pores that are typical of NIPS membranes [19,161]. The reason behind the existence of such shapes is the lateral and longitudinal rupture of the skin layer during membrane formation. The surface average pore size of all HFPS membranes was ~30 nm for all concentrations. Such similar pore size distribution can be attributed to the upside-down formation mechanism of the HFPS method in which PAI had to precipitate directly on the hydrogel mold. According to the results listed in Table 4.2, the surface pore size of patterned membranes was larger than that of unpatterned and NIPS membranes. As proved by ATR-FTIR analyses, the embedded PVP macromolecules were mostly leached out from the outer surface of the patterned HFPS membranes during phase inversion step. The remaining open voids and spaces after PVP dissolution in water can increase the surface average pore diameter as visualized by top FESEM pictures.

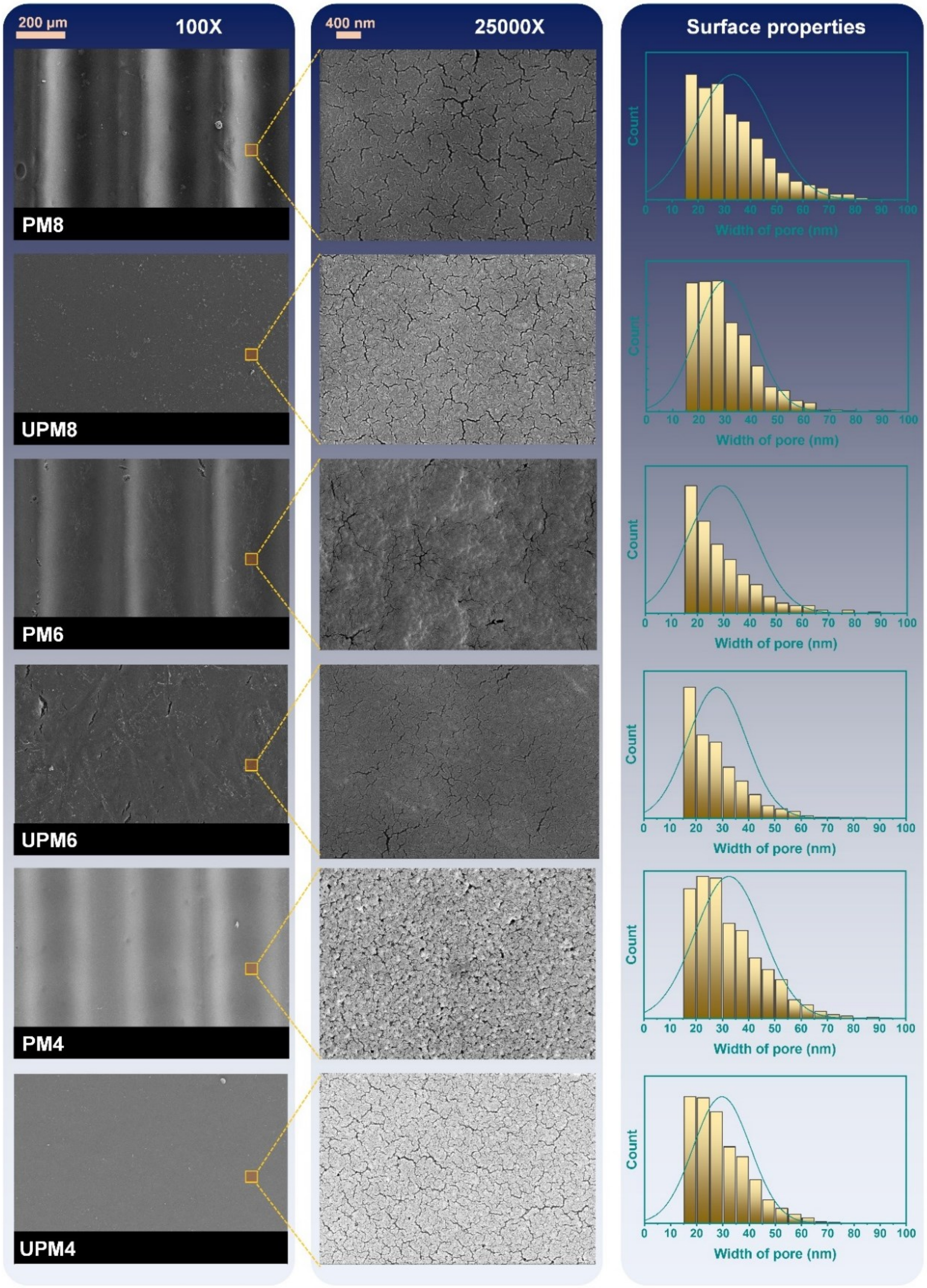

Figure 4. 4 Top FESEM images from the surfaces of HFPS membranes with corresponding pore size distribution curves.

Table 4. 2: The morphological characteristics of the fabricated membranes

Membrane	Overall thickness (μm)	The thickness of the top skin layer (nm)	The surface average pore diameter (nm)	Surface pore density (%)	Bulk porosity (%)
PM8	230	490	32.4	9	80
UPM8	200	490	28.4	8	80
CM8	60	480	25.8	9	60
PM6	190	320	29.2	7	87
UPM6	190	320	28.0	9	87
CM6	60	310	28.0	6	63
PM4	170	170	32.0	16	90
UPM4	170	170	29.6	10	90

4.3.3 Mechanical stability

The mechanical properties of the fabricated patterned membranes were evaluated through stress-strain tests, and the obtained data are plotted as Figure 4.S7. The tensile strength of PM8, PM6, and PM4 membranes were 0.086, 0.064, and 0.051 MPa, respectively. As expected, reducing the PAI concentration from 8 wt.% to 6 wt.% and 4 wt.% resulted in a reduction in the tensile strength by a value of 22% and 50%, respectively. Since the fabricated membranes are used in gravity-driven filtration experiments, the small sacrifice in the mechanical properties did not affect the durability of the membranes through the whole filtration process, as no visible damage was seen after 18 filtration runs of each membrane.

4.3.4 Wettability

The wettability of the fabricated membranes was evaluated through the measurement of water contact angle (WCA) and underwater oil contact angle (OCA), and the results are presented in Table 4.3. In general, patterned membranes demonstrated lower apparent WCA values as compared to unpatterned and NIPS membranes due to the existence of patterns, as reported in our previous work [26]. The WCA values of 8 wt%, 6 wt%, and 4 wt% unpatterned membranes were 36°, 35°, and 28°, respectively (Figure 4.5a). The slight decrease in the WCA of the 4wt% membranes can be attributed to the increase in the PVP macromolecules at the membrane surface, as confirmed by the ATR-FTIR results. Another possible reason could be the increase in the surface pore density (Table 4.2), which might have increased the water droplet penetration into the membrane [134]. Both HFPS unpatterned and NIPS membranes showed similar WCA values for all PAI concentrations, which was expected as both have similar surface properties.

Table 4. 3: Water contact angle (WCA) and underwater oil contact angle (OCA) of the fabricated membranes.

Membrane	WCA (Apparent, °)	OCA (n-hexadecane, °)	OCA (diesel oil, °)	OCA (mineral oil, °)	Pure water flux (LMH)
PM8	21±2	No attachment	No attachment	No attachment	244
UPM8	36 ±3	146 ± 3	No attachment	152 ± 3	172
CM8	36 ±2	146 ± 3	No attachment	152 ± 3	63
PM6	17±3	No attachment	No attachment	No attachment	402
UPM6	35 ±2	148 ± 3	No attachment	156 ± 3	346

CM6	35 ±3	148 ± 3	No attachment	156 ± 3	157
PM4	15±1	No attachment	No attachment	No attachment	440
UPM4	28 ±2	153 ± 3	No attachment	158 ± 3	356

The underwater OCA analysis is generally used to evaluate the propensity of the membrane surface towards oil fouling. The higher the OCA, the lower the oleophilic interaction between the membrane surface and the oil droplet, which is preferable to reduce oil fouling. This effect is mainly observed in the filtration performance of membranes, where the higher repellency for oil results in a lower flux decline and higher flux recovery ratio (more information regarding the contact angle analyzer instrument is provided in Figure 4.S8). Underwater oil contact angle measurements were conducted using n-hexadecane, diesel, and mineral oils. The underwater OCA values of n-hexadecane/mineral oils for 8wt%, 6wt%, and 4wt% unpatterned membranes (UPM8, UPM6, and UPM4) were 146°/152°, 148°/156°, and 153°/158°, respectively, demonstrating the superoleophobic nature of PAI membranes (Figure 4.5a). The observed superoleophobicity can be attributed to the formation of a hydration layer on the surface of PAI membranes, preventing the direct contact of the solid part of the membrane with oil. Patterned membranes (PM8, PM6, and PM4) showed complete repellency for all types of oils. Since the HFPS method only changes the physical structure of the membrane without altering its surface chemistry, the complete repellency for oils is due to the existence of patterns. The relation between wettability and surface roughness was defined by Wenzel, who stated that an increase in the surface roughness would magnify the wettability caused by the surface chemistry. This means that a surface-patterned hydrophilic membrane provides higher wettability than an unpatterned one made from the same material. This aligns with our CA and OCA results, in which patterned membranes showed lower CA values and higher OCA values (180°) as compared to unpatterned ones. [162,163].

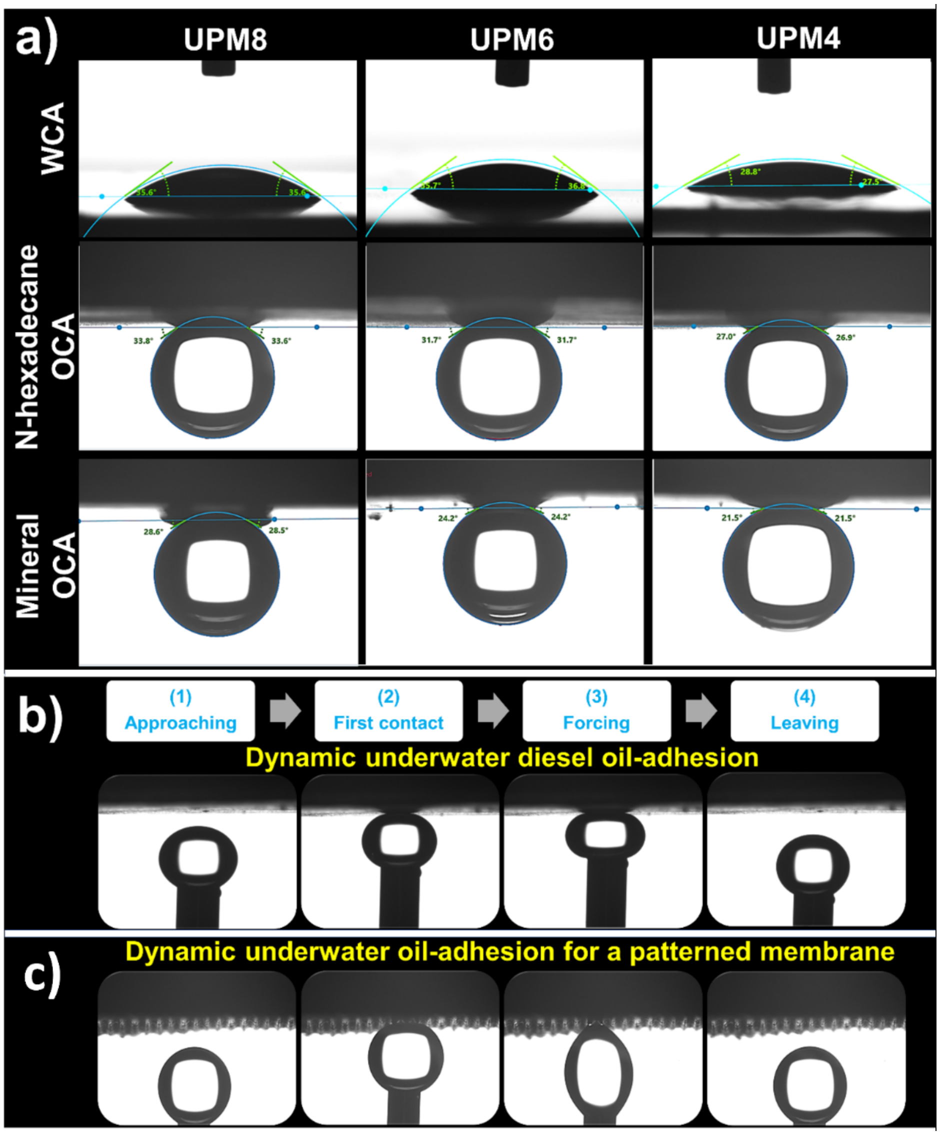

Figure 4. 5 a) The static water contact angle and underwater oil contact angles for HFPS unpatterned membranes (The water droplet size is 3μL, and the oil droplet size is 6μL). b) Dynamic underwater adhesion of diesel oil obtained for UPM8 (all membranes in this study showed no adhesion for diesel oil on their surfaces). c) Dynamic underwater adhesion of diesel oil for PM8 (PM8, PM6, and PM4 showed similar behavior for all types of oils).

Interestingly, diesel oil did not attach to the surface for all membranes. To examine the diesel oil repellency of PAI membranes, a dynamic underwater diesel oil adhesion test was performed (Figure 4.5b). First, 6 μL of diesel oil droplet was brought into contact with the membrane and then was squeezed onto the membrane surface to allow for sufficient oil/membrane interaction. After that, the needle holding the oil droplet was retrieved back with the oil droplet sticking into it, revealing the weak interaction between diesel oil and both HFPS patterned and unpatterned membranes' surface.

4.3.5 Membrane filtration performance

4.3.5.1 Pure water flux

The pure water flux results of all membranes are presented in Table 4.3. The pure water flux for PM8 was about 40% and 300% higher than UPM8 and CM8 membranes, respectively. Improvement of initial water flux in HFPS patterned membranes can be attributed to a 34% increase in the surface area compared with the unpatterned ones. The free-standing nature of HFPS membranes reduced the overall resistance against water permeation and increased the overall porosity, thereby a significant higher pure water flux obtained in the case of HFPS membranes compared with NIPS membranes. In NIPS membranes, the penetrated polymer solution in the fabric support clogged its open channels. As the polymer concentration reduced from 8 to 6 wt.%, the pure water flux values increased by 60% for both PM6 and UPM6 and 150% for CM6 membrane. Such flux enhancement can be attributed to the reduction in the skin layer thicknesses and the increase in the bulk porosities. A similar flux increment trend was observed by decreasing the polymer concentration from 6 wt.% to 4 wt.%. PM4 and CM8 provided the highest and lowest water fluxes of 430 LMH and 60 LMH, respectively. The super-high flux of PM4 is ascribed to its high bulk and surface porosities (90% and 16%), very thin skin layer (170 nm), and high wettability, as proved by WCA results (15±1°).

4.3.5.2 Antifouling performance

The antifouling performance of HFPS and NIPS membranes was examined by filtration of oil in water emulsions using a dead-end filtration setup under gravity. A consistent filtration protocol was applied to investigate the permeation and antifouling properties of each membrane. Figure 4.6 shows the variation of permeate flux with time during filtration of n-hexadecane, diesel oil, and mineral oil-in-water emulsions in three consecutive cyclic tests. To assess the performance of membranes under harsh fouling conditions, each membrane was continuously utilized for all oil filtration tests. The FD and FRR parameters are calculated using Equations 3 and 4, and the results are presented in Figure 4.7. As shown in Figure 4.6a, by replacing the pure water with n-hexadecane emulsion, the water flux declined slightly for all membranes. The FD and FRR values after three n-hexadecane oil emulsion cyclic tests were in the range of 4-18% and 90-100%, respectively (Figure 4.7). Such small FD and high FRR values are attributed to the highly hydrophilic and underwater superoleophobic nature of PAI membranes, as confirmed by WCA and underwater OCA (also see supporting videos) [134]. After the oil-in-water emulsion touches the membrane surface, the water instantly spreads on the surface of the membrane and penetrates the membrane pores. Due to the strong interactions between water molecules and the functional groups of PAI, a robust hydration layer forms that prevents direct contact between oil and the membrane surface [164]. In the case of diesel oil emulsion filtration (Figure 4.6b), the FD and FRR values were in the range of 3-15% and 95-100% (Figure 4.7). The high FRR values can be explained by the OCA results, which showed no attachment of diesel oil on the membrane surface.

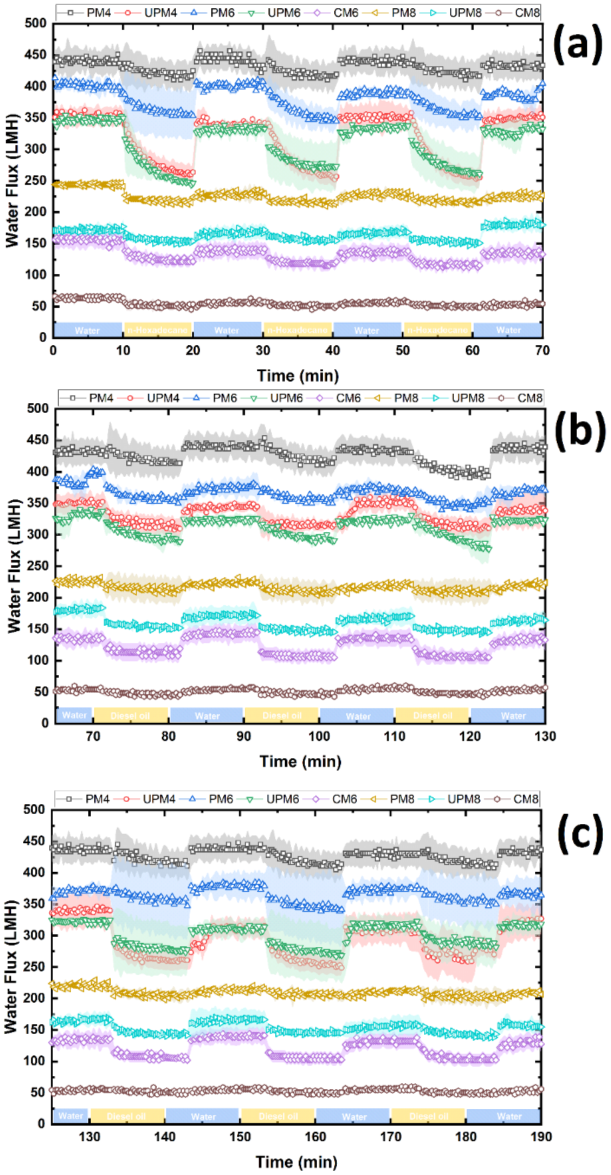

Figure 4. 6. Permeation flux vs. time for different fabricated membranes during the separation of (a) n-hexadecane in water emulsion, (b) diesel oil in water emulsion, and (c) mineral oil in water emulsion. The initial oil concentration was 500 mg/L, and the emulsions were prepared by adding 0.75 mg of Tween 80 as the surfactant. After each oil emulsion filtration test, the membrane was washed with distilled water for two minutes. The filtration experiments were repeated three times using a new synthesized membrane each time. The shaded areas on each data point represent the standard deviation of the mean of the three filtration results.

To demonstrate the robustness of the prepared membranes in long-term cyclic tests, a heavy mineral oil emulsion, which is a mixture of heavier alkanes, was chosen as the third oil. As shown in Figures 4.6c and 4.7, the behavior of membranes was found to be similar to the n-hexadecane in terms of FD (3-20%) and FRR (95-100%). The oil-in-water emulsion filtration results demonstrated the superior antifouling and high recoverability of PAI membranes with a simple water flushing. The repeatability of the synthesized membranes was ensured by synthesizing three new membranes of each polymer concentration. Each one of these membranes was used for the filtration experiments, as described in the experimental section.

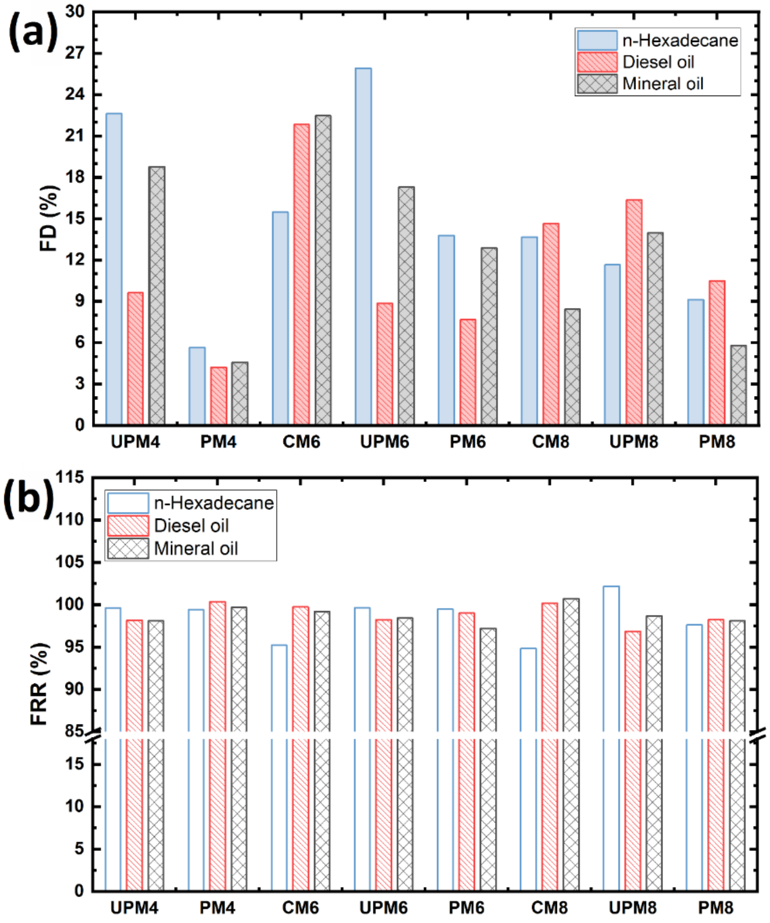

Figure 4. 7. (a) Flux decline (FD) and (b) flux recovery ratio (FRR) for all prepared membranes after filtration of n-hexadecane, diesel oil, and mineral oil in water emulsions.

We have noticed that for n-hexadecane and mineral oil-water emulsion separation tests, when the water flux is higher than 250 LMH, the flux decline becomes more significant. A possible explanation is the enhanced concentration polarization effect at higher permeation fluxes. As the water passage increases, the concentration of oil at the vicinity of the membrane surface increases, leading to more interaction between oil and the membrane surface [165]. This trend was observed for all membranes that provided water fluxes higher than 250 (PM6, UPM6, and UPM4), except for PM4, with the highest water flux. This can be attributed to the highest surface porosity of PM4 among all synthesized membranes that might have reduced the available contact areas for oil droplets to attach [166]. Overall, the combination of excellent characteristics of the fabricated membranes, including super-wetting property and high bulk and surface porosities, has led to high permselectivity without applying transmembrane pressure.

Figure 4.8 shows the optical pictures of feed and permeate solutions after treatment by the PM4 membrane. All membranes in this study showed 99.9% oil rejection for all oil-in-water emulsions. The high rejection values were attributed to the difference between the surface pore size of the synthesized membranes and the oil droplets diameter. As can be seen in Figure 4.S9, n-hexadecane showed a unimodal distribution with one clear peak at 570 nm mean diameter. Diesel and mineral oils, however, exhibited two distinct peaks, with the first prominent peaks positioning at a mean value of 420 nm (weight of peak = 71%) and 530 nm (weight of peak = 52%), respectively. The mean size of the second DLS peak was 8.8 μm for diesel oil and 6.1 μm for mineral oil. The prepared oil/water emulsions were adequately stable, and no phase separation was observed after 24 h resting time. The surface pore size of all fabricated membranes, measured by the SEM image analysis, were in the range of 25.8 - 32.4 nm, which are much smaller than the oil droplet diameters (420 nm – 8.8 μm).

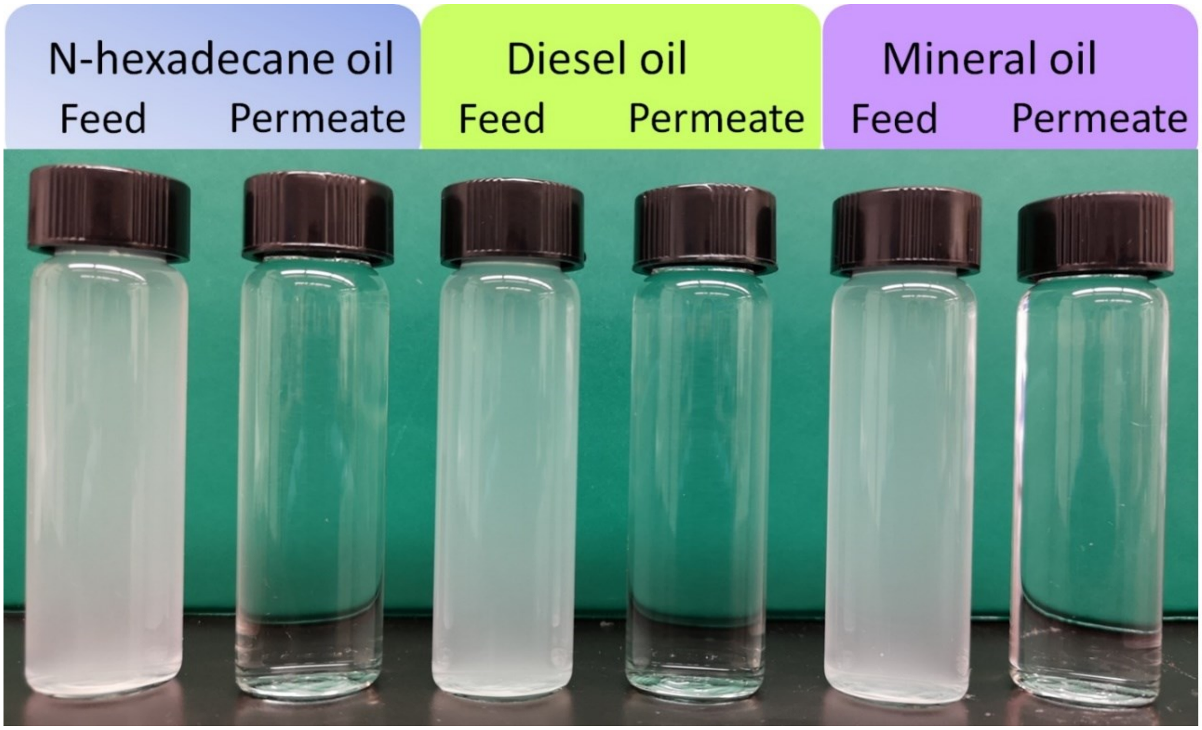

Figure 4. 8. Optical pictures of feed and permeate solutions after filtration by PM4 membrane.

Table 4.4 provides a comparison between our best membrane, PM4, with other recent state-of-the-art membranes for the separation of oil-in-water emulsions. As can be noticed, the PM4 membrane achieved superior filtration performance in terms of low FD, high permselectivity, and FRR as compared to the different surface- and bulk-modified membranes at TMP ranged between 1-3 bar. Moreover, compared with the recently developed gravity-assisted membranes, PM4 showed better filtration performance. The smart integration of the hydrophilic nature of PAI with the advantages of the HFPS method has led to the fabrication of highly porous free-standing membranes with ultra-high flux under gravity.

Table 4. 4. Comparison of our best membrane (PM4) with other membranes for the treatment of oily wastewater

Membrane	**Type of modification**	**Type of oils**	**Oil droplet size (nm)**	**Concentration of oil (mg/L)**	**Trans-membrane pressure (Bar)**	**Pure water flux (LMH)**	**Oil/water emulsion flux (LMH)**	**FRR (%)**	**Ref.**
PSf-bentonite	Bulk	Crude oil	500-938	---	1	300	150	----	[167]
PSf-HAO	Bulk	Crude oil	387	1000	1	1194	191	67	[168]
PVDF-TBC	Bulk	Engine oil	380-720	1000	2	360	60.5	76-88	[169]
PES-P(PEG-grad-TFOA)	Bulk	vacuum pump oil (GS-1)	----	1000	1	140	119	100	[170]
PES-Pluronic F127	Bulk	Soybean oil	2,100	1000	1	~128	85	93	[171]
PSf-Pro-PEG	Grafting	Soybean oil	1000	1000	1	139	130	95	[172]
PSf-Pro-PEG	Grafting	oilfield	1,2000		1	139	119	95	[172]
PVDF-PVP	Grafting	260# solvent oil	90-105	300	3	552	513	93	[173]
PES-TiO_2	Surface coating	commercial gas oil	----	3000	1.5	~27	~16	----	[174]
PES-SiO2-g-(PDMAEMA-co-PDMAPS)	Bulk	Engine oil	1000	----	1	~172	~80	84.3	[175]
PVDF-ZrO_2-MWCNTs	Bulk	diesel oil	4,000	1000-3000	1.5	325	150	80.9	[176]
PAN-F127-$CaCO_3$	Bulk	Motor oil	5,000	1	2	343	161	98	[177]
PSf-SZY	Bulk	wastewater	----	80	2	125	110	---	[178]
PAN-100kDa	Commercial membrane	grade gas–oil	750	1000	3	350	96	95	[179]
PES	Surface modifications	grade gas–oil	~700	3000	1.5	~143	70	---	[180]

ESSM@PDA@MOF	Surface modifications	Hexadecane	---	1000	Gravity	---	350	---	[181]
TiO2/sulfonated graphene oxide/Ag nanoparticle	Surface modifications	Gasoline	530-5,560	---	Gravity	---	53	100	[143]
Hygro-responsive	Surface modifications	Hexadecane	10,000-20,000		Gravity	43,200	90	---	[142]
PP-PDA/PEI	Surface modifications	n-hexane	~8,000	10,000	Gravity	147.7	120	100	[182]
PM4	**Physical surface modifications**	**Diesel oil**	**420**	**500**	**Gravity**	**440**	**420**	**100**	**This work**

4.4 Conclusion

In this work, we fabricated highly porous PAI microfiltration membranes using HFPS and NIPS methods for the separation of oil-in-water emulsions under gravity. HFPS patterned membranes showed ~300% increase in the pure water flux compared with the NIPS ones. This was attributed to the increase in the surface area (in the case of HFPS-patterned membranes), the free-standing nature of HFPS membranes, as well as the elimination of the unwanted secondary skin layer at the non-active side. Moreover, patterned membrane with 4wt.% PAI (PM4) provided the highest water flux of 440. Cyclic tests of 3 different oils, namely, n-hexadecane, diesel, and mineral oils, were performed to evaluate the separation and antifouling performance of the prepared membranes. The FRR and FD results of PM4 after 18 filtration experiments were >98% and <6%, respectively.

Chapter 5

Micro-patterned Thin Film Composite Poly(piperazine-amide) Nanofiltration membranes for Wastewater Treatment

5.1 Introduction

Freshwater and energy scarcities are two of the greatest challenges human beings will face in the next few decades.[152,183] The growing demand for freshwater due to population growth, climate change, and industrial activities has created an essential need for additional water resources [184,185]. Oil sands and textile industries, for example, consume a massive amount of freshwater during their processes and consequently generates large quantities of wastewater that can endanger the environment and public health if not treated adequately or disposed of improperly [186,187]. The sustainable growth of these industries relies greatly on energy-efficient wastewater treatment methods that purify water for better reusability [188].

The recent advancement in membrane separation processes made them reliable and effective methods for wastewater treatment [136-138]. Among these processes, nanofiltration (NF) with thin-film composite (TFC) membranes has attracted significant attention owing to its high water permeability and high removal rate of organic molecules (200-1000 Da) and multivalent ions [189,190]. A TFC membrane consists of a dense selective layer, mainly responsible for the selective property, coated on a microporous substrate. The most common method to synthesize this dense layer, typically made of polyamide, is interfacial polymerization (IP) reaction in which two highly reactive monomers, such as amine and acid chloride, react at the interface of two immiscible solutions [32,191,192]. The location of the interface is controlled to happen at the top surface of a porous membrane which leads to the fabrication the TFC membrane. Since the invention of TFC membranes, one of the hoped-for goals of researchers has always been enhancing both permeation flux (how fast water transport through a membrane) and rejection (the ability of a membrane to separate solutes) using cost-efficient and scalable methods [193,194]. Significant efforts have been made to enhance TFC membrane performance, including optimizing the parameters of the IP reaction [195], coating the membrane surface with hydrophilic layers [196-201], applying post-treatment steps using organic solvents[202,203], and incorporating nanoparticles within the polyamide layer [204-206]. Most of the proposed methods either added extra complexity steps that reduced the affordability and scalability of such membranes or lowered the permeation flux making them less applicable for industrial applications [150,207]. In addition, some of these modification methods used expensive nanoparticles or environmentally unfriendly chemicals [33].

Surface patterning of membranes was proposed as an eco-friendly method that increases the surface area to achieve high water permeation flux [208]. Currently, there are three techniques to make micro and nanopatterned porous membranes: (i) phase separation micromolding (PSμM) [46,48,66,209]; nanoimprint lithography (NIL) [112]; and (iii) our recently developed hydrogel-facilitated phase separation (HFPS) method [26,210]. HFPS method was developed to overcome the challenges associated with the other previous methods, such as forming an undesired dense skin layer at the unpatterned side of PSμM membranes and the damaged membrane internal structures resulting in the NIL method. In addition, HFPS provides extra flexibility in terms of materials selection and allows the fabrication of many different patterns on the membrane surface with a wide range of average pore sizes. Few studies in the literature utilized support membranes by the first two methods to make surface-patterned reverse osmosis (RO) membranes. For instance, Maruf et al. used NIL method to form nanopatterned PES membranes and then coated these membranes with a polyamide layer using IP reaction between m-phenylenediamine (MPD) and trimesoyl chloride (TMC) monomers. In another study, Elsherbiny formed the PA layer on PSμM patterned supports using the same monomers. The prepared patterned TFC RO membranes from

NIL and PSμM showed water permeability/NaCl rejection of 1 (LMH/bar) /90% and 1.4 – 1.6 (LMH/bar)/97-99%, respectively [211-214].

In this study, for the first time, we used HFPS substrates to synthesize TFC micro-patterned NF membranes by IP reaction. The IP reaction was performed using piperazine (PIP) and trimesoyl chloride (TMC) monomers dispersed in distilled water and n-hexane, respectively. Previous studies have proven that this combination of monomers can provide polyamide coatings with low surface roughness, high hydrophilicity, and more negative surface charge [215,216]. Therefore, the combination of this type of polyamide layer with the advantages of HFPS membranes can conceivably achieve high filtration performance without the need for costly and time-consuming modification methods. The prepared membranes were tested for the removal of monovalent and divalent ions, dye molecules, as well as the filtration of boiler feed water (BFW) taken from a Canadian oil sand wastewater treatment plant. The fabricated membranes were characterized in terms of morphological properties, surface chemistry, surface roughness, wettability, and permeation properties (water flux and solute rejection). Finally, the filtration performance of the fabricated HFPS-TFC membranes in this study was compared with the state-of-the-art commercial membranes and recent works in the literature.

5.2 Experimental Methodology

5.2.1 Chemicals

Polyethersulfone (PES, BASF, Ultrason E6020P, Mw= 58 kDa), N, N-dimethylacetamide (DMAc, Sigma-Aldrich), and polyethylene glycol (PEG, Sigma-Aldrich, Mw= 6kDa) were utilized to prepare polymer casting solutions. Agarose polymer (Sigma-Aldrich, CAS number: 9012-36-6) was utilized to make hydrogel solutions. Piperazine (PIP, Sigma-Aldrich), trimesoyl chloride (TMC, Sigma-Aldrich), and N-hexane (Fisher Scientific) were used to prepare the TFC membranes. A polymethylmethacrylate (PMMA, McMaster-Carr, USA) sheet was laser cut to prepare the master mold. The separation performance of the fabricated TFC membranes for salt and dye removal was evaluated using sodium chloride (NaCl), magnesium sulfate ($MgSO_4$), sodium sulfate (Na_2SO_4), methyl orange (Sigma-Aldrich, Mw=327.34 Da), and reactive black 5 (RB5, Sigma-Aldrich, MW=991.8 Da). Salts solutions were prepared by dissolving 2g of $MgSO_4$, Na_2SO_4, or NaCl in 1 L of distilled water. Dye solutions were prepared by dissolving 0.2 g of reactive black 5 or methyl orange in 1 L of distilled water. BFW was provided from steam-assisted gravity drainage (SAGD) water treatment plant located in the Athabasca oil sands region of Alberta, Canada. Table 1 presents the characteristics of oxidized SAGD BFW. These values were obtained by inductively coupled plasma-optical emission spectroscopy (ICP-OES) and total organic carbon (TOC) analyzer.

Table 5. 1. The characteristics of SAGD BFW at room temperature (25 °C).

Parameter	Unit	Value
pH	-	8.5
Conductivity	µS	~1,700
TOC	mg/L	96.2
TDS	mg/L	~1,000
Sodium	mg/L	292
Iron	mg/L	149
Potassium	mg/L	14.7

Sulfur	mg/L	76.2
Calcium, Copper, Magnesium, Manganese, and Phosphorus	mg/L	<1

5.2.2 Preparation of HFPS membranes as a support layer

PES polymer solution (40 g) was prepared by dissolving 10 wt.% PES and 2wt.% PEG in DMAc solvent. The polymer mixture was stirred at 300 rpm and 40 °C overnight to ensure the preparation of a fully dissolved and homogenous solution. The polymer solution was then placed at rest for 24 hours before casting on the hydrogel mold.

To fabricate the hydrogel mold, 50 g hydrogel solution was first prepared by dissolving 5wt.% agarose in 95 wt.% distilled water, followed by heating the solution in a microwave for 120 seconds. The hydrogel solution was then cast with a controlled thickness of 1.6 mm on the top of the patterned side of the acrylic master mold and left for 2-3 minutes to solidify (Figure 1a). After that, the hydrogel mold was peeled off and placed on a glass plate for polymer solution casting.

The PES polymer solution was cast on top of the hydrogel mold using a film applicator with a thickness of 100 μm and left under the fume hood for 1-2 minutes until the membrane was formed. (Figure 1b & c) After that, the hydrogel mold and the membrane on it were placed in a water bath. The membrane was demolded from the hydrogel mold and stored in another water bath for later use. Two types of membranes were prepared using the HFPS method, patterned and unpatterned, denoted here as base-P and base-U, respectively.

5.2.3 Preparation of thin film composite membranes

The thin-film polyamide layer was formed on top of HFPS membranes using interfacial polymerization (IP) reaction between PIP and TMC monomers dissolved in two immiscible solvents (Figure 1). The monomer solutions were prepared by dissolving piperazine (PIP) and trimesoyl chloride (TMC) monomers in distilled water and n-hexane, respectively. The HFPS membrane was first dried at room temperature overnight and then fixed between two acrylic frames. Next, piperazine aqueous solution was poured on top of the membrane and left for 11 minutes to allow sufficient impregnation (Figure 1d). The membrane was then removed from the acrylic frames and taped on an inclined glass plate. After that, an air knife was used to remove the excess of the aqueous solution from the top surface of the membrane (Figure 1e). Then the membrane was again placed between a set of acrylic frames, and the TMC organic solution was poured on the membrane surface and kept for 40 seconds to allow the polymerization reaction to complete (Figure 1f). Finally, the polyamide-coated membrane was cured in an oven at 80 $^{\circ}$C for 4 minutes and then washed thoroughly with distilled water for 5 minutes to promote the hydrolysis of the unreacted acid chloride groups in the polyamide layer (Figure 1g). Table 2 shows the concentrations of PIP and TMC that were used in this study. For instance, TFC-P n and TFC- U n represent thin-film composite patterned and unpatterned membranes in which n indicates the concentration of PIP.

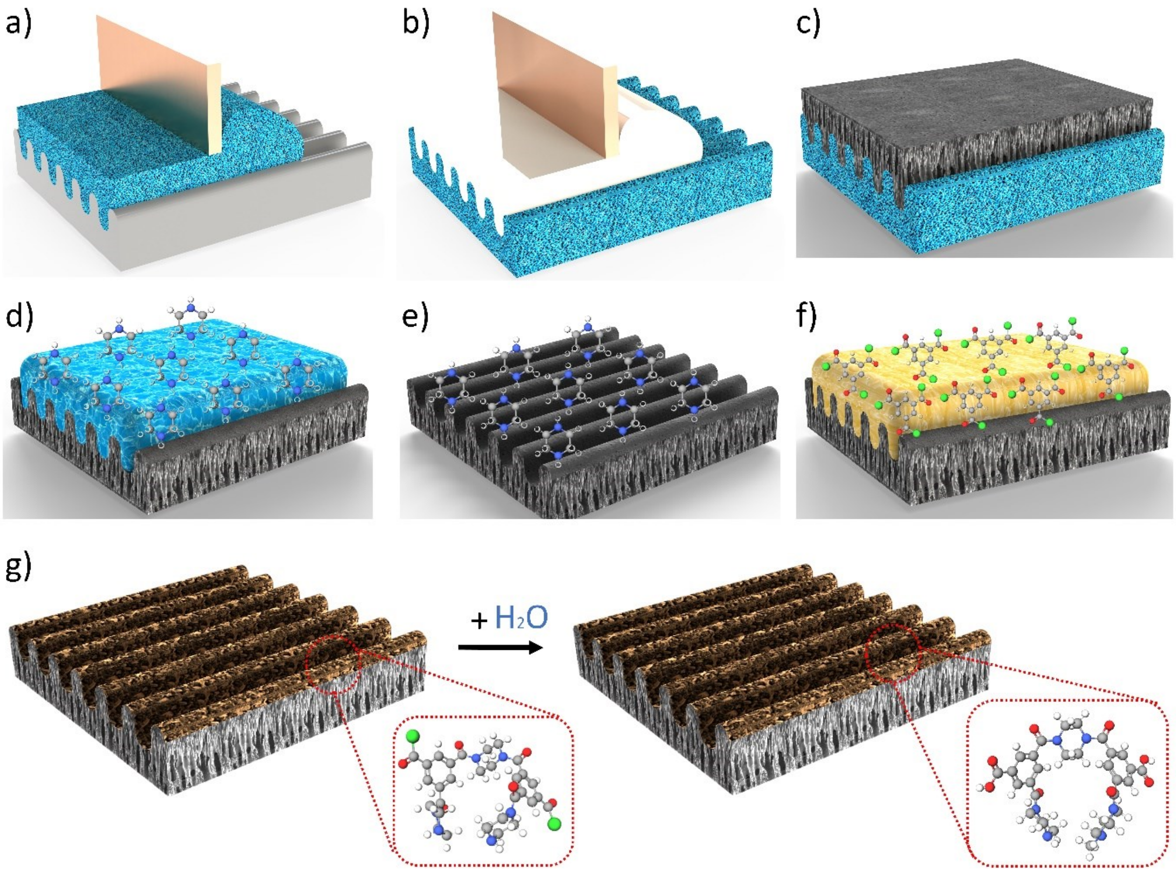

Figure 5. 1. The formation steps for HFPS and TFC patterned membranes. (a) Casting hydrogel solution on a patterned acrylic mold; (b) casting the PES polymer solution on the patterned side of the hydrogel mold; (c) resting the polymer solution on the hydrogel mold until the formation of membrane; (d) the first step of the IP reaction process in which the membrane was dried overnight and then covered with PIP aqueous solution for 11 minutes; (e) air-dring of the membrane surface to remove the excess aqueous solution; (f) pouring the TMC organic solution on the membrane surface to allow the PA formation; (g) Curing the membrane in an oven and then washing with distilled water to allow the hydrolysis of the unreacted acid chloride groups in the PA layer.

Table 5. 2. The PIP and TMC concentrations used to prepare the TFC membranes

Membrane	PIP Conc. (wt.%)	TMC Conc. (wt.%)
TFC-P 1	1	0.2
TFC-U 1	1	0.2
TFC-P 0.5	0.5	0.2
TFC-U 0.5	0.5	0.2
TFC-P 0.25	0.25	0.2
TFC-U 0.25	0.25	0.2

5.2.4 Characterization

5.2.4.1 Membrane morphology

Field emission scanning electron microscopy (FE-ESEM, Zeiss Sigma) was used to examine the membranes' cross-section and top surface. All membrane samples were dried overnight and then broken in liquid nitrogen. After that, samples were placed on an SEM stub holder containing a carbon tape coating. Before SEM, samples were sputter-coated with a gold layer of ~2 nm thickness. The surface roughness of membranes was measured using atomic force microscopy (AFM, Bruker Dimension edge, USA) in tapping mode under ambient conditions. The scanning rate and area were 1.0 Hz and 10 µm ×10 µm, respectively. The raw data were analyzed using NanoScope Analysis software, and the membrane surface roughness was expressed as the root mean square error (Rq) and average roughness (Ra). The cross-section of the polyamide layer was examined using transmission electron microscopy (TEM, FEI Morgagni 268 100kV).

5.2.4.2 Chemical composition analysis

The surface chemistry of all membranes was evaluated using attenuated total reflectance-Fourier transform infrared (ATR-FTIR, Agilent Cary 600 series). The absorbance spectrum was obtained over the range of 400-4000 cm^{-1} with a resolution of 4 cm^{-1}.

5.2.4.3 Wettability measurement

Contact angle analyzer equipment (Kruss GmbH, Germany) was used to measure the apparent contact angle of the prepared membranes. A small piece of each membrane was taped on a glass slide where the active side was faced up. Then, 2 μL distilled water droplet was gently placed on the membrane surface, and its contact angle was measured. Five contact angle measurements were recorded for each membrane sample.

5.2.4.4 Zeta potential measurement

A streaming zeta potential analyzer (Surpass 3, Anton Paar, Graz, Austria) was used to evaluate the surface zeta potentials of the unpatterned membranes over the pH range of 4-9. The electrolyte solution used in these measurements was 1 mM KCl, and its pH was adjusted automatically using NaOH and HCl. Measurements were repeated 3 times. We only provided results for the unpatterned membranes due to difficulties in mounting the patterned membranes in the slit microchannel of the streaming potential analyzer.

5.2.4.5 Filtration experiments

All filtration experiments were conducted using a crossflow filtration setup with the feed flow rate and transmembrane pressure of 3 $Lmin^{-1}$ and 40 psi, respectively. The feedwater temperature was fixed at 25±3 °C using a circulating chiller water bath (Fisher Scientific Isotemp 3013). The active membrane surface area was 20.6 cm^2. For each membrane, pure water filtration experiment was first performed for 2 hours until there was no change in the water flux readings (membrane compaction), followed by the addition of solutes/foulants. The permeated water was collected on a digital balance (ME4002, Mettler Toledo, USA), in which data was automatically recorded on a computer every 15 seconds. The permeate water flux (J_w) was calculated by:

$$J_w = \frac{m}{A\,\Delta t} \tag{6.1}$$

where m is the weight of the permeate water (L), A is the active surface area (m^2), and Δt is the time interval between recorded data (hr). After membrane compaction, solute/ foulant solutions including salts, dyes, and SAGD produced water were filtered for four hours each. Water samples were collected from the feed and permeate water and analyzed using conductometer, total organic carbon (TOC) analyzer, inductively coupled plasma-optical emission spectroscopy (ICP-OES, Agilent 735), and UV–Vis spectrophotometer (Thermo Fisher Scientific GENESYS™ 10), depending on the nature of the solutes. The following equation was used to calculate the rejection percentage (R):

$$R = \left(1 - \frac{C_p}{C_f}\right) \tag{6.2}$$

Where, C_p and C_f are the concentrations of solutes in the permeate and feed water, respectively.

5.3 Results and discussion

5.3.1 Morphological results

Figure 5.2 shows the cross-sectional SEM images of base and polyamide HFPS membranes. All membranes showed typical asymmetric finger-like internal structures with a dense skin layer. The left panel shows low magnification images of patterned and unpatterned membranes, including support layer (Base-P and Base-U) and PA-coated ones (TFC Patterned and TFC Unpatterned). These images prove that the base membranes kept their internal characteristics after the IP process was conducted to create the polyamide layer. The middle and right panels show high magnification cross-sectional images of the top side of the prepared membranes. It can be noticed from these images that the PES support is uniformly covered with the PA layer.

Figure 5.3 shows cross-section TEM images of the polyamide layer of all TFC membranes. The thickness of the polyamide layers is in the order of TFC-P/U 1 > TFC-P/U 0.5 > TFC-P/U 0.25. As can be noticed, the higher the PIP concentration, the thicker the polyamide layer. This can be attributed to the effect of PIP on the kinetics of IP reaction, which increases with more PIP content causing a high amine monomer partition rate from water to the n-hexane, leading to more growth of the PA layer [216,217]. Figure 5.4 shows SEM images of the top surfaces of all HFPS membranes. The left panel shows low magnification SEM images of the top surface of HFPS-base patterned, HFPS-base unpatterned, TFC patterned, and TFC unpatterned membranes. As shown, the overall pattern geometry was almost the same before and after the IP reaction, indicating the polyamide formation at the submicron scale. The middle and right panels show high magnification images for HFPS patterned and unpatterned membranes, including base and TFC polyamide membranes with different PIP concentrations (TFC-P 1, TFC-U 1, TFC-P 0.5, TFC-U 0.5, TFC-p 0.25, and TFC-U 0.25). It can be observed that the porous surface of base membranes was completely covered with the polyamide layer after the IP reaction. Moreover, as the concentration of PIP decreased from 1 wt.% to 0.25 wt.%, the polyamide ridges and valleys were flattened. This is confirmed with the 2D and 3D images of surface topography obtained by the AFM in Figure 5. Based on the AFM analysis, the average/root-mean-square surface roughness values for Base-P, Base-U, TFC-P 1, TFC-U 1, TFC-P 0.5, TFC-U 0.5, TFC-p 0.25, and TFC-U 0.25 are 16/14 nm, 20/15 nm, 28/20 nm, 24/18 nm, 19/15 nm, 22/16 nm, 17/13 nm, and 12/8 nm, respectively (Table 3). These results show that as the PIP concentration decreased from 1 wt.% to 0.25 wt.%, the average surface roughness decreased from 28±1 nm to 19±1 nm for patterned membranes and 22±2 nm to 12±1 nm for unpatterned membranes. A possible explanation is an increase in the release rate of nanosized gas bubbles during IP reaction at higher PIP concentrations. By increasing the PIP concentration, the kinetics of the IP reaction is enhanced, resulting in the rapid formation of the polyamide layer. As a result, and since the IP reaction is exothermic, a high heat generation rate evaporates the organic solvent and produces multiscale nodular shapes [218,219].

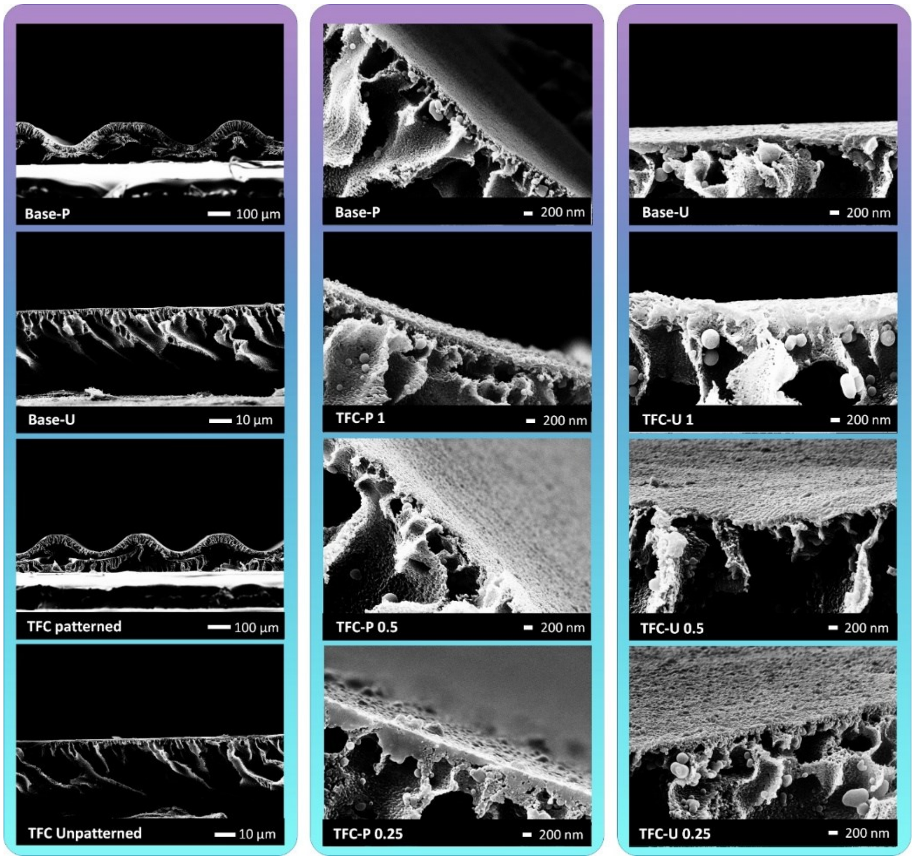

Figure 5. 2. Cross-sectional SEM images of all membranes including PES patterned (base-P), PES unpatterned (base-U), TFC patterned (TFC-P 1, TFC-P 0.5, and TFC-P 0.25), and TFC unpatterned (TFC-U 1, TFC-U 0.5, and TFC-U 0.25) membranes.

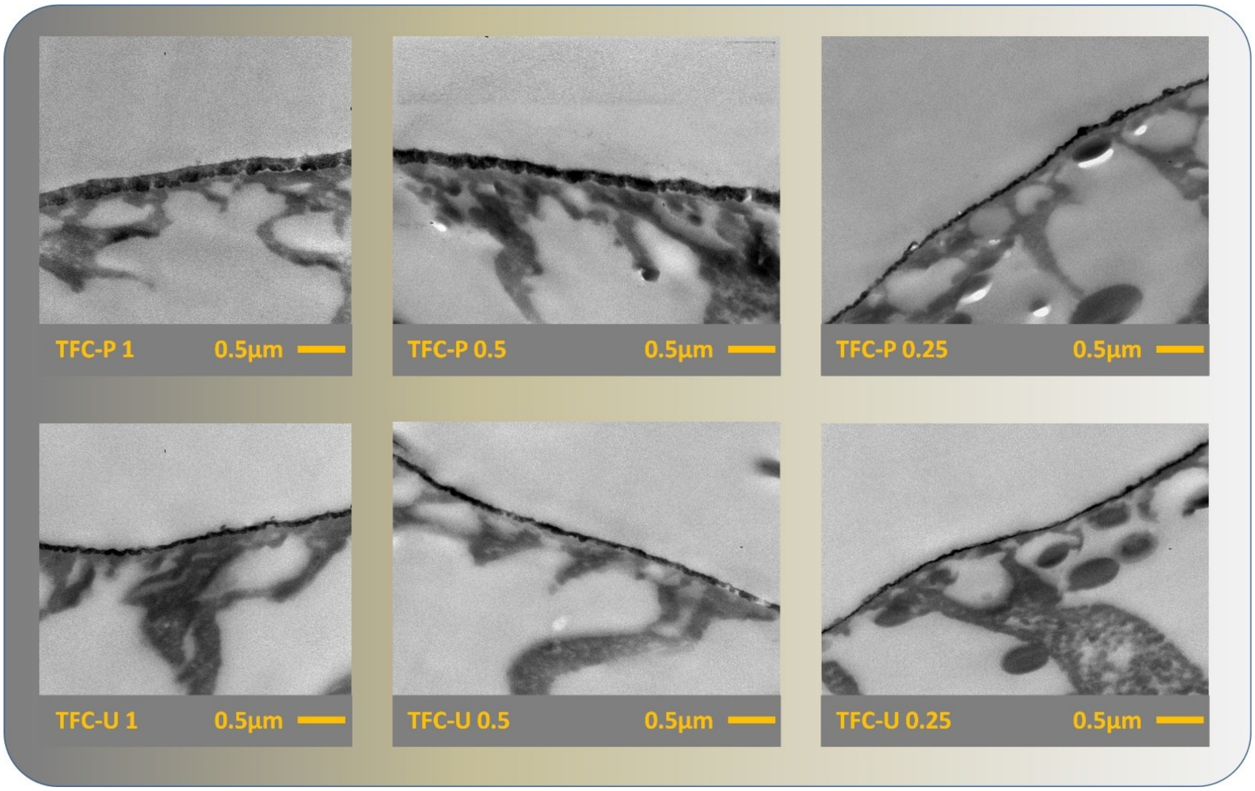

Figure 5. 3. Cross-sectional TEM images of TFC patterned and unpatterned membranes.

Table 5. 3. The surface roughness, water contact angle, and surface charge of the fabricated membranes

Membrane	Surface roughness		Water contact angle	Zeta Potential at pH 9
	Ra	Rq		
TFC-P	16 ±2	14 ±1	86±2°	----
TFC-U	20 ±2	15 ±1	92±2°	-28.9
TFC-P 1	28 ±1	20 ±1	38±1°	----
TFC-U 1	22 ±2	16 ±2	44±2°	-32.1
TFC-P 0.5	24 ±1	18 ±1	48±2°	-----

TFC-U 0.5	17 ±1	13 ±1	46±3°	-34.4
TFC-P 0.25	19 ±1	15 ±1	50±1°	-----
TFC-U 0.25	12 ±1	18 ±1	55±2°	-37.1

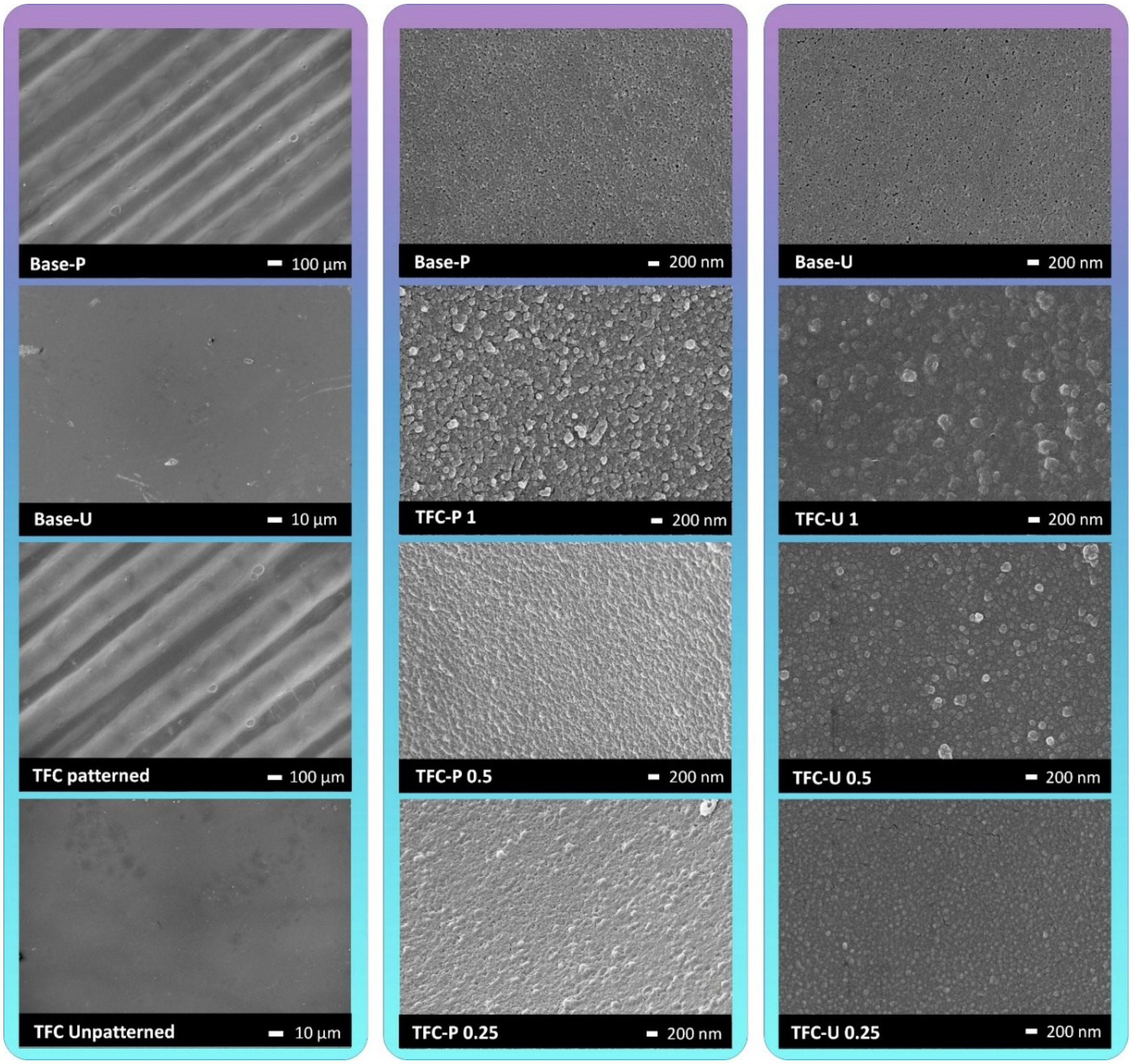

Figure 5. 4. SEM images of the top surface of all membranes including PES patterned (base-P), PES unpatterned (base-U), TFC patterned (TFC-P 1, TFC-P 0.5, and TFC-P 0.25), and TFC unpatterned (TFC-U 1, TFC-U 0.5, and TFC-U 0.25) membranes.

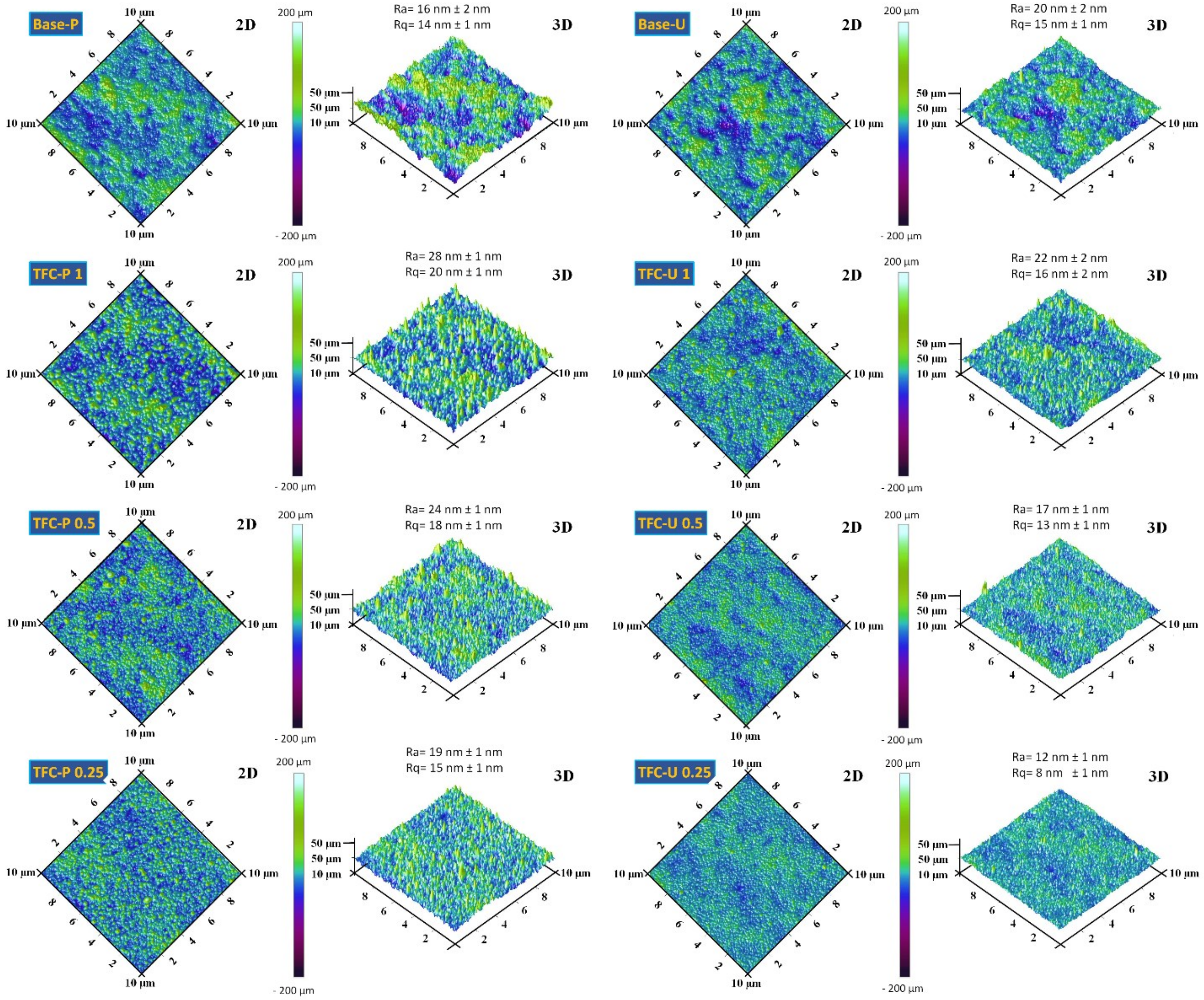

Figure 5. 5. AFM images of the surface roughness of all prepared membranes. For each membrane, 2D/3D images, average roughness (R_a), and root mean square error of the surface were obtained using NanoScope Analysis software.

5.3.2 ATR-FTIR results

The surface chemistry of the synthesized membranes was evaluated using ATR-FTIR analysis. Figure 6 shows the absorbance spectrum of the base and polyamide-coated membranes over the wavenumber of 1000-3800 cm^{-1}. The prominent polyamide peaks, namely, O-H bending vibration and C=O stretching vibration, are located at 1440 cm^{-1} and 1630 cm^{-1}, respectively [220]. In addition, the broad peak located at 3450 cm^{-1} is due to the hydroxyl groups (−OH), which are formed due to the partial hydrolysis of the unreacted acyl chloride groups of TMC.[221,222] These distinct peaks were found in all PA-coated membranes and were absent in the base PES substrate, confirming the formation of the PA layer. As can be seen, the PA peak intensities varied with the PIP concentration. The PA peak intensities were in the order of TFC-P 1, TFC-U 1> TFC-P 0.5, TFC-U 0.5> TFC-P 0.25, TFC-U 0.25, indicating higher concentration of amide linkage formed with the increase of PIP concentration [223].

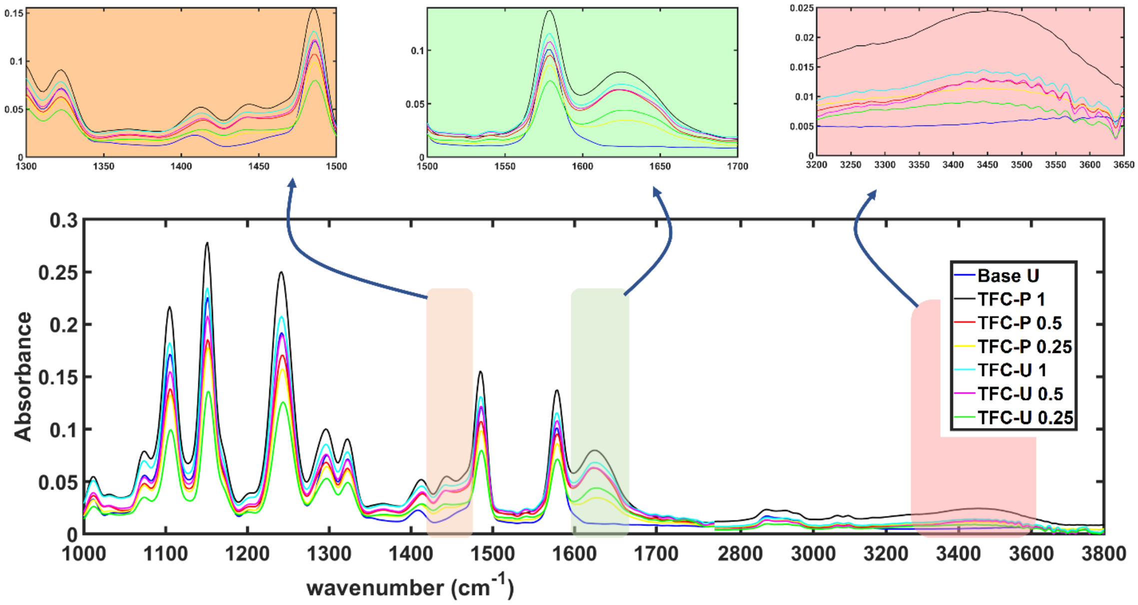

Figure 5. 6. The absorbance spectrum of the base and polyamide membranes obtained by the ATR-FTIR analysis.

5.3.3 Zeta potential results

The surface charge of the unpatterned membranes, including base and TFC, is shown in Figure 7. All membranes exhibit a negative surface charge over the pH range of 4-9. The negative surface charge of the base PES membranes originates from the adsorption of anions from the electrolyte solution to the membrane surface and dissociation of pendant sulfonate ($-SO_3H$) groups in PES into negatively charged $-SO_3^-$ [224,225]. The enhanced ionization rate of $-SO_3H$ at higher pH values makes the PES surface more negatively charged. It is worth noting that the isoelectric point of our fabricated PES membranes is ~3.5, which matches well with the literature [226]. For the TFC membranes, the negative surface charge is attributed to the ionization of acidic carboxyl groups (–COOH) into $R-COO^-$ [227]. It must be noted that polyamide membranes contain both weakly acidic –COOH and weakly basic amine ($-NH_2$) groups, allowing the surface to have either a positive or negative charge based on solution pH. The equilibrium dissociation reactions of R–COOH ($R-COOH \Leftrightarrow R-COO^- + H^+$) and $R-NH_2$ ($R-NH_3^+ \Leftrightarrow R- NH_2 + H^+$) govern the surface charge, depending on the degree of ionization and the pH of the solution. As the PIP concentration increases, more polymer forms and the content of the$-NH_2$ groups increases, which possibly has led to less negative surface zeta potential values (see Table 3 and Figure 7) [216,228].

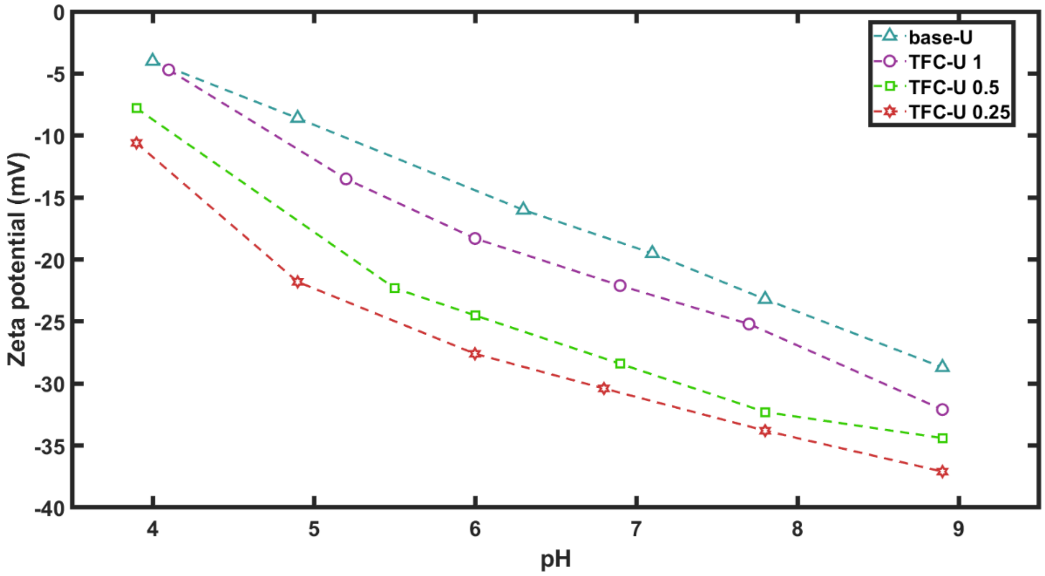

Figure 5. 7. The surface charge of the base and TFC unpatterned membranes obtained by streaming zeta potential analyzer.

5.3.4 Contact angle results

The wettability of the prepared membranes is investigated by measuring the water contact angle (CA) and the results are presented in Table 3 and Figure 8. As shown in Figure 8, the water CA dropped significantly after coating the base membranes with the polyamide layer due to the presence of hydrophilic carboxyl groups at the surface of TFC PA membranes [229]. This suggests that the higher carboxyl group content at the membrane surface, the lower the CA values. Given that, the CA values are found to be in the order TFC-U/P 1<TFC-U/P 0.5< TFC-U/P 0.25, implying the presence of more carboxyl groups in the polyamide matrix when more acid chlorides reacted with amines at higher concentrations of PIP. The unreacted TMC monomers are most likely washed or leached out during the rinsing step of the IP process. Other than surface chemistry, the surface physical heterogeneities can also control the surface wettability [166]. Wenzel's model relates the wettability and the surface roughness so that an increase in the surface roughness magnifies the wettability caused by the surface chemistry. This means that a rougher hydrophilic surface shows a higher wettability and thus lower CA values. Based on AFM results, the order of surface roughness is TFC-U/P 1>TFC-U/P 0.5> TFC-U/P, which agrees with the wettability trend. It is worth mentioning that the wettability of patterned membranes was lower than unpatterned ones due to ridges & valleys, which helped spread the water droplet on the surface. This behavior was also observed in our previous studies [26,188].

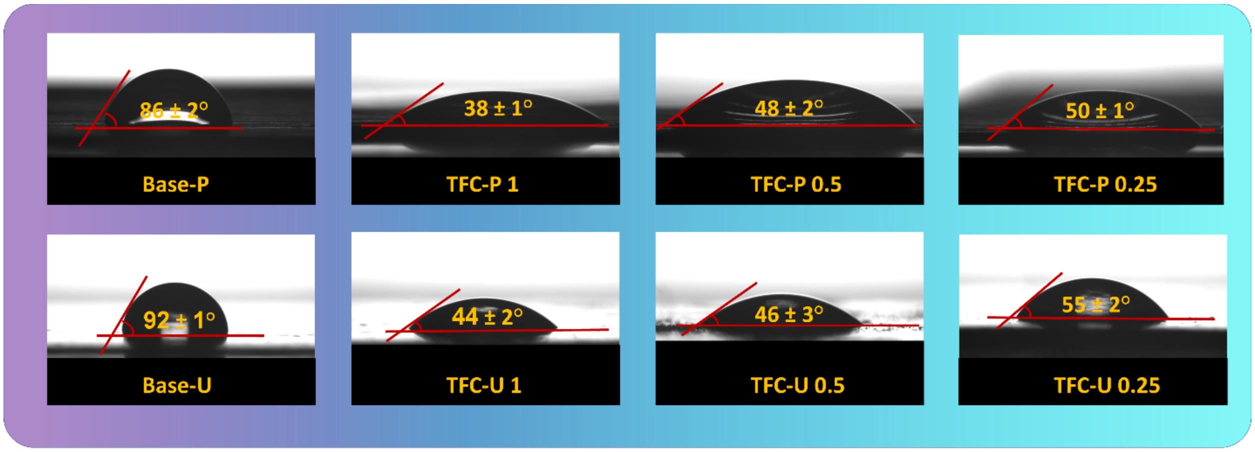

Figure 5. 8. The static water contact angle of synthesized membranes. The water droplet size was adjusted at 2 µL for all membranes.

5.3.5 Filtration results

The filtration performance of the prepared membranes was evaluated using a crossflow filtration setup at a fixed transmembrane pressure of 40 psi. Figure 9 and Table 4 show the water flux and the separation performance of fabricated membranes to reject divalent ($MgSO_4$, Na_2SO_4) and monovalent (NaCl) ions. As can be observed, the water flux through the patterned TFC-P 1, TFC-P 0.5, and TFC-P 0.25 was 20%, 36%, and 96% higher than the corresponding unpatterned membranes, respectively. This improvement can be attributed to a 34% increase in the surface area, calculated using Image J software [26]. Interestingly, the typical trade-off relation between flux and rejection did not affect the separation performance of patterned membranes to remove divalent ions. The maximum reduction in divalent ion rejection (13% for $MgSO_4$ and 6% for Na_2SO_4) was observed for TFC-P 0.25, which can be compromised with almost 100% water flux enhancement through this membrane. Nevertheless, the NaCl rejection of patterned TFC-P 0.5 and TFC-P 0.25 membranes decreases more considerably than that of unpatterned membranes. Since NF membranes are typically designed to remove divalent ions, such a reduction in monovalent ion rejection would not affect the practicality of our fabricated membranes for water softening. Salt rejection results show similarities between the TFC patterned and unpatterned membranes and followed the order $Na_2SO_4 \geq MgSO_4 > NaCl$ (Figure 9b, c, and d). The separation mechanisms of NF membranes are Donnan exclusion and size sieving. Solute molecules with a size bigger than the membrane pores are mainly separated via sieving, while those with a size similar or slightly lower than the membrane pores can be separated by electrostatic repulsion (Donnan exclusion). Since poly(piperazine-amide) NF membranes has negative surface charge, multivalent anion such $SO_4^{2-}$is well rejected while the rejection of cations (Na^+ & Mg^{2+}) is low. Regardless of the type of membrane, as the PIP concentration decreases, the flux increases, which can be attributed to the reduction in the thickness of the PA layer, as shown by TEM results (Figure 3). Moreover, previous studies showed that a decrease in the PIP concentration decreased the PA layer's crosslink density, which can also directly affect the flux results [216].

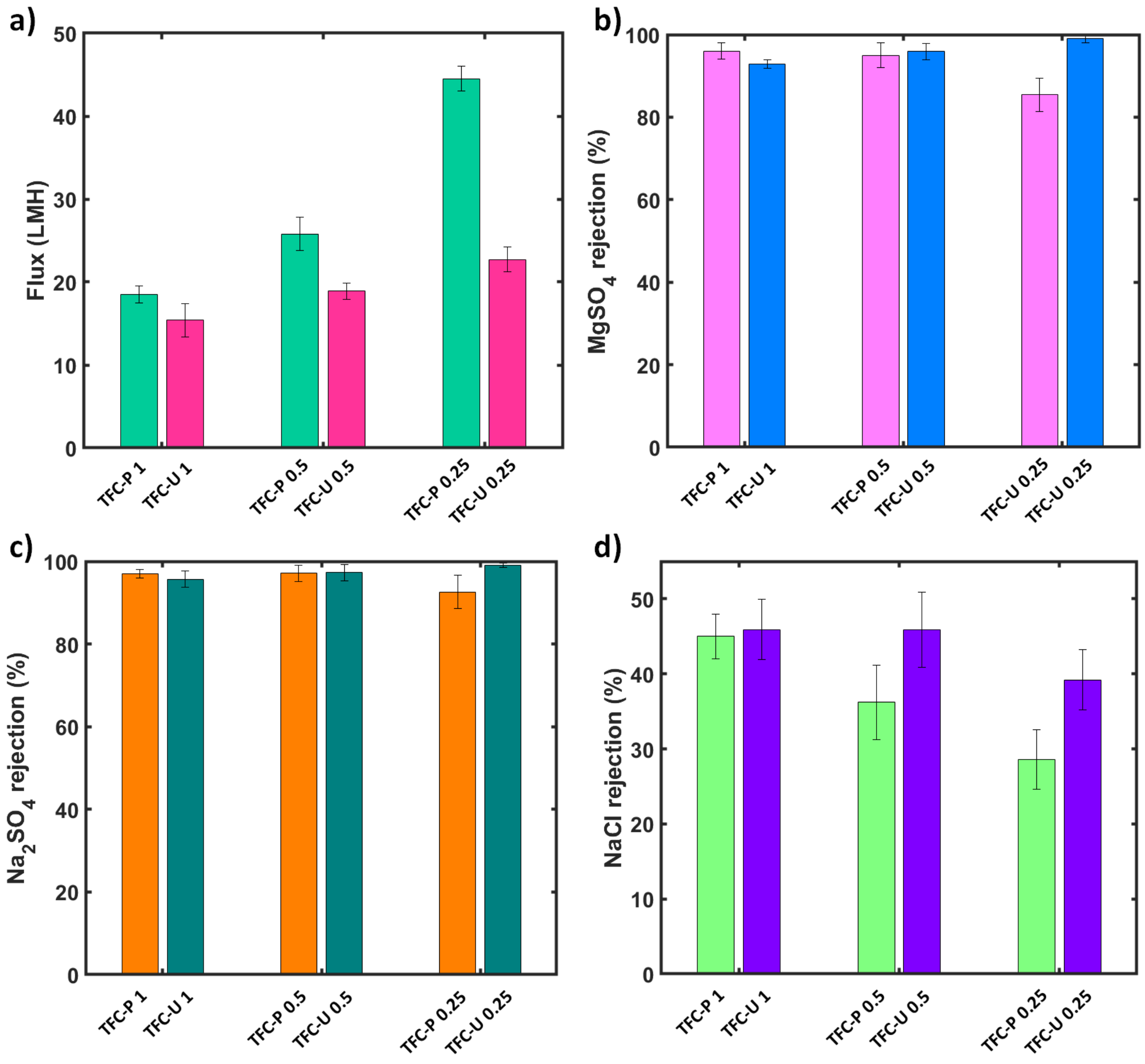

Figure 5. 9. (a) filtration performance of the prepared membranes at 40 psi transmembrane pressure, and the separation performance of membrane to remove (b) $MgSO_4$, (c) Na_2SO_4, and (c) NaCl.

Table 5. 4. The filtration performance of the prepared TFC membranes and the separation results for salts and dyes.

Membrane	**Salt rejection (%)**	**Dye rejection (%)**

	Water flux (LMH)	MgSO4	Na_2SO_4	NaCl	RB5	Methyl Orange
TFC-P 1	18.5	96	97	45	>99	94
TFC-U 1	15.4	92.9	95.7	45.9	>99	93
TFC-P 0.5	25.8	95	97.1	36.2	>99	94.5
TFC-U 0.5	18.9	95.9	97.3	45.9	>99	94
TFC-P 0.25	44.5	85.4	92.6	28.6	>99	92.1
TFC-U 0.25	22.7	99	99	39.2	>99	95

The separation performance of fabricated membranes for dye (RB5 and MO) removal was investigated, and the results are shown in Figure 5.10 and Table 5.4. The TFC membranes showed separation performance of >99% and 92-95% for RB5 and MO, respectively. Based on the MO rejection results, the molecular weight cut-off (MWCO) of the TFC membranes is estimated to be in the range of 270-300 Da. The MWCO is defined as the smallest molecular weight of a solute that is retained by a membrane with a percentage of 90. Interestingly, TFC-P 0.25 exhibits high dyes rejection and flux values making it an excellent candidate for textile wastewater treatment. Figure 5.10c shows images of RB5 and MO dye of feed and permeate water through all TFC membranes.

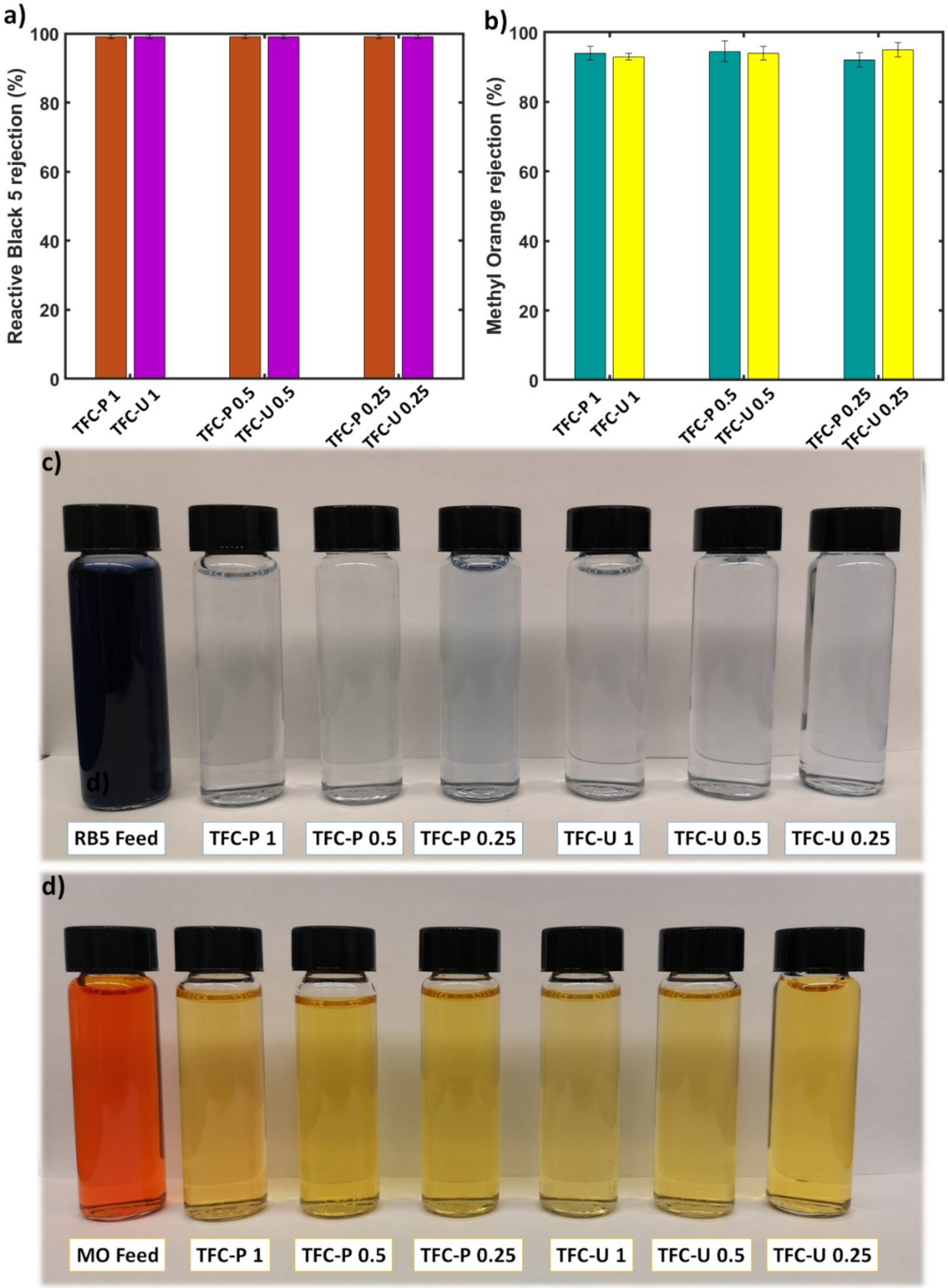

Figure 5. 10. The separation performance of the prepared membranes for (a) reactive black 5 and (b) methyl orange dyes, and (c) pictures of the feed and permeate solutions after the treatment of dye solutions.

The rejection values of major constituents in SAGD produced water (iron, potassium, sodium, and sulfur), as well as TOC and TDS rejection by the TFC membranes, are presented in Figures 11. The synthesized membranes could remove 90-92%, 80-85%, 99%, 76-89%, 75-89%, and 98-99% of TOC, TDS, iron, potassium, sodium, and sulfur from BFW. The ultimate goal for producing patterned membranes was to overcome the trade-off relationship between flux and rejection, which was achieved by looking at rejection results. TOC removal did not change, and the rejection of monovalent ions reduced slightly (<10%), indicating the high performance of fabricated patterned NF membranes for water softening and treatment of oil sands produced water. Figure 11g shows water samples of the feed (BFW) and permeate of the fabricated membranes. The high-quality permeates of our NF membranes reduce the fouling and scaling of boiler tubes and thus reduce the operating costs of resource extraction in Alberta, Canada. Finally, all fabricated membranes in the present work did not exhibit any flux decline for all fouling tests, likely due to the combination of high hydrophilicity, low surface roughness, and negatively charged surface, providing yet another value to membrane water purification.

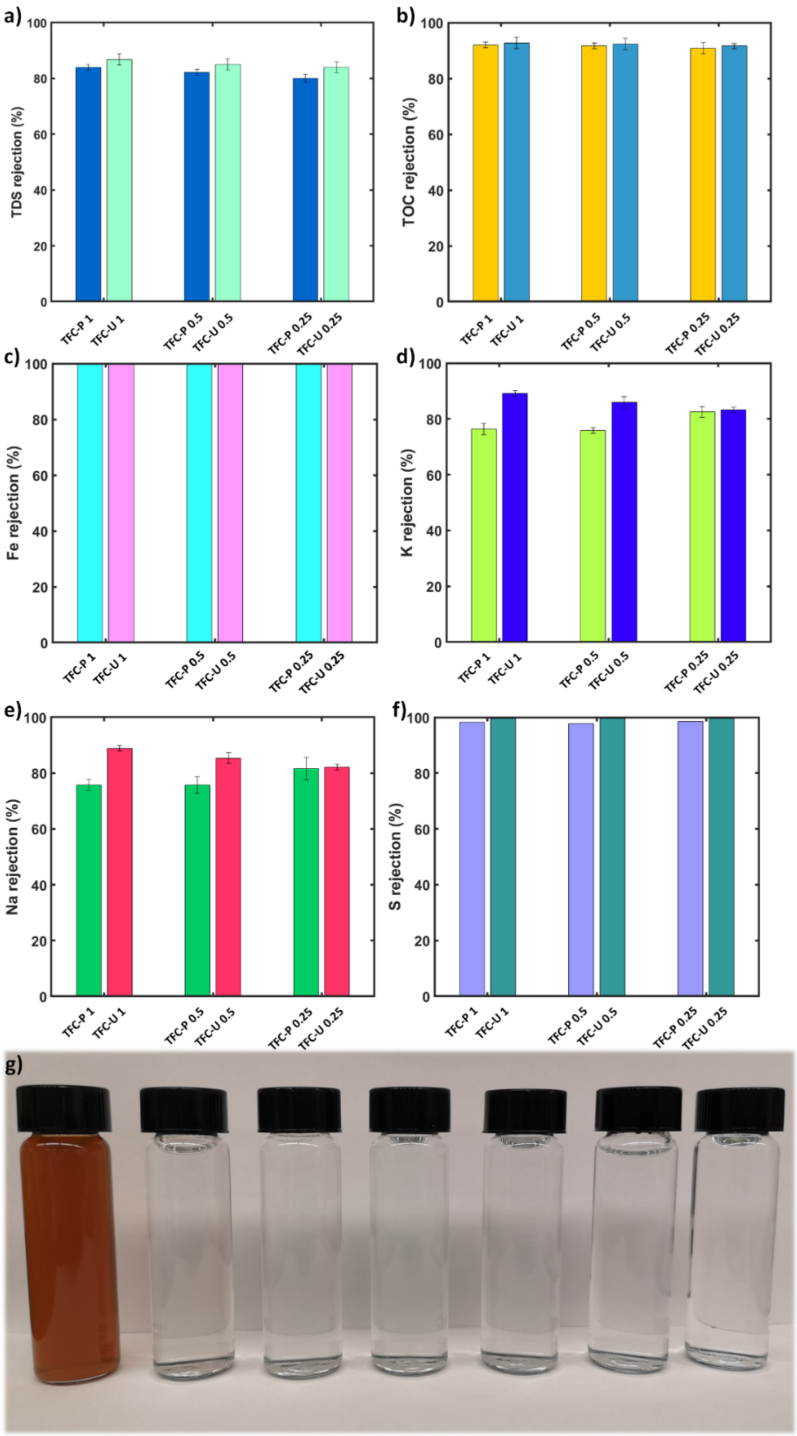

Figure 5. 11. (a)-(f) The separation performance of the TFC membranes for TOC and TDS removal and removal of iron, potassium, sodium, and sulfur from SAGD produced water, and (g) pictures of feed and permeate water samples after treatment of SAGD BFW.

Table 5.5 presents a comparison between our best membranes, TFC-P 0.5 and TFC-P 0.25, with some of the best commercial NF membranes and recently fabricated NF membranes in the literature. The performance of our membranes is superior to most of them, especially the ones that only used PIP and TMC without additives. We acknowledge that some published work demonstrated higher performances since they utilized additives such as surfactants in the IP reaction. Nevertheless, by applying such modifications to our patterned membranes, higher performances would have been achieved. Most importantly, our membranes showed comparable results with the state-of-the-art commercial membranes because of the enhanced surface area.

Table 5. 5. Comparison of our best membranes with other TFC NF membranes.

Membrane	**Water flux (LMH/bar)**	**Salt rejection (%)**			**Ref.**
		MgSO4	**Na_2SO_4**	**NaCl**	
PAN PDA/PEI/GA	1.6	93	----	50	[201]
PES-poly(aryl cyanurate)	1.7	92.8	97.1	51.3	[189]
PAN PDA/PEI/TMC	2.1	93.6	92.4	27.8	[230]
PES PIP/IPC	2.9	77.7	----	51.8	[215]
PES PIP/TMC salt modified	5.1	98	----	49	[231]
PES PEI/TMC	5.1	90	60	31	[186]
MWCNT-NH/ PIP/TMC	5.3	95	96.8	35.1	[232]
PAN PDA/PEI/GA - SiO2	5.3	70	----	25	[233]

PES PIP/TMC	6.2	94.5	----	30.2	[215]
PES PIP/TMC	6.25	95.3	97.1	15	[216]
PES PIP/TMC	6.1	98	99	16	[186]
MWCNT-COOH/ PIP/TMC	6.2	93.7	96.6	34	[232]
MWCNT-OH/ PIP/TMC	6.9	97.1	97.6	35.3	[232]
PMMA MWCNT-PIP/TMC	6.9	96	99	44.1	[234]
PSF-PVA PIP/TMC	7.65	95.9	----	16	[235]
PES PIP/TMC	9.1	92	95.2	22	[236]
PES PIP/TMC-SDS	9.25	98.2	99.6	27	[216]
PAN PEI/TMC	9.5	77	----	45	[237]
PES PIP/TMC	10.6	78	----	44	[238]
PES PIP/BP	11.1	----	90	22	[239]
PEI PIP/TMC	11.6	----	95	----	[222]
PES PIP/TMC-CTAB	22.5	90.9	98.1	9.9	[216]
PAN- PIP/BP	22.9	98	----	----	[240]
PES-PVA PIP/TMC	31.4	96	99.4	49	[236]
NF270	22	95	98	35	[236]
NF 90	10.4	100	----	----	[240]
SUEZ (HL)	5.5	98	----	----	
Synder (NDX)	9.8	90	----	----	
TriSep (XN45)	7.6	95	----	----	
TFC-P 0.5	**9.4**	**95**	**97.1**	**36.2**	**This work**
TFC-P 0.25	**16.2**	**85.4**	**92.6**	**28.6**	**This work**

5.4 Conclusion

In this work, we fabricated novel poly(piperazine amide) NF micropatterned membranes using interfacial polymerization on a hydrogel facilitated phase separation substrate. The fabricated TFC membranes, including micropatterned and unpatterned, were tested through the filtration of $MgSO_4$, Na_2SO_4, NaCl, Reactive Black 5 dye, Methyl Orange dye, and a real boiler feed water collected from the oil sands industry in Canada. The fabricated membranes showed exceptional characteristics such as low surface roughness, high hydrophilicity, and high negative surface charge. For each PIP concentration, the filtration performance of patterned TFC membranes (TFC-P 1, TFC-P 0.5, and TFC-P 0.25) showed higher water flux compared to unpatterned membranes. The best membrane was TFC- P 0.25, which showed an almost 100% increase in the flux with a slight reduction in the rejection values of ions and dyes as compared to the corresponding unpatterned membrane. This straightforward and feasible physical surface modification method proposed in this article managed to overcome the trade-off relationship between flux and rejection and can potentially dominate the NF field.

Chapter 6

Concluding Remarks and Future Direction of Research

6.1 Conclusion

In this dissertation, a new generation of patterned membranes with superior performances has been developed that allows the implementation of an energy-efficient membrane filtration system for wastewater treatment.

In the first part of this research work, a new method to directly apply micro-scale patterns on phase inversion membranes was invented; the method we named hydrogel facilitated phase separation (HFPS). Hydrogel is a water swollen polymeric material that can hold and retain large amounts of water and be molded from almost any patterned surface. The advantages of hydrogel allowed patterning membranes without changing the surface chemistry while maintaining a selective dense layer at the patterned side. The morphological properties of the HFPS membranes showed similarities with the conventional NIPS membranes, but slight average pore enlarging was observed in the HFPS membranes. This was mainly attributed to the demixing rate difference between hydrogel and water. The permeation results showed that patterned membranes almost doubled the flux results compared with unpatterned ones. This increase was attributed to the addition of surface area and the slight increase in the membrane average pore size. BSA fouling results showed a 78% increase in the flux for the patterned membrane compared with the unpatterned one after 100 minutes of filtration time.

In the second part of this research work, a feasible and straightforward treatment process was developed to allow the continuous use of the same hydrogel mold in making patterned membranes. In HFPS, a soft lithographically patterned hydrogel mold is used as a water content source that initiates the phase separation process in membrane fabrication. After each membrane casting, however, the hydrogel content changes due to the diffusion of the organic solvent into the hydrogel from the original membrane solution. The absorption of solvent into the hydrogel mold limits the continuous use of the mold in repeated membrane casts. The idea of our treatment method was to extract the diffused organic solvent inside the hydrogel after each membrane formation without damaging the hydrogel structure. The proposed method consists of warm and cold treatment steps that allow the highest water content recovery without affecting the hydrogel integrity. The best recovery result was 96% which was achieved by placing the hydrogel mold in warm (50 ºC) and cold water (23 ºC) baths for 10 and 4 minutes, respectively. This recovery was attributed to nearly complete solvent extraction without any deformation of the hydrogel structure. The reusability of the hydrogel can assist in the development of a continuous membrane fabrication process using HFPS.

In the third phase of this research work, novel polyamide-imide (PAI) microfiltration membranes were developed using HFPS and NIPS methods for the separation of oil in water emulsion. The PAI concentration in the dope solutions varied from 8 to 4 wt.% for each method. Lowering the PAI concentration in the dope solutions significantly influenced the morphological properties of the prepared membranes, primarily reduced the thickness of the skin layer and increased the bulk and surface porosities. We found that by reducing the concentration of PAI from 8 wt.% to 4 wt.%, the skin layer thickness of the HFPS membranes decreased by 65%, while the bulk porosity increased by 13%. The prepared membranes showed superhydrophilicity, underwater superoleophobicity, and high porosity, making them excellent candidates for the separation of oil/water emulsion under gravity. The HFPS patterned membranes showed complete repellency for diesel, n-hexadecane and mineral oils. All fabricated membranes showed >99.9% oil removal efficiency under gravity-driven filtration experiments. The best membrane was patterned with 4wt.% PAI (PM4) which showed flux results of 440 LMH and FRR and FD after 18 filtration experiments of >98% and <6%, respectively. Such an excellent antifouling property was attributed to the superhydrophilicity and underwater superoleophobicity of PM4. The OCA of the prepared membranes for n-hexadecane, diesel, and mineral oils were in the range of 146-153 °, no attachment, and 152-158 °, respectively. Benefiting from the natural super-wetting properties of the PAI and the advantages of the HFPS method, the fabricated membranes in this study showed superior filtration performance, in terms of permeation, FD, FRR, and oil separation, compared to the membranes reported in the literature.

In the fourth phase of this research work, we synthesized a novel poly(piperazine amide) NF micropatterned membranes using interfacial polymerization reaction between PIP and TMC on a hydrogel facilitated phase separation substrates. The concentration of PIP was varied from 1wt.% down to 0.25 wt.% for both patterned and unpatterned substrate forming 6 TFC membranes (TFC-P 1, TFC-P 0.5, TFC-P 0.25, TFC-U 1, TFC-U 0.5, and TFC-U 0.25) in total. The SEM images of the top surface of the HFPS patterned and unpatterned membranes, showed complete coverage of the surface pores after coating the membranes with the Polyamide layer. The average surface roughness values of the TFC membranes were between 12-28 nm which are very favorable to prevent membrane fouling. The water contact angle values of Base-P, Base-U, TFC-P 1, TFC-U 1, TFC-P 0.5, TFC-U 0.5, TFC-P 0.25, and TFC-U 0.25 were 86°, 92°, 38°, 44°,48°, 46°, 50°, and 55°, respectively. As shown in figure LMN, there was a significant drop in the water CA values between base PES and TFC membranes due to the hydrophilic nature of PA layer induced by the IP reaction. The filtration performance of the TFC membranes was evaluated through the separation of different salts (e.g., $MgSO_4$, Na_2SO_4, and NaCl), Reactive Black 5 dye, Methyl Orange dye and the treatment of real oil sands produced water. The water flux of TFC-P 1, TFC-U 1, TFC-P 0.5, TFC-U 0.5, TFC-P0.25, TFC-U 0.25 was 18.5, 15.4, 25.8, 18.9, 44.5 and 22.7 LMH, respectively. The increment in the flux results for TFC-P 1, TFC-P 0.5, and TFC-P 0.25

compared with the unpatterned membranes were 20%, 36% and 96%, respectively. Moreover, the TFC membranes showed separation performance of >99% and 92-95% for Reactive Black 5 and Methyl Orange dyes, respectively. Lastly, the synthesized membranes could remove 90-92%, 80-85%, 99%, 76-89%, 75-89%, and 98-99% of TOC, TDS, iron, potassium, sodium, and sulfur from Boiler Feed Water. The ultimate goal for producing patterned membranes was to overcome the trade-off relationship between flux and rejection, which was achieved by looking at the filtration performance. This straightforward and feasible physical surface modification method proposed in this article managed to overcome the trade-off relationship between flux and rejection and can potentially dominate the NF field.

6.2 Possible future directions

Based on the accomplished works, the following future directions of research are identified:

- Preparing superhydrophobic PVDF patterned membranes for the membrane distillation (MD) process. MD is a thermally-driven membrane separation process where water vapor molecules transport from a feed stream to a permeate stream through a microporous hydrophobic membrane. In MD only water vapor passes through the membrane. Theoretically, a complete separation can be achieved. The major drawbacks of MD are low permeate flux and high susceptibility to flux decline over time due to both temperature and concentration polarization phenomena [241]. The formation of patterned hydrophobic PVDF membranes can improve the permeation flux due to the increase in the surface area and reduce the temperature polarization effect by increasing the secondary flows at the vicinity of the membrane surface [242].
- Investigating the feasibility of integrating the HFPS method into the Roll-to-Roll manufacturing process for continuous production.

- Modifying the polymer content of the hydrogels and the specific polymer blends within the solvent mixture to increase the demixing rate of the HFPS process. This step will allow us to produce micropatterned phase inversion membranes with equal pore sizes and rejection rates as conventional NIPS membranes, but significantly higher flux can be produced.

6.3 List of contributions

6.3.1 Journal papers

1. Asad, Asad, et al. "Micro-patterned Thin Film Composite Poly(piperazine-amide_ Nanofiltration Membranes for Wastewater Treatment." Submitted.
2. **Asad**, Asad, et al. "Gravity assisted super high flux microfiltration polyamide-imide membranes for oil/water emulsion separation." *Journal of Membrane Science* 621 (2021): 119019.
3. Asad, Asad, et al. "Durability and recoverability of soft lithographically patterned hydrogel molds for the formation of phase separation membranes." *Micromachines* 11.1 (2020): 108.
4. Asad, Asad, Mohtada Sadrzadeh, and Dan Sameoto. "Direct micropatterning of phase separation membranes using hydrogel soft lithography." *Advanced Materials Technologies* 4.7 (2019): 1800384.
5. Rastgar, Masoud, et al. "Removal of trace organic contaminants by melamine-tuned highly cross-linked polyamide TFC membranes." *Chemosphere* 238 (2020): 124691.
6. Khondoker, Mohammad Abu Hasan, Asad Asad, and Dan Sameoto. "Printing with mechanically interlocked extrudates using a custom bi-extruder for fused deposition modelling." *Rapid Prototyping Journal* (2018).

6.3.2 Patents

7. **Asad Asad**, Dan Sameoto, Mohtada Sadrzadeh, Patterned Microfilter Membrane and Method of Preparing the Same, US Patent Application Serial No. 62/530,445, Date of Filing: July 10, 2017.

7.3.3 Book chapters

8. Asad, Asad, Dan Sameoto, and Mohtada Sadrzadeh. "Overview of membrane technology." *Nanocomposite Membranes for Water and Gas Separation*. Elsevier, 2020. 1-28.

6.3.3 conference presentations

9. Asad Asad, Masoud Rastgar, Mohtada Sadrzadeh, and Dan Sameoto, 2020. Development of Super High Flux Microfiltration Polyamide-imide Membranes for Gravity Assisted Oil/Water Emulsion Separation. The Adhesion Society conference.
10. Asad, Asad, et al, 2020. Durability and Recoverability of Soft Lithographically patterned hydrogel molds for the formation of Phase Separation membranes. *International Congress on Membranes & Membrane Processes (ICOM).*
11. **Asad, A.,** Sameto, A. and Sadrzadeh, M., 2019. New generation of patterned membranes for water treatment. *North American Membrane Society* (NAMS).
12. Huthaifa Abu Saris, **Asad Asad**, Mohtada Sadrzadeh, (2019). Automated Roll-to-Roll membrane manufacturing system. *COSIA Innovation Summit.*
13. **Asad, A.,** Sameoto, D. and Sadrzadeh, M., 2019. New generation of patterned membranes for water treatment. *International Conference on Environmental Science and Technology (CEST).*
14. Sadrzadeh, M., Khorshidi, B., Nazaripoor, H., Karkooti, A., **Asad, A**. and Koupaei, A., 2019. Nano-enabled membranes for Canada's oil sands produced water treatment. *TechConnect World Innovation Conference*.
15. **Asad, A.**, Nazaripoor, H., Sameoto, D. and Sadrzadeh, M., 2018. Development of micro/nano-patterned membranes with improved permeation and antifouling properties for the treatment of SAGD produced water. *COSIA Innovation Summit.*

References

[1] S. Zhao, L. Zou, C.Y. Tang, and D. Mulcahy. Recent developments in forward osmosis: opportunities and challenges. J.Membr.Sci., 396 (2012) 1.

[2] G.M. Geise, H. Lee, D.J. Miller, B.D. Freeman, J.E. McGrath, and D.R. Paul. Water purification by membranes: the role of polymer science. Journal of Polymer Science Part B: Polymer Physics, 48 (2010) 1685.

[3] M.A. Shannon, P.W. Bohn, M. Elimelech, J.G. Georgiadis, B.J. Mariñas, and A.M. Mayes. Science and technology for water purification in the coming decades. Nature, 452 (2008) 301.

[4] A. Politano, P. Argurio, G. Di Profio, V. Sanna, A. Cupolillo, S. Chakraborty, et al. Photothermal membrane distillation for seawater desalination. Adv Mater, 29 (2017).

[5] N.X. Tsiourtis. Desalination and the environment. Desalination, 141 (2001) 223.

[6] N. Hunter. Water reuse: Making use of wastewater. Filtration Sep., 44 (2007) 24.

[7] C. Charcosset. Membrane processes in biotechnology: an overview. Biotechnol.Adv., 24 (2006) 482.

[8] M. Pizzichini, C. Russo, and C. Di Meo. Purification of pulp and paper wastewater, with membrane technology, for water reuse in a closed loop. Desalination, 178 (2005) 351.

[9] J. Radjenović, M. Petrović, and D. Barceló. Fate and distribution of pharmaceuticals in wastewater and sewage sludge of the conventional activated sludge (CAS) and advanced membrane bioreactor (MBR) treatment. Water Res., 43 (2009) 831.

[10] M. Noronha, T. Britz, V. Mavrov, H. Janke, and H. Chmiel. Treatment of spent process water from a fruit juice company for purposes of reuse: hybrid process concept and on-site test operation of a pilot plant. Desalination, 143 (2002) 183.

[11] V. Mavrov, E. Bélières. Reduction of water consumption and wastewater quantities in the food industry by water recycling using membrane processes. Desalination, 131 (2000) 75.

[12] M. Sadrzadeh, D. Pernitsky, and M. McGregor. Nanofiltration for the Treatment of Oil Sands-Produced Water. Edited by Muhammad Akhyar Farrukh, (2018) 25.

[13] A. Karkooti, A.Z. Yazdi, P. Chen, M. McGregor, N. Nazemifard, and M. Sadrzadeh. Development of advanced nanocomposite membranes using graphene nanoribbons and nanosheets for water treatment. J.Membr.Sci., (2018).

[14] M. Elimelech, W.A. Phillip. The future of seawater desalination: energy, technology, and the environment. Science, 333 (2011) 712.

[15] M. Lee, Z. Wu, and K. Li, Advances in ceramic membranes for water treatment, in Anonymous , Advances in Membrane Technologies for Water Treatment, Elsevier, 2015, pp. 43-82.

[16] R.W. Baker, Updated by Staff. Membrane technology. Kirk-Othmer Encyclopedia of Chemical Technology, (2000).

[17] J. Mulder, Basic principles of membrane technology, , Springer Science & Business Media, 2012.

[18] N. Abdullah, M.A. Rahman, M.H.D. Othman, J. Jaafar, and A.F. Ismail, Membranes and Membrane Processes: Fundamentals, in Anonymous , Current Trends and Future Developments on (Bio-) Membranes, Elsevier, 2018, pp. 45-70.

[19] J. Mulder, Basic principles of membrane technology, , Springer Science & Business Media, 2012.

[20] E.M. Hoek, M. Elimelech. Cake-enhanced concentration polarization: a new fouling mechanism for salt-rejecting membranes. Environ.Sci.Technol., 37 (2003) 5581.

[21] J.H. Masliyah, S. Bhattacharjee, Electrokinetic and colloid transport phenomena, , John Wiley & Sons, 2006.

[22] M. Al Mamun, S. Bhattacharjee, D. Pernitsky, and M. Sadrzadeh. Colloidal fouling of nanofiltration membranes: Development of a standard operating procedure. Membranes, 7 (2017) 4.

[23] L. Rozelle, J. Cadotte, R. Corneliussen, E. Erickson, K. Cobian, and C. Kopp Jr. Phase inversion membranes. Encyclopedia of Separation Science, M.Mulder, Editor, Academic Press, NY, (2000) 3331.

[24] L.K. Wang, J.P. Chen, Y. Hung, and N.K. Shammas, Membrane and desalination technologies, , Springer, 2008.

[25] H. Strathmann, K. Kock. The formation mechanism of phase inversion membranes. Desalination, 21 (1977) 241.

[26] A. Asad, M. Sadrzadeh, and D. Sameoto. Direct Micropatterning of Phase Separation Membranes Using Hydrogel Soft Lithography. Advanced Materials Technologies, (2019) 1800384.

[27] A. Karkooti, A.Z. Yazdi, P. Chen, M. McGregor, N. Nazemifard, and M. Sadrzadeh. Development of advanced nanocomposite membranes using graphene nanoribbons and nanosheets for water treatment. J.Membr.Sci., (2018).

[28] J. Cadotte, R. Petersen, R. Larson, and E. Erickson. A new thin-film composite seawater reverse osmosis membrane. Desalination, 32 (1980) 25.

[29] W. Lau, A. Ismail, N. Misdan, and M. Kassim. A recent progress in thin film composite membrane: a review. Desalination, 287 (2012) 190.

[30] P.W. Morgan, S.L. Kwolek. Interfacial polycondensation. II. Fundamentals of polymer formation at liquid interfaces. Journal of Polymer Science, 40 (1959) 299.

[31] B. Khorshidi, T. Thundat, D. Pernitsky, and M. Sadrzadeh. A parametric study on the synergistic impacts of chemical additives on permeation properties of thin film composite polyamide membrane. J.Membr.Sci., 535 (2017) 248.

[32] B. Khorshidi, T. Thundat, B.A. Fleck, and M. Sadrzadeh. A novel approach toward fabrication of high performance thin film composite polyamide membranes. Scientific reports, 6 (2016) 22069.

[33] D. Rana, T. Matsuura. Surface modifications for antifouling membranes. Chem.Rev., 110 (2010) 2448.

[34] Z. Liu, X. An, C. Dong, S. Zheng, B. Mi, and Y. Hu. Modification of thin film composite polyamide membranes with 3D hyperbranched polyglycerol for simultaneous improvement in their filtration performance and antifouling properties. Journal of Materials Chemistry A, 5 (2017) 23190.

[35] M.F. Ismail, M.A. Islam, B. Khorshidi, and M. Sadrzadeh. Prediction of surface charge properties on the basis of contact angle titration models. Mater.Chem.Phys., 258 (2021) 123933.

[36] M.F. Ismail, B. Khorshidi, and M. Sadrzadeh. New insights into the impact of nanoscale surface heterogeneity on the wettability of polymeric membranes. J.Membr.Sci., 590 (2019) 117270.

[37] H. Yanagishita, D. Kitamoto, K. Haraya, T. Nakane, T. Okada, H. Matsuda, et al. Separation performance of polyimide composite membrane prepared by dip coating process. J.Membr.Sci., 188 (2001) 165.

[38] J. Cho, J. Le, Y. Na, M. Sadrzadeh, and A. Myles. Microscopic Characterization of IBM Star Polymers at High-Temperature for Water Membrane Applications. Microscopy and Microanalysis, 24 (2018) 1080.

[39] I. Goossens, A. Van Haute. The influence of mineral fillers on the membrane properties of high flux asymmetric cellulose acetate reverse osmosis membranes. Desalination, 18 (1976) 203.

[40] B. Khorshidi, J. Hajinasiri, G. Ma, S. Bhattacharjee, and M. Sadrzadeh. Thermally resistant and electrically conductive PES/ITO nanocomposite membrane. J.Membr.Sci., 500 (2016) 151.

[41] H. Yang, J. Hou, V. Chen, and Z. Xu. Surface and interface engineering for organic–inorganic composite membranes. Journal of Materials Chemistry A, 4 (2016) 9716.

[42] B. Khorshidi, S.A. Hosseini, G. Ma, M. McGregor, and M. Sadrzadeh. Novel nanocomposite polyethersulfone-antimony tin oxide membrane with enhanced thermal, electrical and antifouling properties. Polymer, 163 (2019) 48.

[43] D. Emadzadeh, W. Lau, and A. Ismail. Synthesis of thin film nanocomposite forward osmosis membrane with enhancement in water flux without sacrificing salt rejection. Desalination, 330 (2013) 90.

[44] Y. Wang, R. Ou, Q. Ge, H. Wang, and T. Xu. Preparation of polyethersulfone/carbon nanotube substrate for high-performance forward osmosis membrane. Desalination, 330 (2013) 70.

[45] O. Heinz, M. Aghajani, A.R. Greenberg, and Y. Ding. Surface-patterning of polymeric membranes: fabrication and performance. Current Opinion in Chemical Engineering, 20 (2018) 1.

[46] L. Vogelaar, J.N. Barsema, C.J. van Rijn, W. Nijdam, and M. Wessling. Phase separation micromolding—PSμM. Adv Mater, 15 (2003) 1385.

[47] G.R. Guillen, Y. Pan, M. Li, and E.M. Hoek. Preparation and characterization of membranes formed by nonsolvent induced phase separation: a review. Ind Eng Chem Res, 50 (2011) 3798.

[48] Y. Won, J. Lee, D. Choi, H.R. Chae, I. Kim, C. Lee, et al. Preparation and application of patterned membranes for wastewater treatment. Environ.Sci.Technol., 46 (2012) 11021.

[49] Y.K. Lee, Y. Won, J.H. Yoo, K.H. Ahn, and C. Lee. Flow analysis and fouling on the patterned membrane surface. J.Membr.Sci., 427 (2013) 320.

[50] A. Venault, Y. Chang, D. Wang, and D. Bouyer. A review on polymeric membranes and hydrogels prepared by vapor-induced phase separation process. Polymer Reviews, 53 (2013) 568.

[51] H. Matsuyama, M. Teramoto, R. Nakatani, and T. Maki. Membrane formation via phase separation induced by penetration of nonsolvent from vapor phase. II. Membrane morphology. J Appl Polym Sci, 74 (1999) 171.

[52] Y. Gençal, E. Durmaz, and P. Çulfaz-Emecen. Preparation of patterned microfiltration membranes and their performance in crossflow yeast filtration. J.Membr.Sci., 476 (2015) 224.

[53] S.H. Maruf, L. Wang, A.R. Greenberg, J. Pellegrino, and Y. Ding. Use of nanoimprinted surface patterns to mitigate colloidal deposition on ultrafiltration membranes. J.Membr.Sci., 428 (2013) 598.

[54] S.H. Maruf, M. Rickman, L. Wang, J. Mersch IV, A.R. Greenberg, J. Pellegrino, et al. Influence of sub-micron surface patterns on the deposition of model proteins during active filtration. J.Membr.Sci., 444 (2013) 420.

[55] B. Khorshidi, I. Biswas, T. Ghosh, T. Thundat, and M. Sadrzadeh. Robust fabrication of thin film polyamide-TiO 2 nanocomposite membranes with enhanced thermal stability and anti-biofouling propensity. Scientific reports, 8 (2018) 784.

[56] Z. Almansoori, B. Khorshidi, B. Sadri, and M. Sadrzadeh. Parametric study on the stabilization of metal oxide nanoparticles in organic solvents: A case study with indium tin oxide (ITO) and heptane. Ultrason.Sonochem., 40 (2018) 1003.

[57] Y. Manawi, V. Kochkodan, E. Mahmoudi, D.J. Johnson, A.W. Mohammad, and M.A. Atieh. Characterization and Separation Performance of a Novel Polyethersulfone Membrane Blended with Acacia Gum. Scientific reports, 7 (2017) 15831.

[58] W. Sun, J. Liu, H. Chu, and B. Dong. Pretreatment and membrane hydrophilic modification to reduce membrane fouling. Membranes, 3 (2013) 226.

[59] M. Amirilargani, M. Sadrzadeh, E. Sudhölter, and L. de Smet. Surface modification methods of organic solvent nanofiltration membranes. Chem.Eng.J., 289 (2016) 562.

[60] C. Zhao, J. Xue, F. Ran, and S. Sun. Modification of polyethersulfone membranes–a review of methods. Progress in Materials Science, 58 (2013) 76.

[61] G. Kang, Y. Cao. Development of antifouling reverse osmosis membranes for water treatment: a review. Water Res., 46 (2012) 584.

[62] M. Bikel, I.G. Punt, R.G. Lammertink, and M. Wessling. Micropatterned polymer films by vapor-induced phase separation using permeable molds. ACS applied materials & interfaces, 1 (2009) 2856.

[63] Y. GENÇAL. Fabrication and Characterization of Corrugated Microfiltration Membranes. Middle East Technical University, (2014).

[64] Y. Gençal, E. Durmaz, and P. Çulfaz-Emecen. Preparation of patterned microfiltration membranes and their performance in crossflow yeast filtration. J.Membr.Sci., 476 (2015) 224.

[65] M. Girones, I. Akbarsyah, W. Nijdam, C. Van Rijn, H. Jansen, R. Lammertink, et al. Polymeric microsieves produced by phase separation micromolding. J.Membr.Sci., 283 (2006) 411.

[66] Y. Won, D. Choi, J.H. Jang, J. Lee, H.R. Chae, I. Kim, et al. Factors affecting pattern fidelity and performance of a patterned membrane. J.Membr.Sci., 462 (2014) 1.

[67] M. Bikel, P.Z. Culfaz, L. Bolhuis-Versteeg, J.G. Pérez, R. Lammertink, and M. Wessling. Polymeric microsieves via phase separation microfabrication: Process and design optimization. J.Membr.Sci., 347 (2010) 93.

[68] E.M. Ahmed. Hydrogel: Preparation, characterization, and applications: A review. Journal of Advanced Research, 6 (2015) 105.

[69] K.Y. Lee, D.J. Mooney. Hydrogels for tissue engineering. Chem.Rev., 101 (2001) 1869.

[70] M.W. Tibbitt, K.S. Anseth. Hydrogels as extracellular matrix mimics for 3D cell culture. Biotechnol.Bioeng., 103 (2009) 655.

[71] N. Peppas, P. Bures, W. Leobandung, and H. Ichikawa. Hydrogels in pharmaceutical formulations. European journal of pharmaceutics and biopharmaceutics, 50 (2000) 27.

[72] A.S. Hoffman. Hydrogels for biomedical applications. Adv.Drug Deliv.Rev., 64 (2012) 18.

[73] M. Sadrzadeh, S. Bhattacharjee. Rational design of phase inversion membranes by tailoring thermodynamics and kinetics of casting solution using polymer additives. J.Membr.Sci., 441 (2013) 31.

[74] K.A. Gebru, C. Das. Effects of solubility parameter differences among PEG, PVP and CA on the preparation of ultrafiltration membranes: Impacts of solvents and additives on morphology, permeability and fouling performances. Chin.J.Chem.Eng., 25 (2017) 911.

[75] W. Barthlott, C. Neinhuis. Purity of the sacred lotus, or escape from contamination in biological surfaces. Planta, 202 (1997) 1.

[76] T. Wong, S.H. Kang, S.K. Tang, E.J. Smythe, B.D. Hatton, A. Grinthal, et al. Bioinspired self-repairing slippery surfaces with pressure-stable omniphobicity. Nature, 477 (2011) 443.

[77] X. Gao, L. Jiang. Biophysics: water-repellent legs of water striders. Nature, 432 (2004) 36.

[78] C.M. Magin, S.P. Cooper, and A.B. Brennan. Non-toxic antifouling strategies. Materials today, 13 (2010) 36.

[79] D. Xia, L.M. Johnson, and G.P. López. Anisotropic Wetting Surfaces with One-Dimesional and Directional Structures: Fabrication Approaches, Wetting Properties and Potential Applications. Adv Mater, 24 (2012) 1287.

[80] P. Radovanovic, S.W. Thiel, and S. Hwang. Formation of asymmetric polysulfone membranes by immersion precipitation. Part I. Modelling mass transport during gelation. J.Membr.Sci., 65 (1992) 213.

[81] J. Wijmans, J. Baaij, and C. Smolders. The mechanism of formation of microporous or skinned membranes produced by immersion precipitation. J.Membr.Sci., 14 (1983) 263.

[82] H. Strathmann, K. Kock, P. Amar, and R. Baker. The formation mechanism of asymmetric membranes. Desalination, 16 (1975) 179.

[83] D.J. Miller, S. Kasemset, D.R. Paul, and B.D. Freeman. Comparison of membrane fouling at constant flux and constant transmembrane pressure conditions. J.Membr.Sci., 454 (2014) 505.

[84] C. Zhou, Z. Hou, X. Lu, Z. Liu, X. Bian, L. Shi, et al. Effect of polyethersulfone molecular weight on structure and performance of ultrafiltration membranes. Ind Eng Chem Res, 49 (2010) 9988.

[85] K. Boussu, C. Vandecasteele, and B. Van der Bruggen. Study of the characteristics and the performance of self-made nanoporous polyethersulfone membranes. Polymer, 47 (2006) 3464.

[86] M.A.A. Shahmirzadi, S.S. Hosseini, G. Ruan, and N. Tan. Tailoring PES nanofiltration membranes through systematic investigations of prominent design, fabrication and operational parameters. RSC Advances, 5 (2015) 49080.

[87] B. Amsden. Solute diffusion in hydrogels.: an examination of the retardation effect. Polym.Gels Networks, 6 (1998) 13.

[88] E.J. Schantz, M.A. Lauffer. Diffusion measurements in agar gel. Biochemistry (N.Y.), 1 (1962) 658.

[89] J.H. Jang, J. Lee, S. Jung, D. Choi, Y. Won, K.H. Ahn, et al. Correlation between particle deposition and the size ratio of particles to patterns in nano-and micro-patterned membrane filtration systems. Separation and Purification Technology, 156 (2015) 608.

[90] D. Choi, S. Jung, Y. Won, J.H. Jang, J. Lee, H. Chae, et al. Effect of Pattern Shape on the Initial Deposition of Particles in the Aqueous Phase on Patterned Membranes during Crossflow Filtration. Environmental Science & Technology Letters, 4 (2017) 66.

[91] I.S. Ngene, R.G. Lammertink, M. Wessling, and Van der Meer, Walter GJ. Particle deposition and biofilm formation on microstructured membranes. J.Membr.Sci., 364 (2010) 43.

[92] W. Lau, l.R. Pérez de. Membrane Separation. Chem.Eng.Technol., 41 (2018) 210.

[93] P. Karami, B. Khorshidi, M. McGregor, J.T. Peichel, J. Soares, and M. Sadrzadeh. Thermally stable Thin Film Composite Polymeric Membranes for Water Treatment: A Review. J.Clean.Prod., (2019) 119447.

[94] S. Alzahrani, A.W. Mohammad. Challenges and trends in membrane technology implementation for produced water treatment: A review. Journal of Water Process Engineering, 4 (2014) 107.

[95] A. Fane. Membranes and the water cycle: challenges and opportunities. Applied water science, 1 (2011) 3.

[96] W. Guo, H. Ngo, and J. Li. A mini-review on membrane fouling. Bioresour.Technol., 122 (2012) 27.

[97] W. Gao, H. Liang, J. Ma, M. Han, Z. Chen, Z. Han, et al. Membrane fouling control in ultrafiltration technology for drinking water production: a review. Desalination, 272 (2011) 1.

[98] A.P. Straub, A. Deshmukh, and M. Elimelech. Pressure-retarded osmosis for power generation from salinity gradients: is it viable? Energy & Environmental Science, 9 (2016) 31.

[99] H.B. Park, J. Kamcev, L.M. Robeson, M. Elimelech, and B.D. Freeman. Maximizing the right stuff: The trade-off between membrane permeability and selectivity. Science, 356 (2017) 10.1126/science.aab0530.

[100] Y. Qin, H. Yang, Z. Xu, and F. Li. Surface Modification of Polyacrylonitrile Membrane by Chemical Reaction and Physical Coating: Comparison between Static and Pore-Flowing Procedures. ACS Omega, 3 (2018) 4231.

[101] M.S. Mauter, Y. Wang, K.C. Okemgbo, C.O. Osuji, E.P. Giannelis, and M. Elimelech. Antifouling ultrafiltration membranes via post-fabrication grafting of biocidal nanomaterials. ACS applied materials & interfaces, 3 (2011) 2861.

[102] M. Rastgar, A. Bozorg, and A. Shakeri. Novel dimensionally controlled nanopore forming template in forward osmosis membranes. Environ.Sci.Technol., 52 (2018) 2704.

[103] Y.T. Nam, J. Choi, K.M. Kang, D.W. Kim, and H. Jung. Enhanced stability of laminated graphene oxide membranes for nanofiltration via interstitial amide bonding. ACS applied materials & interfaces, 8 (2016) 27376.

[104] A. Asad, D. Sameoto, and M. Sadrzadeh. Overview of membrane technology. Nanocomposite Membranes for Water and Gas Separation, (2019) 1.

[105] O. Heinz, M. Aghajani, A.R. Greenberg, and Y. Ding. Surface-patterning of polymeric membranes: fabrication and performance. Current opinion in chemical engineering, 20 (2018) 1.

[106] N.U. Barambu, M.R. Bilad, Y. Wibisono, J. Jaafar, T.M.I. Mahlia, and A.L. Khan. Membrane Surface Patterning as a Fouling Mitigation Strategy in Liquid Filtration: A Review. Polymers, 11 (2019) 1687.

[107] I.M. ElSherbiny, A.S. Khalil, and M. Ulbricht. Surface micro-patterning as a promising platform towards novel polyamide thin-film composite membranes of superior performance. J.Membr.Sci., 529 (2017) 11.

[108] Y. Won, S. Jung, J. Jang, J. Lee, H. Chae, D. Choi, et al. Correlation of membrane fouling with topography of patterned membranes for water treatment. J.Membr.Sci., 498 (2016) 14.

[109] L. Vogelaar, R.G. Lammertink, J.N. Barsema, W. Nijdam, L.A. Bolhuis-Versteeg, C.J. Van Rijn, et al. Phase separation micromolding: a new generic approach for microstructuring various materials. Small, 1 (2005) 645.

[110] J. Seo, D.I. Kushner, and M.A. Hickner. 3D printing of micropatterned anion exchange membranes. ACS applied materials & interfaces, 8 (2016) 16656.

[111] S.H. Maruf, A.R. Greenberg, J. Pellegrino, and Y. Ding. Critical flux of surface-patterned ultrafiltration membranes during cross-flow filtration of colloidal particles. J.Membr.Sci., 471 (2014) 65.

[112] S.H. Maruf, L. Wang, A.R. Greenberg, J. Pellegrino, and Y. Ding. Use of nanoimprinted surface patterns to mitigate colloidal deposition on ultrafiltration membranes. J.Membr.Sci., 428 (2013) 598.

[113] A.M. Koupaei, H. Nazaripoor, and M. Sadrzadeh. Electrohydrodynamic Patterning of Polyethersulfone Membranes. Langmuir, 35 (2019) 12139.

[114] M. Bikel, I.G. Punt, R.G. Lammertink, and M. Wessling. Micropatterned polymer films by vapor-induced phase separation using permeable molds. ACS applied materials & interfaces, 1 (2009) 2856.

[115] S.H. Maruf. Surface patterning of polymeric separation membranes and its influence on the filtration performance. (2014).

[116] T. Femmer, A.J. Kuehne, J. Torres-Rendon, A. Walther, and M. Wessling. Print your membrane: Rapid prototyping of complex 3D-PDMS membranes via a sacrificial resist. J.Membr.Sci., 478 (2015) 12.

[117] S.H. Maruf, Z. Li, J.A. Yoshimura, J. Xiao, A.R. Greenberg, and Y. Ding. Influence of nanoimprint lithography on membrane structure and performance. Polymer, 69 (2015) 129.

[118] M. Mayer, J. Yang, I. Gitlin, D.H. Gracias, and G.M. Whitesides. Micropatterned agarose gels for stamping arrays of proteins and gradients of proteins. Proteomics, 4 (2004) 2366.

[119] Y. Qiu, K. Park. Environment-sensitive hydrogels for drug delivery. Adv.Drug Deliv.Rev., 53 (2001) 321.

[120] J. Mulder, Basic principles of membrane technology, , Springer Science & Business Media, 2012.

[121] G.R. Guillen, Y. Pan, M. Li, and E.M. Hoek. Preparation and characterization of membranes formed by nonsolvent induced phase separation: a review. Ind Eng Chem Res, 50 (2011) 3798.

[122] M. Sadrzadeh, S. Bhattacharjee. Rational design of phase inversion membranes by tailoring thermodynamics and kinetics of casting solution using polymer additives. J.Membr.Sci., 441 (2013) 31.

[123] F. Van Vught, W.F.C. Kools, and B. te Hoogstraten. Membrane formation by phase inversion in multicomponent polymer system, (1998).

[124] H. Yang, K. Liao, H. Huang, Q. Wu, L. Wan, and Z. Xu. Mussel-inspired modification of a polymer membrane for ultra-high water permeability and oil-in-water emulsion separation. Journal of Materials Chemistry A, 2 (2014) 10225.

[125] M. Padaki, R.S. Murali, M.S. Abdullah, N. Misdan, A. Moslehyani, M. Kassim, et al. Membrane technology enhancement in oil–water separation. A review. Desalination, 357 (2015) 197.

[126] R. Sarbatly, D. Krishnaiah, and Z. Kamin. A review of polymer nanofibres by electrospinning and their application in oil–water separation for cleaning up marine oil spills. Mar.Pollut.Bull., 106 (2016) 8.

[127] M. Rastgar, A. Shakeri, A. Karkooti, A. Asad, R. Razavi, and M. Sadrzadeh. Removal of trace organic contaminants by melamine-tuned highly cross-linked polyamide TFC membranes. Chemosphere, 238 (2020) 124691.

[128] J. Zhang, X. Pan, Q. Xue, D. He, L. Zhu, and Q. Guo. Antifouling hydrolyzed polyacrylonitrile/graphene oxide membrane with spindle-knotted structure for highly effective separation of oil-water emulsion. J.Membr.Sci., 532 (2017) 38.

[129] Y. Huang, H. Zhan, D. Li, H. Tian, and C. Chang. Tunicate cellulose nanocrystals modified commercial filter paper for efficient oil/water separation. J.Membr.Sci., 591 (2019) 117362.

[130] M.E. Comba, K.L. Kaiser. Suspended particulate concentrations in the St. Lawrence River (1985–1987) determined by centrifugation and filtration. Sci.Total Environ., 97 (1990) 191.

[131] Y. Suzuki, T. Maruyama. Removal of emulsified oil from water by coagulation and foam separation. Sep.Sci.Technol., 40 (2005) 3407.

[132] W. Kang, L. Guo, H. Fan, L. Meng, and Y. Li. Flocculation, coalescence and migration of dispersed phase droplets and oil–water separation in heavy oil emulsion. Journal of Petroleum Science and Engineering, 81 (2012) 177.

[133] S. Zarghami, T. Mohammadi, M. Sadrzadeh, and B. Van der Bruggen. Superhydrophilic and underwater superoleophobic membranes-A review of synthesis methods. Progress in Polymer Science, (2019) 101166.

[134] N. Helali, M. Rastgar, M.F. Ismail, and M. Sadrzadeh. Development of underwater superoleophobic polyamide-imide (PAI) microfiltration membranes for oil/water emulsion separation. Separation and Purification Technology, 238 (2020) 116451.

[135] J. Zhang, Q. Xue, X. Pan, Y. Jin, W. Lu, D. Ding, et al. Graphene oxide/polyacrylonitrile fiber hierarchical-structured membrane for ultra-fast microfiltration of oil-water emulsion. Chem.Eng.J., 307 (2017) 643.

[136] K. Dalane, Z. Dai, G. Mogseth, M. Hillestad, and L. Deng. Potential applications of membrane separation for subsea natural gas processing: A review. Journal of Natural Gas Science and Engineering, 39 (2017) 101.

[137] H. Shi, Y. He, Y. Pan, H. Di, G. Zeng, L. Zhang, et al. A modified mussel-inspired method to fabricate TiO2 decorated superhydrophilic PVDF membrane for oil/water separation. J.Membr.Sci., 506 (2016) 60.

[138] C. de Morais Coutinho, M.C. Chiu, R.C. Basso, A.P.B. Ribeiro, L.A.G. Gonçalves, and L.A. Viotto. State of art of the application of membrane technology to vegetable oils: A review. Food Res.Int., 42 (2009) 536.

[139] H. Li, Y. Yin, L. Zhu, Y. Xiong, X. Li, T. Guo, et al. A hierarchical structured steel mesh decorated with metal organic framework/graphene oxide for high-efficient oil/water separation. J.Hazard.Mater., 373 (2019) 725.

[140] D. Li, X. Huang, Y. Huang, J. Yuan, D. Huang, G.J. Cheng, et al. Additive printed all-cellulose membranes with hierarchical structure for highly efficient separation of oil/water nanoemulsions. ACS Applied Materials & Interfaces, 11 (2019) 44375.

[141] J. Ge, J. Zhang, F. Wang, Z. Li, J. Yu, and B. Ding. Superhydrophilic and underwater superoleophobic nanofibrous membrane with hierarchical structured skin for effective oil-in-water emulsion separation. Journal of Materials Chemistry A, 5 (2017) 497.

[142] A.K. Kota, G. Kwon, W. Choi, J.M. Mabry, and A. Tuteja. Hygro-responsive membranes for effective oilâ€“water separation. Nature communications, 3 (2012) 1.

[143] D. Qian, D. Chen, N. Li, Q. Xu, H. Li, J. He, et al. TiO2/sulfonated graphene oxide/Ag nanoparticle membrane: In situ separation and photodegradation of oil/water emulsions. J.Membr.Sci., 554 (2018) 16.

[144] A. Karkooti, A.Z. Yazdi, P. Chen, M. McGregor, N. Nazemifard, and M. Sadrzadeh. Development of advanced nanocomposite membranes using graphene nanoribbons and nanosheets for water treatment. J.Membr.Sci., 560 (2018) 97.

[145] A. Karkooti, A.Z. Yazdi, P. Chen, M. McGregor, N. Nazemifard, and M. Sadrzadeh. Development of advanced nanocomposite membranes using graphene nanoribbons and nanosheets for water treatment. J.Membr.Sci., 560 (2018) 97.

[146] B. Van der Bruggen. Chemical modification of polyethersulfone nanofiltration membranes: a review. J Appl Polym Sci, 114 (2009) 630.

[147] L. Zhu, B. Zhu, L. Xu, Y. Feng, F. Liu, and Y. Xu. Corona-induced graft polymerization for surface modification of porous polyethersulfone membranes. Appl.Surf.Sci., 253 (2007) 6052.

[148] D. Yu, W. Lin, and M. Yang. Surface modification of poly (L-lactic acid) membrane via layer-by-layer assembly of silver nanoparticle-embedded polyelectrolyte multilayer. Bioconjug.Chem., 18 (2007) 1521.

[149] C. Liu, P. Su, C. Hu, J. Lai, and Y. Liu. Surface modification of porous substrates for oil/water separation using crosslinkable polybenzoxazine as an agent. J.Membr.Sci., 546 (2018) 100.

[150] A. Asad, M. Rastgar, H. Nazaripoor, M. Sadrzadeh, and D. Sameoto. Durability and Recoverability of Soft Lithographically Patterned Hydrogel Molds for the Formation of Phase Separation Membranes. Micromachines, 11 (2020) 108.

[151] L. Vogelaar, R.G. Lammertink, J.N. Barsema, W. Nijdam, L.A. Bolhuis-Versteeg, C.J. Van Rijn, et al. Phase separation micromolding: a new generic approach for microstructuring various materials. Small, 1 (2005) 645.

[152] A. Asad, D. Sameoto, and M. Sadrzadeh, Overview of membrane technology, in Anonymous , Nanocomposite Membranes for Water and Gas Separation, Elsevier, 2020, pp. 1-28.

[153] A. Shakeri, H. Salehi, and M. Rastgar. Chitosan-based thin active layer membrane for forward osmosis desalination. Carbohydr.Polym., 174 (2017) 658.

[154] M.A.H. Khondoker, N. Baheri, and D. Sameoto. Tendon-driven functionally gradient soft robotic gripper 3D printed with intermixed extrudate of hard and soft thermoplastics. 3D Printing and Additive Manufacturing, 6 (2019) 191.

[155] A. Rabbani, S. Salehi. Dynamic modeling of the formation damage and mud cake deposition using filtration theories coupled with SEM image processing. Journal of Natural Gas Science and Engineering, 42 (2017) 157.

[156] N. Otsu. A threshold selection method from gray-level histograms. IEEE Trans.Syst.Man Cybern., 9 (1979) 62.

[157] A. Rabbani, S. Ayatollahi, R. Kharrat, and N. Dashti. Estimation of 3-D pore network coordination number of rocks from watershed segmentation of a single 2-D image. Adv.Water Resour., 94 (2016) 264.

[158] Y. Zhang, R. Wang, L. Zhang, and A.G. Fane. Novel single-step hydrophobic modification of polymeric hollow fiber membranes containing imide groups: Its potential for membrane contactor application. Separation and purification technology, 101 (2012) 76.

[159] H. Kim, R. Tyagi, A. Fouda, and K. Ionasson. The kinetic study for asymmetric membrane formation via phase-inversion process. J Appl Polym Sci, 62 (1996) 621.

[160] H. Basri, A.F. Ismail, and M. Aziz. Polyethersulfone (PES)–silver composite UF membrane: Effect of silver loading and PVP molecular weight on membrane morphology and antibacterial activity. Desalination, 273 (2011) 72.

[161] S. Zhao, P. Wang, C. Wang, J.L. Langer, G. Abulikemu, and X. Sun. Recycling of high temperature steam condensed water from petroleum refinery by thermostable PPESK ultrafiltration membrane. Chem.Eng.J., 219 (2013) 419.

[162] R.N. Wenzel. Surface roughness and contact angle. J.Phys.Chem., 53 (1949) 1466.

[163] Y. Wei, H. Qi, X. Gong, and S. Zhao. Specially wettable membranes for oil–water separation. Advanced Materials Interfaces, 5 (2018) 1800576.

[164] X. Zhao, Y. Su, Y. Liu, Y. Li, and Z. Jiang. Free-standing graphene oxide-palygorskite nanohybrid membrane for oil/water separation. ACS Applied Materials & Interfaces, 8 (2016) 8247.

[165] V. Chen, A. Fane, S. Madaeni, and I. Wenten. Particle deposition during membrane filtration of colloids: transition between concentration polarization and cake formation. J.Membr.Sci., 125 (1997) 109.

[166] M.F. Ismail, B. Khorshidi, and M. Sadrzadeh. New insights into the impact of nanoscale surface heterogeneity on the wettability of polymeric membranes. J.Membr.Sci., 590 (2019) 117270.

[167] S. Kumar, C. Guria, and A. Mandal. Synthesis, characterization and performance studies of polysulfone/bentonite nanoparticles mixed-matrix ultra-filtration membranes using oil field produced water. Separation and Purification Technology, 150 (2015) 145.

[168] R.J. Gohari, F. Korminouri, W. Lau, A. Ismail, T. Matsuura, M. Chowdhury, et al. A novel super-hydrophilic PSf/HAO nanocomposite ultrafiltration membrane for efficient separation of oil/water emulsion. Separation and purification technology, 150 (2015) 13.

[169] T. Rajasekhar, M. Trinadh, P.V. Babu, A.V.S. Sainath, and A. Reddy. Oil–water emulsion separation using ultrafiltration membranes based on novel blends of poly (vinylidene fluoride)

and amphiphilic tri-block copolymer containing carboxylic acid functional group. J.Membr.Sci., 481 (2015) 82.

[170] G. Zhang, J. Jiang, Q. Zhang, F. Gao, X. Zhan, and F. Chen. Ultralow oil-fouling heterogeneous poly (ether sulfone) ultrafiltration membrane via blending with novel amphiphilic fluorinated gradient copolymers. Langmuir, 32 (2016) 1380.

[171] W. Chen, J. Peng, Y. Su, L. Zheng, L. Wang, and Z. Jiang. Separation of oil/water emulsion using Pluronic F127 modified polyethersulfone ultrafiltration membranes. Separation and Purification Technology, 66 (2009) 591.

[172] T. Yuan, J. Meng, T. Hao, Y. Zhang, and M. Xu. Polysulfone membranes clicked with poly (ethylene glycol) of high density and uniformity for oil/water emulsion purification: effects of tethered hydrogel microstructure. J.Membr.Sci., 470 (2014) 112.

[173] X. Huang, W. Wang, Y. Liu, H. Wang, Z. Zhang, W. Fan, et al. Treatment of oily waste water by PVP grafted PVDF ultrafiltration membranes. Chem.Eng.J., 273 (2015) 421.

[174] V. Moghimifar, A. Raisi, and A. Aroujalian. Surface modification of polyethersulfone ultrafiltration membranes by corona plasma-assisted coating TiO2 nanoparticles. J.Membr.Sci., 461 (2014) 69.

[175] J. Yin, J. Zhou. Novel polyethersulfone hybrid ultrafiltration membrane prepared with SiO2-g-(PDMAEMA-co-PDMAPS) and its antifouling performances in oil-in-water emulsion application. Desalination, 365 (2015) 46.

[176] X. Yang, Y. He, G. Zeng, Y. Zhan, Y. Pan, H. Shi, et al. Novel hydrophilic PVDF ultrafiltration membranes based on a ZrO 2–multiwalled carbon nanotube hybrid for oil/water separation. J.Mater.Sci., 51 (2016) 8965.

[177] J.B. Melbiah, D. Nithya, and D. Mohan. Surface modification of polyacrylonitrile ultrafiltration membranes using amphiphilic Pluronic F127/CaCO3 nanoparticles for oil/water emulsion separation. Colloids Surf.Physicochem.Eng.Aspects, 516 (2017) 147.

[178] Y. Zhang, X. Shan, Z. Jin, and Y. Wang. Synthesis of sulfated Y-doped zirconia particles and effect on properties of polysulfone membranes for treatment of wastewater containing oil. J.Hazard.Mater., 192 (2011) 559.

[179] A. Salahi, A. Gheshlaghi, T. Mohammadi, and S.S. Madaeni. Experimental performance evaluation of polymeric membranes for treatment of an industrial oily wastewater. Desalination, 262 (2010) 235.

[180] I. Sadeghi, A. Aroujalian, A. Raisi, B. Dabir, and M. Fathizadeh. Surface modification of polyethersulfone ultrafiltration membranes by corona air plasma for separation of oil/water emulsions. J.Membr.Sci., 430 (2013) 24.

[181] M. Liu, L. Tie, J. Li, Y. Hou, and Z. Guo. Underoil superhydrophilic surfaces: water adsorption in metal–organic frameworks. Journal of Materials Chemistry A, 6 (2018) 1692.

[182] H. Yang, K. Liao, H. Huang, Q. Wu, L. Wan, and Z. Xu. Mussel-inspired modification of a polymer membrane for ultra-high water permeability and oil-in-water emulsion separation. Journal of Materials Chemistry A, 2 (2014) 10225.

[183] M.M. Mekonnen, A.Y. Hoekstra. Four billion people facing severe water scarcity. Science advances, 2 (2016) e1500323.

[184] Y. Shevah, Water resources, water scarcity challenges, and perspectives, in Anonymous , Water Challenges and Solutions on a Global Scale, ACS Publications, 2015, pp. 185-219.

[185] C.Y. Tang, Z. Yang, H. Guo, J.J. Wen, L.D. Nghiem, and E. Cornelissen. Potable water reuse through advanced membrane technology, (2018).

[186] X. Cao, Y. Yan, F. Zhou, and S. Sun. Tailoring nanofiltration membranes for effective removing dye intermediates in complex dye-wastewater. J.Membr.Sci., 595 (2020) 117476.

[187] M. Hayatbakhsh, M. Sadrzadeh, D. Pernitsky, S. Bhattacharjee, and J. Hajinasiri. Treatment of an in situ oil sands produced water by polymeric membranes. Desalination and water treatment, 57 (2016) 14869.

[188] A. Asad, M. Rastgar, D. Sameoto, and M. Sadrzadeh. Gravity assisted super high flux microfiltration polyamide-imide membranes for oil/water emulsion separation. J.Membr.Sci., (2020) 119019.

[189] M.G. Elshof, E. Maaskant, M.A. Hempenius, and N.E. Benes. Poly (aryl cyanurate)-Based Thin-Film Composite Nanofiltration Membranes. ACS applied polymer materials, 3 (2021) 2385.

[190] S.S. Wadekar, Y. Wang, O.R. Lokare, and R.D. Vidic. Influence of chemical cleaning on physicochemical characteristics and ion rejection by thin film composite nanofiltration membranes. Environ.Sci.Technol., 53 (2019) 10166.

[191] S.F. Seyedpour, M. Dadashi Firouzjaei, A. Rahimpour, E. Zolghadr, A. Arabi Shamsabadi, P. Das, et al. Toward Sustainable Tackling of Biofouling Implications and Improved Performance of TFC FO Membranes Modified by Ag-MOF Nanorods. ACS Applied Materials & Interfaces, 12 (2020) 38285.

[192] B. Khorshidi, A. Bhinder, T. Thundat, D. Pernitsky, and M. Sadrzadeh. Developing high throughput thin film composite polyamide membranes for forward osmosis treatment of SAGD produced water. J.Membr.Sci., 511 (2016) 29.

[193] Z. Yang, H. Guo, and C.Y. Tang. The upper bound of thin-film composite (TFC) polyamide membranes for desalination. J.Membr.Sci., 590 (2019) 117297.

[194] Z. Yang, Y. Zhou, Z. Feng, X. Rui, T. Zhang, and Z. Zhang. A review on reverse osmosis and nanofiltration membranes for water purification. Polymers, 11 (2019) 1252.

[195] B. Khorshidi, T. Thundat, B. Fleck, and M. Sadrzadeh. Thin film composite polyamide membranes: parametric study on the influence of synthesis conditions. RSC Advances, 5 (2015) 54985.

[196] J. Zhao, Y. Su, X. He, X. Zhao, Y. Li, R. Zhang, et al. Dopamine composite nanofiltration membranes prepared by self-polymerization and interfacial polymerization. J.Membr.Sci., 465 (2014) 41.

[197] M. Li, J. Xu, C. Chang, C. Feng, L. Zhang, Y. Tang, et al. Bioinspired fabrication of composite nanofiltration membrane based on the formation of DA/PEI layer followed by cross-linking. J.Membr.Sci., 459 (2014) 62.

[198] X. Li, L. Zhu, J. Jiang, Z. Yi, B. Zhu, and Y. Xu. Hydrophilic nanofiltration membranes with self-polymerized and strongly-adhered polydopamine as separating layer. Chinese Journal of Polymer Science, 30 (2012) 152.

[199] R. Zhang, Y. Su, X. Zhao, Y. Li, J. Zhao, and Z. Jiang. A novel positively charged composite nanofiltration membrane prepared by bio-inspired adhesion of polydopamine and surface grafting of poly (ethylene imine). J.Membr.Sci., 470 (2014) 9.

[200] Y. Li, Y. Su, J. Li, X. Zhao, R. Zhang, X. Fan, et al. Preparation of thin film composite nanofiltration membrane with improved structural stability through the mediation of polydopamine. J.Membr.Sci., 476 (2015) 10.

[201] Y. Lv, H. Yang, H. Liang, L. Wan, and Z. Xu. Nanofiltration membranes via co-deposition of polydopamine/polyethylenimine followed by cross-linking. J.Membr.Sci., 476 (2015) 50.

[202] P. Gorgojo, M. Jimenez-Solomon, and A. Livingston. Polyamide thin film composite membranes on cross-linked polyimide supports: Improvement of RO performance via activating solvent. Desalination, 344 (2014) 181.

[203] M.G. Shin, J.Y. Seo, H. Park, Y. Park, and J. Lee. Overcoming the permeability-selectivity trade-off of desalination membranes via controlled solvent activation. J.Membr.Sci., 620 (2021) 118870.

[204] Y.H. Kotp. High-flux TFN nanofiltration membranes incorporated with Camphor-Al2O3 nanoparticles for brackish water desalination. Chemosphere, 265 (2021) 128999.

[205] B. Khorshidi, I. Biswas, T. Ghosh, T. Thundat, and M. Sadrzadeh. Robust fabrication of thin film polyamide-TiO 2 nanocomposite membranes with enhanced thermal stability and anti-biofouling propensity. Scientific reports, 8 (2018) 1.

[206] Z. Yang, Y. Wu, J. Wang, B. Cao, and C.Y. Tang. In situ reduction of silver by polydopamine: a novel antimicrobial modification of a thin-film composite polyamide membrane. Environ.Sci.Technol., 50 (2016) 9543.

[207] A. Asad, M. Rastgar, D. Sameoto, and M. Sadrzadeh. Gravity assisted super high flux microfiltration polyamide-imide membranes for oil/water emulsion separation. J.Membr.Sci., (2020) 119019.

[208] X. Wang, X. Li. Modeling of the initial deposition of individual particles during the cross-flow membrane filtration. Colloids Surf.Physicochem.Eng.Aspects, 440 (2014) 91.

[209] L. Vogelaar, R.G. Lammertink, J.N. Barsema, W. Nijdam, L.A. Bolhuis-Versteeg, C.J. Van Rijn, et al. Phase separation micromolding: a new generic approach for microstructuring various materials. Small, 1 (2005) 645.

[210] A. Asad, D. Sameoto, and M. Sadrzadeh. New generation of patterned membranes for water treatment.

[211] W. Choi, C. Lee, D. Lee, Y.J. Won, G.W. Lee, M.G. Shin, et al. Sharkskin-mimetic desalination membranes with ultralow biofouling. Journal of Materials Chemistry A, 6 (2018) 23034.

[212] I.M. ElSherbiny, A.S. Khalil, and M. Ulbricht. Surface micro-patterning as a promising platform towards novel polyamide thin-film composite membranes of superior performance. J.Membr.Sci., 529 (2017) 11.

[213] S.H. Maruf, A.R. Greenberg, J. Pellegrino, and Y. Ding. Fabrication and characterization of a surface-patterned thin film composite membrane. J.Membr.Sci., 452 (2014) 11.

[214] S.H. Maruf, A.R. Greenberg, and Y. Ding. Influence of substrate processing and interfacial polymerization conditions on the surface topography and permselective properties of surface-patterned thin-film composite membranes. J.Membr.Sci., 512 (2016) 50.

[215] Y. Mo, A. Tiraferri, N.Y. Yip, A. Adout, X. Huang, and M. Elimelech. Improved antifouling properties of polyamide nanofiltration membranes by reducing the density of surface carboxyl groups. Environ.Sci.Technol., 46 (2012) 13253.

[216] Y. Liang, Y. Zhu, C. Liu, K. Lee, W. Hung, Z. Wang, et al. Polyamide nanofiltration membrane with highly uniform sub-nanometre pores for sub-1 Å precision separation. Nature communications, 11 (2020) 1.

[217] W. Xie, G.M. Geise, B.D. Freeman, H. Lee, G. Byun, and J.E. McGrath. Polyamide interfacial composite membranes prepared from m-phenylene diamine, trimesoyl chloride and a new disulfonated diamine. J.Membr.Sci., 403 (2012) 152.

[218] P. Karami, B. Khorshidi, L. Shamaei, E. Beaulieu, J.B. Soares, and M. Sadrzadeh. Nanodiamond-Enabled Thin-Film Nanocomposite Polyamide Membranes for High-Temperature Water Treatment. ACS Applied Materials & Interfaces, 12 (2020) 53274.

[219] X. Ma, Z. Yao, Z. Yang, H. Guo, Z. Xu, C.Y. Tang, et al. Nanofoaming of polyamide desalination membranes to tune permeability and selectivity. Environmental Science & Technology Letters, 5 (2018) 123.

[220] X. Zhu, Z. Yang, Z. Gan, X. Cheng, X. Tang, X. Luo, et al. Toward tailoring nanofiltration performance of thin-film composite membranes: Novel insights into the role of poly (vinyl alcohol) coating positions. J.Membr.Sci., 614 (2020) 118526.

[221] Y. Mansourpanah, S. Madaeni, and A. Rahimpour. Fabrication and development of interfacial polymerized thin-film composite nanofiltration membrane using different surfactants in organic phase; study of morphology and performance. J.Membr.Sci., 343 (2009) 219.

[222] N. Misdan, W. Lau, A. Ismail, T. Matsuura, and D. Rana. Study on the thin film composite poly (piperazine-amide) nanofiltration membrane: Impacts of physicochemical properties of substrate on interfacial polymerization formation. Desalination, 344 (2014) 198.

[223] P. Karami, B. Khorshidi, J.B. Soares, and M. Sadrzadeh. Fabrication of highly permeable and thermally stable reverse osmosis thin film composite polyamide membranes. ACS applied materials & interfaces, 12 (2019) 2916.

[224] S. Salgin, U. Salgin, and N. Soyer. Streaming potential measurements of polyethersulfone ultrafiltration membranes to determine salt effects on membrane zeta potential. Int.J.Electrochem.Sci, 8 (2013) 4073.

[225] N. Mahdi, P. Kumar, A. Goswami, B. Perdicakis, K. Shankar, and M. Sadrzadeh. Robust polymer nanocomposite membranes incorporating discrete TiO2 nanotubes for water treatment. Nanomaterials, 9 (2019) 1186.

[226] A.E. Childress, M. Elimelech. Effect of solution chemistry on the surface charge of polymeric reverse osmosis and nanofiltration membranes. J.Membr.Sci., 119 (1996) 253.

[227] K. Khulbe, C. Feng, and T. Matsuura. Nodular structure of polymers in the membrane, (2008).

[228] M. Sadrzadeh, J. Hajinasiri, S. Bhattacharjee, and D. Pernitsky. Nanofiltration of oil sands boiler feed water: Effect of pH on water flux and organic and dissolved solid rejection. Separation and Purification Technology, 141 (2015) 339.

[229] H. Li, W. Shi, Y. Zhang, Q. Du, X. Qin, and Y. Su. Improved performance of poly (piperazine amide) composite nanofiltration membranes by adding aluminum hydroxide nanospheres. Separation and Purification Technology, 166 (2016) 240.

[230] Z. Yang, X. Huang, J. Wang, and C.Y. Tang. Novel polyethyleneimine/TMC-based nanofiltration membrane prepared on a polydopamine coated substrate. Frontiers of Chemical Science and Engineering, 12 (2018) 273.

[231] J. Xiang, Z. Xie, M. Hoang, and K. Zhang. Effect of amine salt surfactants on the performance of thin film composite poly (piperazine-amide) nanofiltration membranes. Desalination, 315 (2013) 156.

[232] S. Xue, Z. Xu, Y. Tang, and C. Ji. Polypiperazine-amide nanofiltration membrane modified by different functionalized multiwalled carbon nanotubes (MWCNTs). ACS applied materials & interfaces, 8 (2016) 19135.

[233] Y. Lv, Y. Du, W. Qiu, and Z. Xu. Nanocomposite membranes via the codeposition of polydopamine/polyethylenimine with silica nanoparticles for enhanced mechanical strength and high water permeability. ACS applied materials & interfaces, 9 (2017) 2966.

[234] J. nan Shen, C. chao Yu, H. min Ruan, C. jie Gao, and B. Van der Bruggen. Preparation and characterization of thin-film nanocomposite membranes embedded with poly (methyl methacrylate) hydrophobic modified multiwalled carbon nanotubes by interfacial polymerization. J.Membr.Sci., 442 (2013) 18.

[235] Q. An, F. Li, Y. Ji, and H. Chen. Influence of polyvinyl alcohol on the surface morphology, separation and anti-fouling performance of the composite polyamide nanofiltration membranes. J.Membr.Sci., 367 (2011) 158.

[236] X. Zhu, X. Cheng, X. Luo, Y. Liu, D. Xu, X. Tang, et al. Ultrathin thin-film composite polyamide membranes constructed on hydrophilic poly (vinyl alcohol) decorated support toward enhanced nanofiltration performance. Environ.Sci.Technol., 54 (2020) 6365.

[237] Y. Chiang, Y. Hsub, R. Ruaan, C. Chuang, and K. Tung. Nanofiltration membranes synthesized from hyperbranched polyethyleneimine. J.Membr.Sci., 326 (2009) 19.

[238] M. Jahanshahi, A. Rahimpour, and M. Peyravi. Developing thin film composite poly (piperazine-amide) and poly (vinyl-alcohol) nanofiltration membranes. Desalination, 257 (2010) 129.

[239] C. Boo, Y. Wang, I. Zucker, Y. Choo, C.O. Osuji, and M. Elimelech. High performance nanofiltration membrane for effective removal of perfluoroalkyl substances at high water recovery. Environ.Sci.Technol., 52 (2018) 7279.

[240] K. Yoon, B.S. Hsiao, and B. Chu. High flux nanofiltration membranes based on interfacially polymerized polyamide barrier layer on polyacrylonitrile nanofibrous scaffolds. J.Membr.Sci., 326 (2009) 484.

[241] A. Alkhudhiri, N. Darwish, and N. Hilal. Membrane distillation: a comprehensive review. Desalination, 287 (2012) 2.

[242] J.A. Kharraz, A.K. An. Patterned superhydrophobic polyvinylidene fluoride (PVDF) membranes for membrane distillation: Enhanced flux with improved fouling and wetting resistance. J.Membr.Sci., 595 (2020) 117596.

Supporting information of chapter four

Supporting Information

Gravity Assisted Super High Flux Microfiltration Polyamide-imide Membranes for Oil/Water Emulsion Separation

Asad Asad[1], Masoud Rastgar[1], Dan Sameoto[2], and Mohtada Sadrzadeh[3]*

[1] Department of Mechanical Engineering, University of Alberta, National Institute for Nanotechnology (NINT), T6G 2M9, Canada

[2] Department of Mechanical Engineering, University of Alberta, 10-390 Donadeo Innovation Center for Engineering (DICE), T6G 1H9, Canada

16. Department of Mechanical Engineering, Advanced Water Research Lab (AWRL), University of Alberta 10-367 Donadeo Innovation Center for Engineering (DICE), T6G 1H9, Canada

---

Corresponding Author: sadrzade@ualberta.ca

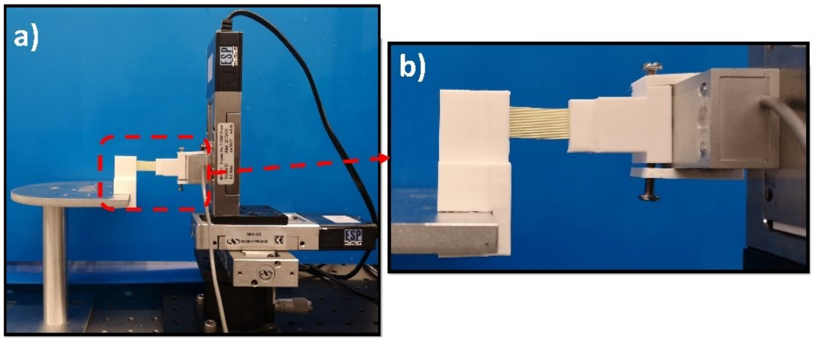

Figure 4.S 1. Images of the tensile measurement setup. a) The overall system. b) 3D printed PLA holders (white) clamping the membrane sample (cream). The applied displacement and the corresponding forces were detected using a National Instrument motion controller (Model No. ESP301), data acquisition (DAQ) hub (NI USB-6289), and a load cell (Transducer Techniques, MLP-10).

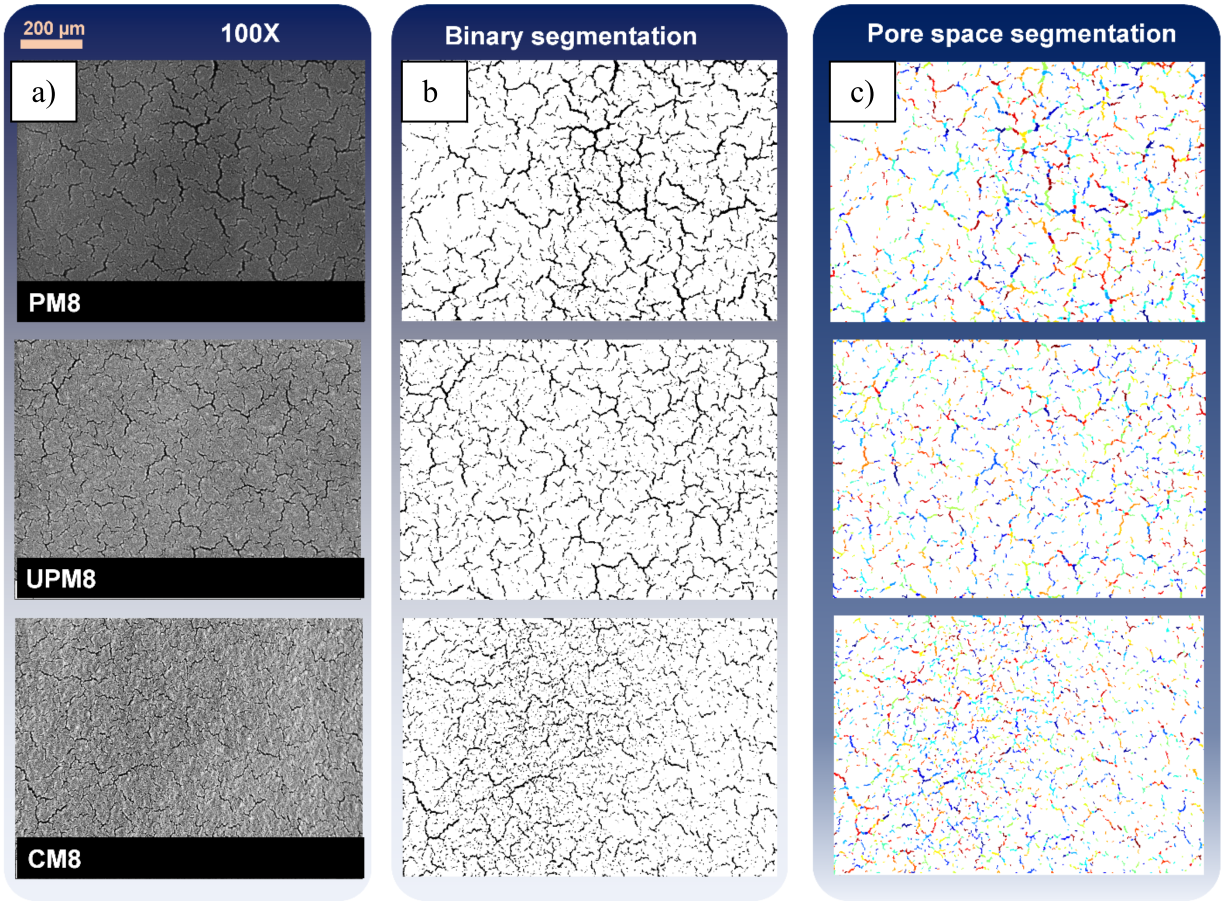

Figure 4.S 2. Different steps of image analysis for the top surface of 8wt% PAI membranes to obtain the pore size distribution curves. The first column shows the original SEM figure of 8 wt.% PAI membranes (PM8, UPM8, and CM8). The second column shows the grey-scale SEM image in which darker spaces were considered as longitudinal pores. The pores were distinguished from the surrounding solid polymer by converting them into black and white colors, respectively. The last column shows the pore space segmentation using the watershed algorithm which is commonly used to separate overlapped pores. Finally, the area of each detected segment (pore) is measured and used to calculate the radius (pore diameter) of an equivalent circle with the same area.

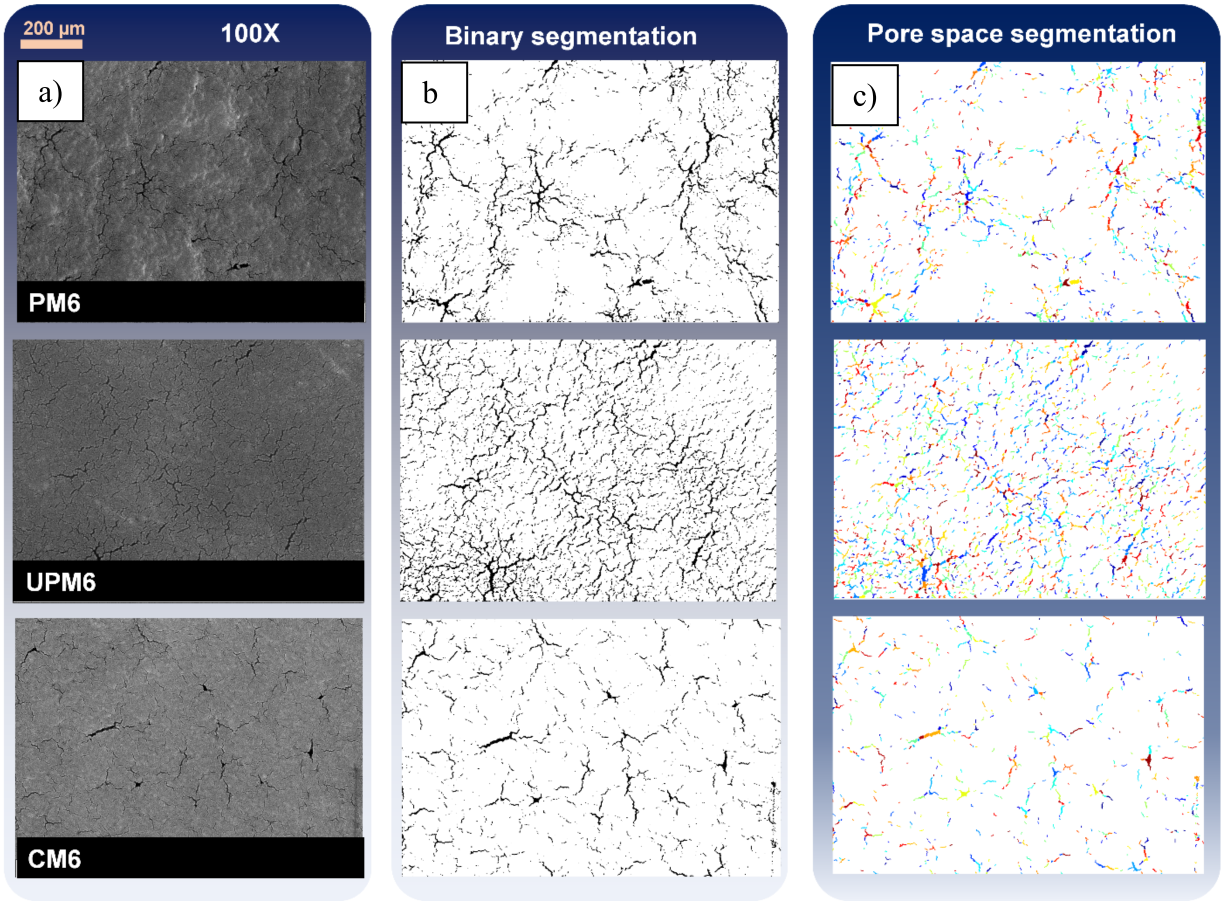

Figure 4.S 3**.** Different steps of image analysis for the top surface of 6wt% PAI membranes to obtain the pore size distribution curves. The first column shows the original SEM figure of 6wt.% PAI membranes (PM6, UPM6 and CM6). The second column shows the grey-scale SEM image in which darker spaces were considered as longitudinal pores. The pores were distinguished from the surrounding solid polymer by converting them into black and white colors, respectively. The last column shows the pore space segmentation using the watershed algorithm which is commonly used to separate overlapped pores. Finally, the area of each detected segment (pore) is measured and used to calculate the radius (pore diameter) of an equivalent circle with the same area.

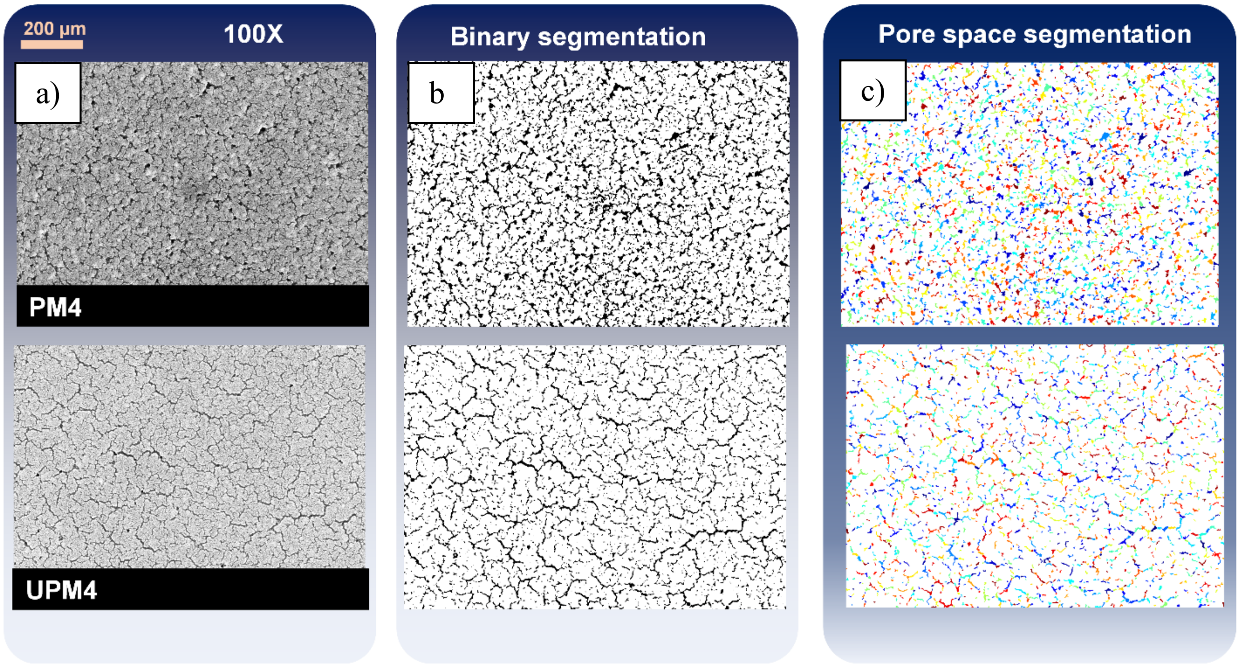

Figure 4.S 4**.** Different steps of image analysis for the top surface of 4wt% PAI membranes to obtain the pore size distribution curves. The first column shows the original SEM figure of 4wt.% PAI membranes (PM4 and UPM4). The second column shows the grey-scale SEM image in which darker spaces were considered as longitudinal pores. The pores were distinguished from the surrounding solid polymer by converting them into black and white colors, respectively. The last column shows the pore space segmentation using the watershed algorithm which is commonly used to separate overlapped pores. Finally, the area of each detected segment (pore) is measured and used to calculate the radius (pore diameter) of an equivalent circle with the same area.

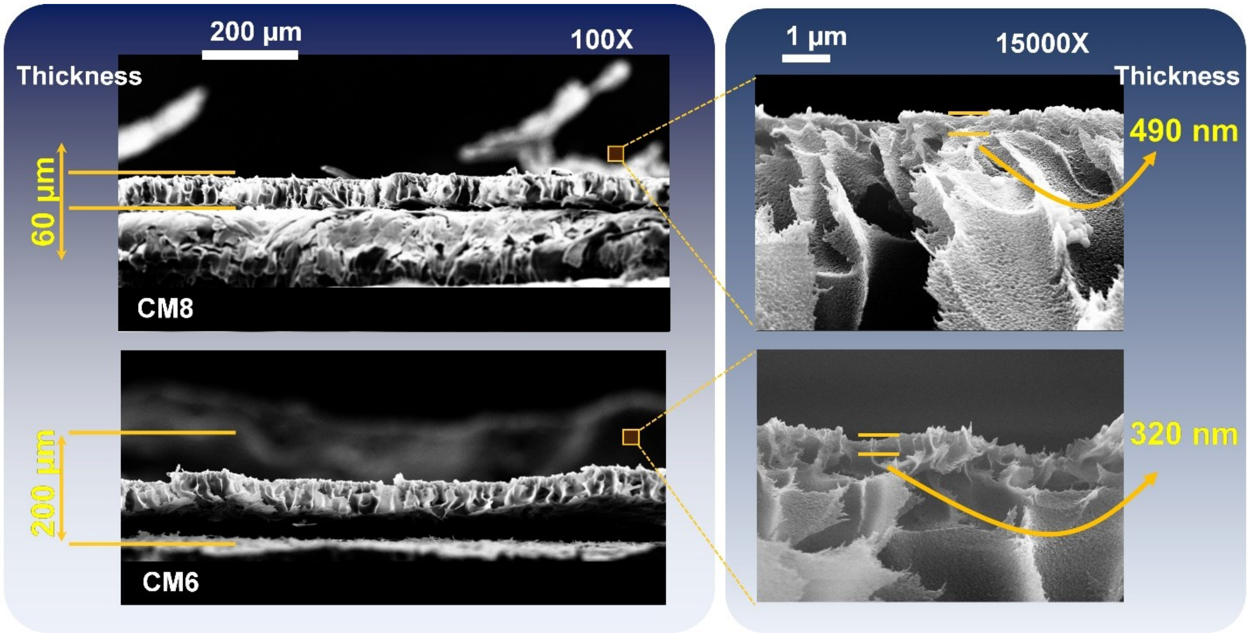

Figure 4.S 5. Cross-sectional SEM images of NIPS membranes with two different magnifications

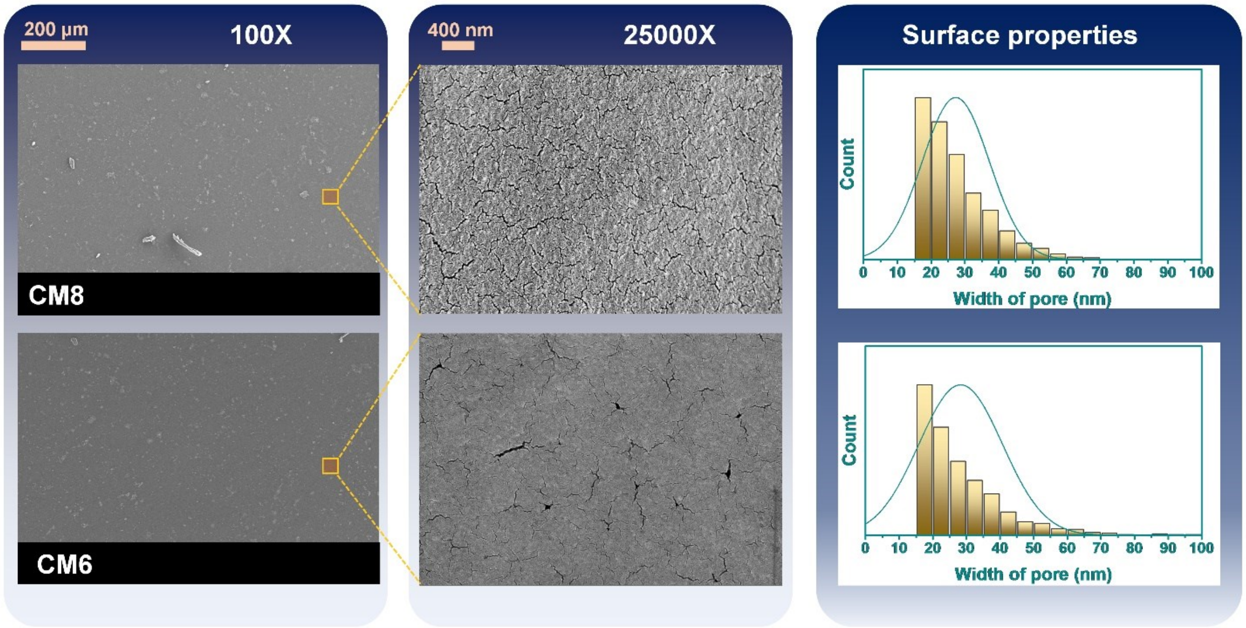

Figure 4.S 6. Top FESEM images from the surfaces of HFPS membranes with corresponding pore size distribution curves. The procedure to measure the surface properties was similar to Figure 4.S1, Figure 4.S2, and Figure 4.S3.

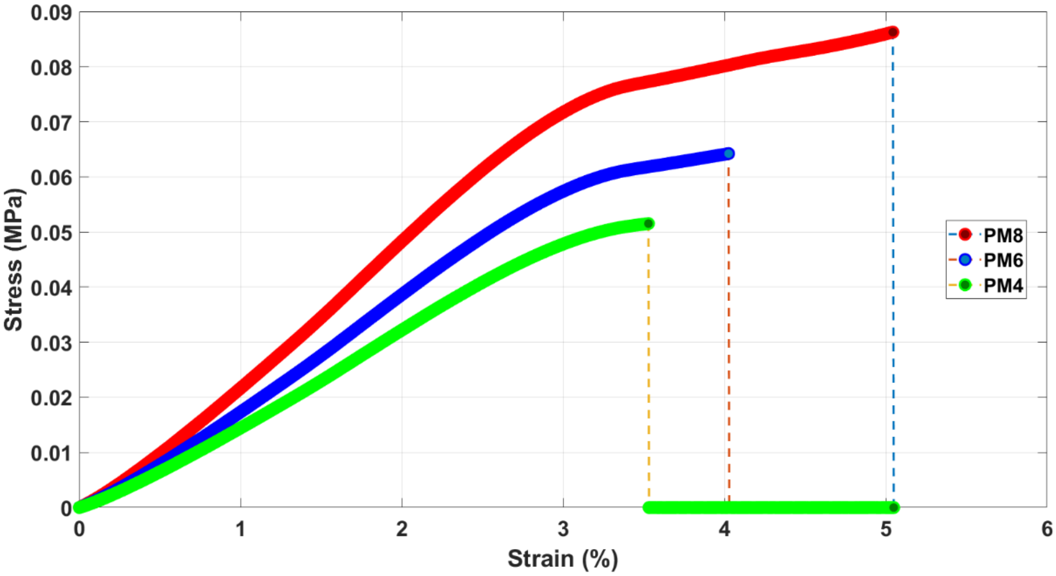

Figure 4.S 7. Stress-strain diagram of the fabricated patterned membranes.

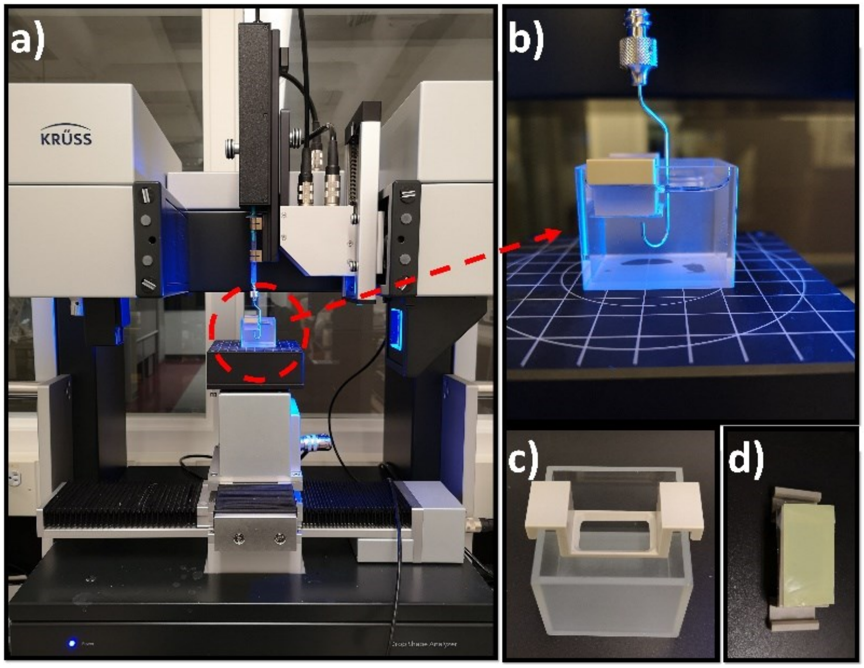

Figure 4.S 8. a) Image of the contact angle analyzer instrument used to obtain the underwater OCA data. b) a closer snapshot on the optically sensitive quartz cuvette filled with DI water with a J-shaped needle lowered into the cuvette and fixed to place 6 µL oil droplet on the membrane surface. c) & d) show the quartz cuvette and the plastic holder with a membrane attached to the latter (active side of the membrane is faced up). By placing the plastic holder inside the cuvette, the active side of the membrane will be faced down.

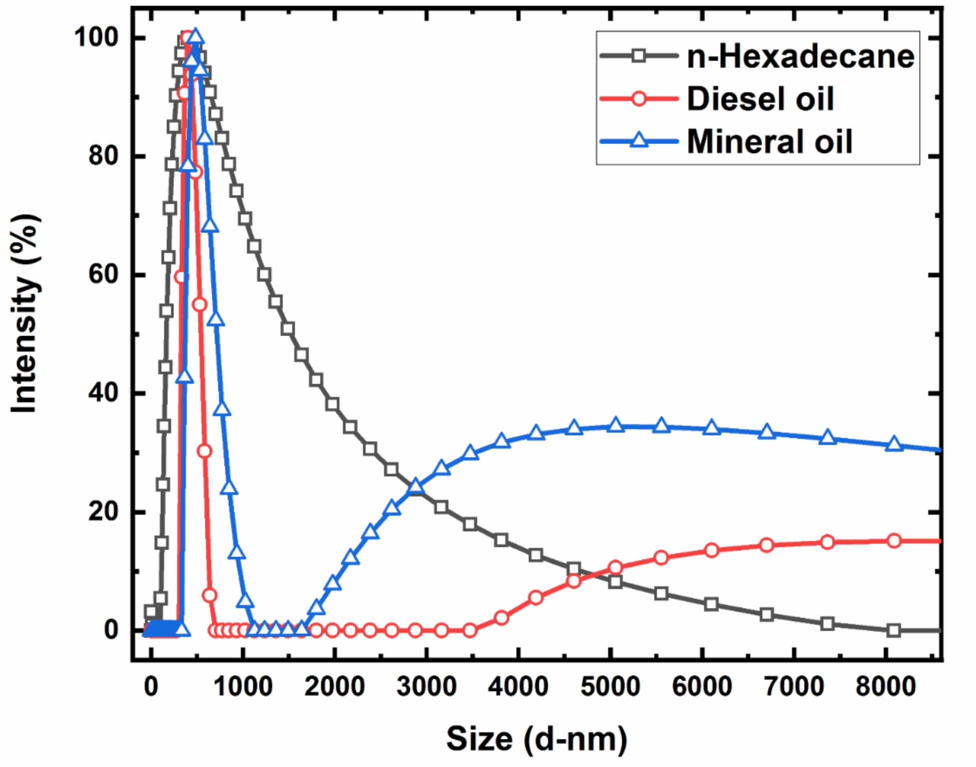

Figure 4.S 9. DLS measurement of the oil size distribution for three different oil emulsions in water